

8. SITE 967¹

Shipboard Scientific Party²

HOLE 967A

Date occupied: 1 April 1995
Date departed: 2 April 1995
Time on hole: 1 day
Position: 34°04.098'N, 32°43.523'E
Bottom felt (drill-pipe measurement from rig floor, m): 2564.2
Distance between rig floor and sea level (m): 11.2
Water depth (drill-pipe measurement from sea level, m): 2553.0
Total depth (from rig floor, m): 2705.5
Penetration (m): 141.3
Number of cores (including cores having no recovery): 16
Total length of cored section (m): 141.3
Total core recovered (m): 142.1
Core recovery (%): 95.8
Oldest sediment cored:
Depth (mbsf): 148.30
Nature: calcareous ooze
Measured velocity (km/s): 2.14

HOLE 967B

Date occupied: 2 April 1995
Date departed: 3 April 1995
Time on hole: 13 hr
Position: 34°04.094'N, 32°43.526'E
Bottom felt (drill-pipe measurement from rig floor, m): 2566.2
Distance between rig floor and sea level (m): 11.2
Water depth (drill-pipe measurement from sea level, m): 2555.0
Total depth (from rig floor, m): 2687.7
Penetration (m): 121.5
Number of cores (including cores having no recovery): 14
Total length of cored section (m): 121.5
Total core recovered (m): 126.6
Core recovery (%): 104.0
Oldest sediment cored:
Depth (mbsf): 121.50
Nature: calcareous ooze

HOLE 967C

Date occupied: 3 April 1995
Date departed: 3 April 1995
Time on hole: 11 hr
Position: 34°04.270'N, 32°43.528'E
Bottom felt (drill-pipe measurement from rig floor, m): 2564.0
Distance between rig floor and sea level (m): 11.2
Water depth (drill-pipe measurement from sea level, m): 2552.8
Total depth (from rig floor, m): 2678.4
Penetration (m): 114.4
Number of cores (including cores having no recovery): 13
Total length of cored section (m): 114.4
Total core recovered (m): 119.6
Core recovery (%): 104.0
Oldest sediment cored:
Depth (mbsf): 13.00
Nature: calcareous matrix-supported conglomerate

HOLE 967D

Date occupied: 3 April 1995
Date departed: 3 April 1995
Time on hole: 09 hr, 30 min
Position: 34°04.253'N, 32°43.531'E
Bottom felt (drill-pipe measurement from rig floor, m): 2562.8
Distance between rig floor and sea level (m): 11.2
Water depth (drill-pipe measurement from sea level, m): 2551.6
Total depth (from rig floor, m): 2579.0
Penetration (m): 16.2
Number of cores (including cores having no recovery): 2
Total length of cored section (m): 16.2
Total core recovered (m): 16.9
Core recovery (%): 104.3
Oldest sediment cored:
Depth (mbsf): 16.20
Nature: nannofossil ooze and clay
Earliest age: Pleistocene

HOLE 967E

Date occupied: 3 April 1995
Date departed: 9 April 1995
Time on hole: 5 days, 13 hr, 30 min

¹Emeis, K.-C., Robertson, A.H.F., Richter, C., et al., 1996. *Proc. ODP, Init. Repts.*, 160: College Station, TX (Ocean Drilling Program).

²Shipboard Scientific Party is given in the list preceding the Table of Contents.

Position: 34°04.106'N, 32°43.525'E

Bottom felt (drill-pipe measurement from rig floor, m): 2564.0

Distance between rig floor and sea level (m): 11.3

Water depth (drill-pipe measurement from sea level, m): 2552.7

Total depth (from rig floor, m): 3164.3

Penetration (m): 600.3

Number of cores (including cores having no recovery): 51

Total length of cored section (m): 488.4

Total core recovered (m): 72.3

Core recovery (%): 14.8

Oldest sediment cored:

Depth (mbsf): 600.30

Nature: calcarenite

HOLE 967F

Date occupied: 3 April 1995

Date departed: 3 April 1995

Time on hole: 02 hr

Position: 34°04.254'N, 32°43.530'E

Bottom felt (drill-pipe measurement from rig floor, m): 2564.0

Distance between rig floor and sea level (m): 11.2

Water depth (drill-pipe measurement from sea level, m): 2552.8

Total depth (from rig floor, m): 2573.5

Penetration (m): 9.5

Number of cores (including cores having no recovery): 1

Total length of cored section (m): 9.5

Total core recovered (m): 9.9

Core recovery (%): 104.0

Oldest sediment cored:

Depth (mbsf): 9.50

Nature: nanofossil ooze

Earliest age: Pleistocene

Comments: The positions for Holes 967D and 967F are the same. The core that was designated as "Hole 967F" was originally called a missed mud-line core for Hole 967D. Drilling continued without offsetting the ship and was designated Hole 967D. Upon investigation the missed mud-line core was found to contain sapropels. The decision was made to designate it Hole 967F, and the core was then described and processed according to standard procedure.

Principal results: The main objectives of drilling at Site 967 were to study the sedimentary and structural setting of the lower northern slope of the Eratosthenes Seamount and to test the hypothesis that a small raised ridge near the foot of the lower slope of the northern flank of the seamount is within a contractional tectonic setting that could be related to underthrusting of the seamount beneath Cyprus. The results provide important new information about the tectonic setting and an unexpected insight into the earlier history of the Eratosthenes Seamount that was not achieved at the other sites drilled.

The section begins with approximately 100 m of burrowed nanofossil ooze, nanofossil clays, mud turbidites, and sapropels, with age determination ranging back to the earliest Pliocene. Sedimentation rates range from 5 to 57 m/m.y., and average 26 m/m.y. Paleomagnetic studies allow the recognition of several polarity zones, although diagenetic effects related to the sapropels have complicated the directional signature. Preliminary studies of benthic foraminifers suggest that in the Pleistocene, water depths were similar to today (2500 m), but were somewhat less in the late Pliocene (1800–2500 m) and earlier. The section is relatively undisturbed,

but for scattered, small high-angle faults and an important interval of slumping associated with an overlying debris-flow unit, which in one hole corresponds to a paleontologically determined hiatus of up to 0.25 m.y. Eighty discrete sapropels were identified, with organic carbon values up to 17%, allowing valuable post-cruise comparisons with the sapropels recovered from the Eratosthenes plateau area (Site 966). Sediment sequences cored in the five APC holes at Site 967 were correlated by means of continuously logged physical properties, color, and sedimentary features, which allowed the construction of a composite section. Organic geochemical studies suggest that the sapropels are composed mainly of degraded marine organic matter, although smear-slide analysis indicates the presence of abundant fine plant material in some individual sapropels.

The underlying unit (15–25 m thick) consists of well-consolidated, red-colored, nanofossil-bearing, fine- to medium-grained sediments, with scattered carbonate fragments; these sediments accumulated in a rapidly depositing, possibly fault-controlled, deep-sea setting. The identification of microfossils of late Miocene–early Pliocene, Miocene, Oligocene, and middle Eocene age suggests erosion from parts of a lithologic column, possibly of mainly pelagic-type deposits, that is not present at Site 967, perhaps because of uplift and erosion. Both the pore-water chemistry and log data indicate the presence of gypsum, of presumed Messinian age, at about 120–130 mbsf. The increased heat-flow values recorded at the top of this unit are possibly related to upward fluid flow through the fractured limestones beneath.

The section continues downward with about 310 m of well-lithified nanofossil cherts of middle Eocene to Late Cretaceous (late Santonian) age. Notable features include concretions of replacement chert in both the middle Eocene and Upper Cretaceous parts of the section and thin intervals of finely laminated low-oxygen facies in the Upper Cretaceous interval. A pervasive fabric of steeply dipping normal faults is present, together with a small suite of relatively shallow-dipping normal and reverse faults; extensive faulting is also imaged with the Formation Micro-Scanner.

The following unit (approximately 95 m) consists of poorly recovered fractured shallow-water carbonates, which as yet have not yielded identifiable fossils. FMS data reveal pervasive tectonic effects. Drilling of the final approximately 85 m recovered only a small number of clasts of shallow-water limestone facies, with slickensides and other evidence of intense tectonic brecciation. The FMS data also reveal evidence of an extensively developed breccia-like fabric. The results of shipboard sonic velocity studies suggest that the brecciated interval lies within a zone of reverse faulting from the study of seismic profiles. Also, inorganic geochemical analysis indicates the presence of brine at depth that may have been derived from Messinian evaporites.

In summary, Site 967 records an early shallow-water carbonate platform setting, followed by 40 m.y. of pelagic carbonate deposition during Late Cretaceous–middle Eocene time. Some marine deposition took place in the vicinity during the Oligocene and Miocene, but any sediments of this age at Site 967 were removed, possibly by tectonically induced uplift and erosion. After the minor accumulation of gypsum, presumably in the Messinian, deep-water deposition resumed in the early Pliocene, including sapropels, followed by further deepening after the late Pliocene in response to dominantly tectonic subsidence. The present local uplift of the ridge may relate to the onset of contractional tectonics in the late Pliocene–early Pleistocene that was accompanied by a hiatus, slumping, and the formation of debris flows.

BACKGROUND AND OBJECTIVES

Site 967 is located on a small ridge trending west-southwest to east-northeast at the base of the northern slope of the Eratosthenes Seamount (Limonov et al., 1994) in water 2554 m deep (Figs. 1, 2). The site is the third on the transect of holes drilled from the Eratosthenes Seamount to the Cyprus margin, which was originally designed to test the tectonic hypothesis that the seamount is breaking up and is in the process of being thrust beneath Cyprus in an active margin setting (Robertson et al., 1994a, 1995).

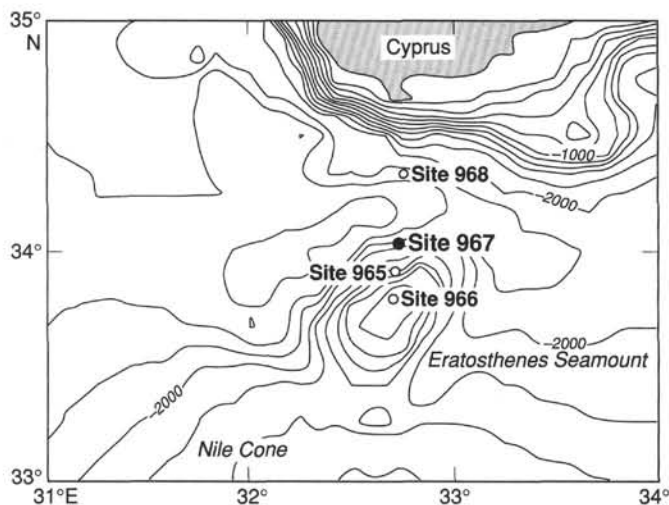


Figure 1. Bathymetric sketch map showing the location of Site 967 on the lower slope of the Eratosthenes Seamount in relation to the position of the other sites drilled.

The aims of drilling at Site 967 were as follows: (1) to determine the lithology and age of the Pliocene-Quaternary succession at this site in relation to Site 965 (upper slope of the seamount) and Site 966 (crestal area of the seamount); (2) to determine the origin and age of a prominent, deformed reflector at the base of the inferred Pliocene-Quaternary succession; (3) to determine the lithology, age, and origin of several less distinct and apparently deformed reflectors that are identified on the migrated site-survey data (D. Klaeschen and R. von Huene, pers. comm., 1995); (4) to seek small-scale structural evidence (e.g., normal and reverse faults) to allow the paleo-stress regime of the basement ridge to be inferred (i.e., compressional or extensional); and (5) to determine the nature of the paleoenvironments associated with the Messinian/Pliocene boundary in relation to the desiccation of the Mediterranean and the prevailing tectonic regime.

In addition, the relatively expanded Pliocene to Pleistocene sedimentary section imaged on the seismic lines promised a more complete and better resolved Pleistocene sedimentary record of sapropel formation than at Site 966. From the tectonic model of subsidence and underthrusting of the northern Eratosthenes Seamount it follows that the water depth of deposition increased greatly since the late Miocene. Site 967 has subsided more than the upper flank and crestal sites (Sites 965 and 966) and may have subsided earlier. If we were able to correlate sapropel events between the crestal Site 966 and the (now) lower slope Site 967, we could elegantly test the hypothesis of depth dependence of organic carbon preservation during sapropel deposition. Provided that the age model constructed from biostratigraphic, paleomagnetic, and lithostratigraphic analyses is of sufficient resolution, a time lag between the deep and shallow sites should be discernible. In addition, the pattern of sapropel deposition, the organic carbon concentrations of the sapropels, and the pattern of intervening turbidite deposition may greatly facilitate reconstruction of the tectonic subsidence at Site 967.

GEOLOGICAL SETTING

Site 967 is located at a critical position near the foot of the northern slope of the Eratosthenes Seamount, on the northern flank of a small (approximately 300 m high) ridge (Figs. 3, 4). Wide-beam OKEAN side-scan sonar records indicate that the ridge is linear and trends nearly northeast-southwest (Alibes et al., 1994).

The site-survey data indicate that the upper slope and the crestal area of the seamount are today under extensional stress associated

with normal faulting on varying scales. The structural observations from Sites 965 and 966 indicate a dominant role of extensional faulting in both the Pliocene-Quaternary and underlying units. However, there is also a sparse record of compressional structures at the Eratosthenes crestal site (Site 966). An important question to be answered by drilling at Site 967 is the state of paleostress beneath the lower northern slope, compared to other parts of the seamount.

Seismic data collected during the cruise of *Gelendzhik* are interpreted to indicate that the northern margin of the Eratosthenes Seamount is breaking up and being thrust northward beneath a deep-water basin infilled with Pliocene-Quaternary turbidites (Limonov and Woodside, 1994; Robertson et al., 1994b, 1994c, 1995). The reasoning is that a prominent reflector at the base of the Pliocene-Quaternary succession, shown at Site 966 to be well-cemented shallow-water limestone, appears to dip beneath the small basement ridge at the foot of the seamount's northern slope. Reflectors similar in character to those of the pre-Pliocene carbonates are seen above this, which suggests that reverse faulting has taken place to form the raised ridge. Also, the Pliocene-Quaternary reflectors are domed, forming a broad, nearly anticlinal structure, involving a process that appears to be still active.

On the depth-migrated version of the same seismic data (D. Klaeschen and R. von Huene, pers. comm., 1995; Fig. 5), a prominent reflector identified as limestone beneath the Pliocene-Quaternary succession on the Eratosthenes Seamount can again be traced, although indistinctly, beneath the small ridge structure under discussion. An alternative interpretation could be that the southern margin of the ridge is bounded by a high-angle normal fault. If so, however, such a fault would have to be of pre-Pliocene-Quaternary age, as this unit is not offset by the seismically imaged faults.

In detail, the migrated data reveal several reflectors that could be penetrated at Site 967. The semitransparent, inferred Pliocene-Quaternary succession is of relatively uniform thickness (approximately 100 m) over the basement high. This unit is underlain by a slightly less seismically transparent interval that appears to be laterally discontinuous and is ponded in depressions on an irregular underlying topography defined by a much more intense reflector. Several indistinct reflectors visible at less than 300 m on the depth-migrated version of the same seismic profile could reflect further lithology changes at depth.

A reasonable interpretation of the seismic data prior to drilling at Site 967 was that an irregular surface of a pre-late Miocene age unit (limestone?) is unconformably overlain by a Pliocene-Quaternary muddy succession that is being actively deformed to produce the present anticlinal structure. The site-survey data collected by *JOIDES Resolution* include several crossing lines that further allow the orientation of an inferred thrust or décollement beneath the ridge to be determined. This dips at about 6° with an azimuth of 340° (see "Site Geophysics" section, this chapter).

Additionally, at Site 967 we hoped to recover Pliocene-Quaternary sapropels that might have been deposited in deeper water than those cored on the Eratosthenes Seamount upper slope (Site 965) and crestal areas (Site 966). A gravity core taken by *Gelendzhik* very close to Site 967 recovered a relatively expanded succession of Quaternary sapropels compared to those cored at the Eratosthenes crestal sites. Sapropel S1 is 16.5 cm thick and includes five small fining-upward units indicative of redeposition by low-density turbidity currents. Two further sapropels at greater depth, although bioturbated, were interpreted as of more pelagic origin. However, mud turbidites were identified at both the top and bottom of the core and sedimentation-rate calculations indicate deposition rates typical of redeposition processes. The mud is assumed to have been derived by resuspension from the flanks of Eratosthenes Seamount located to the south, in contrast to turbidites in the deep basin to the north that are assumed to have been derived both from Cyprus and from the Nile River (Cita et al., 1984; R. Lucchi, pers. comm., 1995). Investigating the Pliocene to Pleistocene section could help to decide if the ridge was already present during deposition, and dilute turbidity currents then

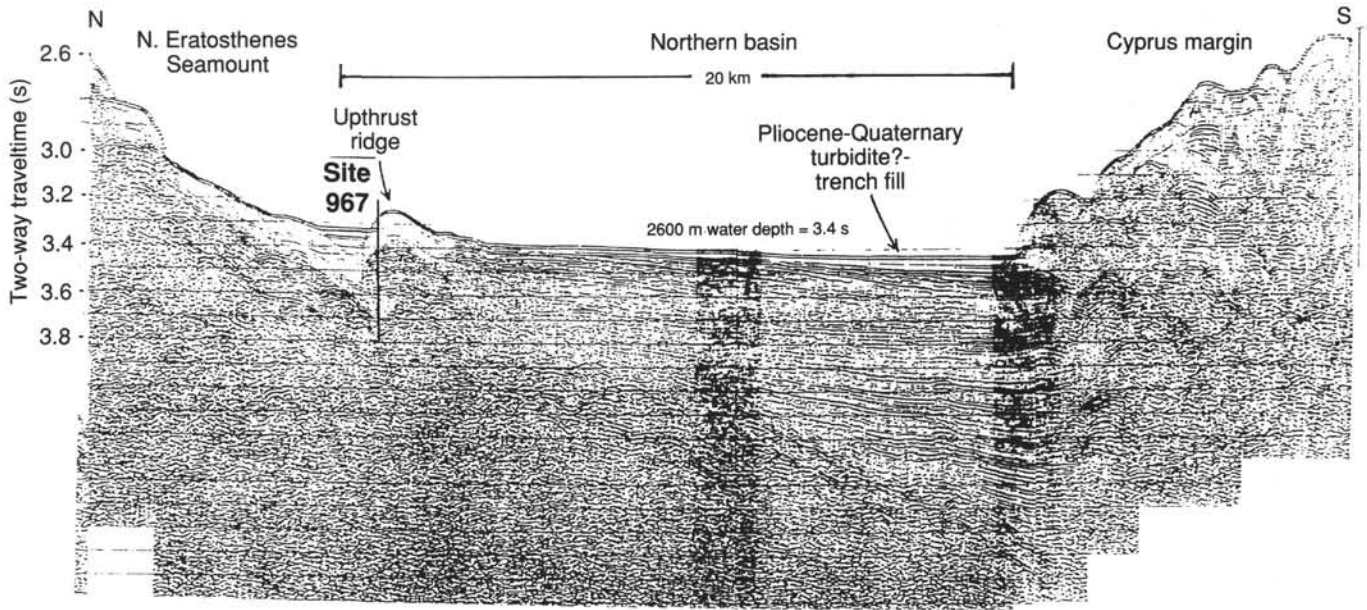


Figure 2. Location of Site 967 on TREDMAR-3 Line 120, 1993. The site is located on the southern slope of a small ridge, inferred to have been produced by compression and reverse faulting. The broad basin to the north is inferred to be the site of a deep-sea trench that is infilled with Pliocene-Quaternary sediments.

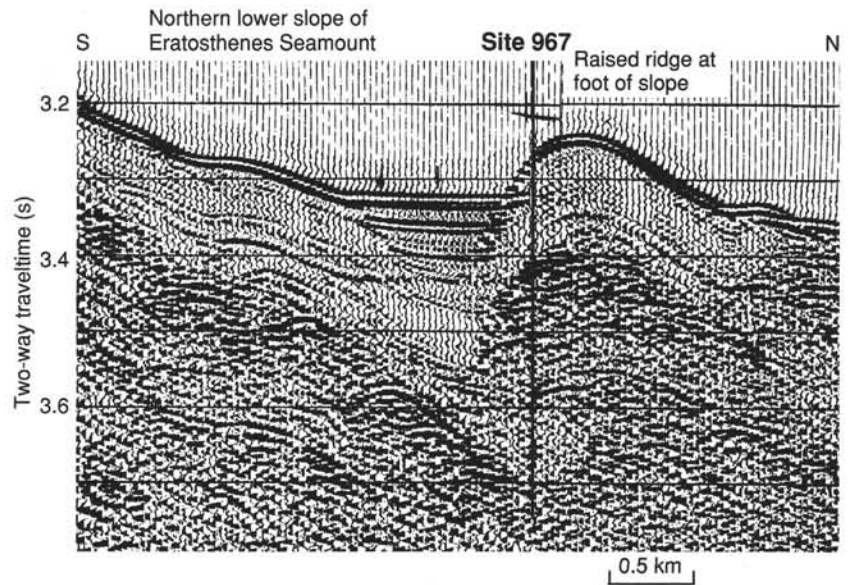


Figure 3. Location of Site 967. Note the domed semitransparent upper unit of Pliocene-Quaternary sediments and the irregular highly reflective unit beneath, which was shown by drilling to be shallow-water limestone. The high-amplitude reflector beneath the Pliocene-Quaternary succession can be traced beneath the base of slope ridge, whereas the domed unit above implies that recent, or active, underthrusting is taking place. Part of TREDMAR-3 Line 120, 1993.

enveloped the ridge, depositing a continuous blanket over a raised topography. Alternatively, the turbidites might have been deposited in a basinal setting, followed by rapid tectonic uplift to form the present ridge structure. It was hoped that drilling could distinguish between these two alternatives.

OPERATIONS

Transit to Site 967

The 17-nmi sea voyage to Site 967 (proposed Site ESM-3A) required 1.5 hr at an average speed of 11.3 kt. A Datasonics 354M beacon (S/N 1240, 14.5 kHz) was deployed at 1150 hr on 1 April.

Hole 967A

The same APC/XCB BHA used at the previous sites was used on proposed Site ESM-3A: a 10 1/8-in. RBI PDC bit and APC/XCB BHA with a nonmagnetic drill collar. Hole 967A was spudded at 1905 hr on 1 April. A seafloor depth of 2553.0 m by drill-pipe measurement was indicated. APC Cores 160-967A-1H through 13H were taken from 0 to 123.3 mbsf, with 123.3 m cored and 127.6 m recovered (103.5% recovery, Table 1). Cores were oriented from Core 160-967A-3H. ADARA heat-flow measurements were taken on Cores 160-967A-5H, 7H, and 9H. The top and bottom of the liner imploded on Core 160-967A-12H. The maximum gas detected was 5 ppm methane. XCB Cores 160-967A-14X through 16X were taken from 123.3 to 141.3 mbsf, with 18.0 m cored and 14.5 m recovered (80.6%

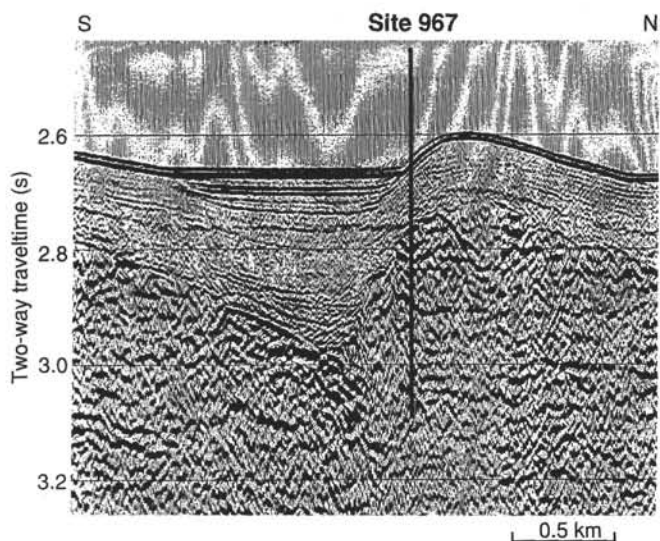


Figure 4. Location of Site 967 on the migrated version of Line 120 (see Fig. 5) reprocessed by D. Klaeschen and R. Von Huene. Note that the zone of underthrusting beneath the basement ridge is less obvious than in Figure 3 and could alternatively be interpreted as a high-angle fault, although this interpretation is not favored. Drilling was aimed at testing these alternatives.

recovery). XCB recovery was poor in the stiff nanofossil ooze using a standard shoe and 8- and 9-finger core catchers. The last two cores jammed in the shoe. Overall recovery was 95.8%. The bit cleared the seafloor at 1140 hr on 2 April.

Hole 967B

The ship was offset 10 m to the south. Hole 967B was spudded at 1241 hr on 2 April. Core 160-967B-1H indicated a seafloor depth of 2555.0 m. APC Cores 160-967B-1H through 14H were taken from 0 to 121.5 mbsf (Table 1), with 121.5 m cored and 126.6 m recovered (104.2% recovery). Cores were oriented from Core 160-967B-3H. Cores 160-967B-12H through 14H had partial strokes, but piston coring continued because the XCB had very poor recovery and suck-in disturbance in the APC cores could be detected. The bit cleared the seafloor at 0040 hr on 3 April.

Hole 967C

The ship was offset 326 m to the north of Hole 967B and Hole 967C was spudded at 0210 hr on 3 April. Core 160-967C-1H indicated a seafloor depth of 2552.8 m. APC Cores 160-967C-1H through 13H were taken from 0 to 114.4 mbsf (Table 1), with 114.4 m cored and 119.5 m recovered (104.5% recovery). Cores were oriented from Core 160-967C-3H. Cores 160-967C-12H and 13H had partial strokes and Core 160-967C-13H was mostly suck-in. The bit cleared the seafloor at 1150 hr on 3 April.

Hole 967D

The ship was offset 20 m to the south of Hole 967C. The first mud-line core attempt recovered 9.87 m, and there was doubt that it was a good mud-line core; therefore, it was kept for later laboratory instruction and not archived. Hole 967D was spudded at 1415 hr on 3 April. Core 160-967D-1H indicated a seafloor depth of 2551.5 m. APC Cores 160-967D-1H and 2H were taken from 0 to 16.2 mbsf, with 16.2 m cored and 16.9 m recovered (104.3% recovery). The bit cleared the rotary table at 2115 hr on 3 April.

Hole 967E

The ship was offset south to 20 m north of Hole 967A and an RCB BHA was assembled. The bit indicated a seafloor depth of 2552.7 m. Hole 967E was spudded at 0320 hr on 4 April. The hole was drilled to 109.5 mbsf. RCB Cores 160-967E-1R through 51R were taken from 0 to 600.3 mbsf (Table 1), with 111.5 m drilled, 488.4 m cored, and 72.3 m recovered (14.8% recovery). Following six cores with negligible recovery, the hole was drilled with a center bit from 561.8 to 563.8 mbsf in an attempt to clean out the bit throat and remove rollers and rubble from the bottom of the hole. The center bit was marked by the bit teeth, indicating that the bit bearings might be failing. Coring continued to 600.3 mbsf, with negligible recovery.

Logging Operations at Hole 967E

A short trip was made to condition the hole for logs. No drag and 10 m of light fill on the bottom indicated average hole conditions for logging. The hole was displaced with 9.0-ppg sepiolite/seawater mud, the bit was released with the mechanical bit release (MBR), and the sleeve was shifted shut. The pipe was pulled back to 91.3 mbsf for logging. The Quad combo log was run to 3162 m below rig floor (mbrf), the GST to 3145 mbrf, the FMS to 3144 mbrf, and the GHMT to 3148 mbrf. Logging was finished at 0200 hr on 9 April, and the bit was pulled. The entire BHA was inspected on the trip out. The MBR cleared the rotary table at 1040 hr. The beacon was recovered and the transit to Site 968 began.

Hole 967F

The bit cleared the seafloor at Hole 967C at 1150 hr on 3 April and the ship was offset 20 m to the south of Hole 967C. A mud-line core attempt made at 1200 hr recovered 9.87 m; however, there was doubt that it was a good mud-line core, and it was kept for later laboratory instruction and not archived initially. Later, the core liner was split and revealed two sapropels that were needed to complete the upper section; therefore, it was archived as Core 160-967F-1H taken from 0 to 9.5 mbsf, with 9.5 m cored and 9.9 m recovered.

SITE GEOPHYSICS

One of the objectives at this site was to drill through a thrust zone inferred to lie beneath a small east-northeast- to west-southwest-oriented ridge at the northern base of the seamount. Two seismic lines run for the site survey were designed to follow the east-west and north-south survey lines carried out earlier by *Gelendzhik* (Limonov et al., 1994) in order to ensure a site location slightly southeast of the top of the ridge but not so far off the ridge as to be in the basin to the south, where the site objectives might not be achieved (Fig. 6). Too far to the north would mean that the inferred thrust zone would be too deep to reach.

Both survey lines satisfactorily presented seismic profiles similar to those of the original site survey, and the site location was therefore well established. On the approach line from the site survey for Site 968, the ridge was crossed farther to the east, where it is much diminished in size (less than 10 m). It is observed to be progressively broader and higher to the west, damming sediments in the basin to the south where the seafloor is almost 40 m shallower than on the northern side of the ridge. Site 967 lies at an elevation about 60 m above the level of the small southern basin and about 1500 m east of a point where the height of the ridge begins to increase to more than 3 times that value.

The morphology of the ridge seems to be controlled by a greater degree of upthrusting in the west than in the east, creating greater relief there. The dipping reflector inferred to be a thrust fault (i.e., dé-

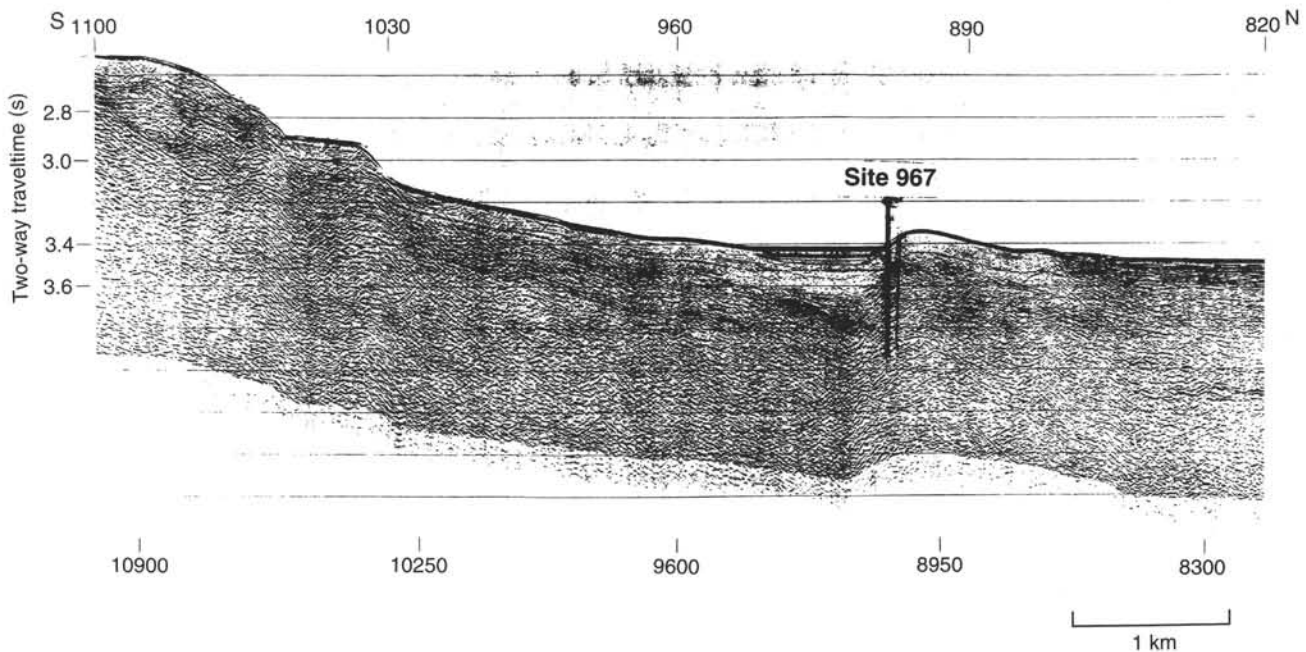


Figure 5. Migrated version of Line 120 reprocessed by D. Klaeschen and R. Von Huene. See text for discussion.

collement) below the southward-thrusted ridge is seen to dip at just under 6° to the north on one line and about 2° degrees to the west on the cross line. This indicates a true dip of the reflecting surface of about 6° to the north-northwest, or roughly perpendicular to the ridge, at least below the southern margin of the ridge at Site 967. The reflector lying below the ridge varies in character, with a very high amplitude and continuity directly to the south of the ridge (Fig. 7). Farther south, it becomes less strong, slightly undulating, and discontinuous, contrasting with the continuity of the overlying upper unit of low-amplitude, continuous, parallel reflectors.

Deeper reflectors are visible beneath the small basin and lower slopes of Eratosthenes Seamount south of the ridge (Fig. 7). There is evidence for some southward thrusting in this lower sequence, as well as for some folding within it. This contrasts with the block forming the ridge at Site 967, where reflectors at depths of 400 to 500 ms two-way traveltime (TWT) show little deformation. The unit forming the upper 140 ms TWT of the profile at Site 967 is characterized by low reflectivity and, based on profiles elsewhere in the region, was assumed to represent the post-Miocene sedimentary succession (Limonov et al., 1994). Below the upper unit and above the inferred décollement are two units with similar seismic character separated by a strong reflector at about 350 ms TWT below the seafloor. Reverse faulting is interpreted to dip steeply northward beneath the ridge along its steeper southern flank.

LITHOSTRATIGRAPHY

The sequence cored at Site 967 recovered 590.7 m of Upper Cretaceous to Holocene sediments. Five lithostratigraphic units were identified on the basis of characteristic visual observation of color, sedimentary structures, smear-slide and thin-section composition, reflectance spectrophotometry measurements, bulk mineralogy (XRD), and carbonate determinations. Within intervals of poor core recovery, reference was made to the downhole measurement data.

The detailed description of sapropels was mainly from Hole 967B. A summary of the lithology at Site 967 is presented in Figure 8. Lithostratigraphic interhole correlation of the upper 114 m of sediments was carried out on the basis of the correlation of sapropels from each hole (Fig. 9). This correlation is in agreement with the col-

or reflectance spectrophotometry (Fig. 10) and magnetic susceptibility data sets (see "Composite Depths" section, this chapter).

Unit I is composed of bioturbated nannofossil ooze and nannofossil clay intercalated with sapropels and turbidites. Unit II consists of well-consolidated nannofossil clay and nannofossil ooze, containing fragments of micritic limestone and inorganic calcite. Unit III contains burrow-mottled, well-lithified foraminifer nannofossil chalk. Unit IV is dominated by well-cemented shallow-water limestones. Unit V is a brecciated limestone.

Description of Lithostratigraphic Units

Lithostratigraphic Unit I

Description: Nannofossil ooze and nannofossil clay

Intervals: Sections 160-967A-1H-1 through 11H-4, Cores 160-967B-1H through 11H, 160-967C-1H through 11H, 160-967D-1H and 2H, and 160-967F-1H

Depth: 0–100 mbsf, Hole 967A; 0–100.3 mbsf, Hole 967B; 0–104.5 mbsf, Hole 967C; 0–16.2 mbsf, Hole 967D; 0–9.5 mbsf, Hole 967F

Age: middle Pliocene to Holocene

The lithology of Unit I is dominated by brown (7.5YR 5/4) and light gray (5Y 7/1) bioturbated nannofossil ooze and nannofossil clay intercalated with sapropels and numerous turbidites. Smear-slide analyses show that the nannofossil ooze is composed of nannofossils (41%–85%), foraminifers (2%–22%), clay (0%–26%), volcanic glass (0%–8%), quartz (0%–22%), and inorganic calcite (0%–10%) (Fig. 11). The nannofossil clay is dominated by clay (46%–86%) with subordinate nannofossils (4%–30%) and foraminifers (0%–5%). The nannofossil ooze and clay are bioturbated throughout by *Chondrites*, *Zoophycos*, and *Planolites*. The bedding of the dominant lithology is horizontal to subhorizontal throughout and is sporadically cut by small high-angle faults (see "Structural Geology" section, this chapter).

Slump/Slide Unit

A distinctive interval of deformed sediments occurs in varying thickness in three holes. It was cored in the interval from Sections 160-967A-6H-5, 110 cm, through 7H-4, 60 cm, (54.4–61.9 mbsf)

Table 1. Coring summary for Site 967.

Core	Date (April 1995)	Time (UTC)	Depth (mbsf)	Length cored (m)	Length recovered (m)	Recovery (%)	Core	Date (April 1995)	Time (UTC)	Depth (mbsf)	Length cored (m)	Length recovered (m)	Recovery (%)		
160-967A-							160-967E-								
1H	1	1720	0.0-9.3	9.3	9.30	100.0	1R	4	0420	109.5-119.1	9.6	2.31	24.0		
2H	1	1810	9.3-18.8	9.5	9.81	103.0	2R	4	0615	119.1-128.7	9.6	0.63	6.6		
3H	1	1845	18.8-28.3	9.5	9.91	104.0	3R	4	0725	128.7-138.3	9.6	3.63	37.8		
4H	1	1945	28.3-37.8	9.5	9.90	104.0	4R	4	0905	138.3-148.0	9.7	4.16	42.9		
5H	1	2100	37.8-47.3	9.5	10.13	106.6	5R	4	1040	148.0-157.7	9.7	5.57	57.4		
6H	1	2155	47.3-56.8	9.5	9.94	104.0	6R	4	1225	157.7-167.3	9.6	3.26	33.9		
7H	1	2255	56.8-66.3	9.5	9.83	103.0	7R	4	1410	167.3-176.9	9.6	0.78	8.1		
8H	1	2345	66.3-75.8	9.5	9.86	104.0	8R	4	1550	176.9-186.5	9.6	2.11	22.0		
9H	2	0055	75.8-85.3	9.5	10.00	105.2	9R	4	1715	186.5-196.2	9.7	3.40	35.0		
10H	2	0140	85.3-94.8	9.5	9.96	105.0	10R	4	1845	196.2-205.8	9.6	3.87	40.3		
11H	2	0230	94.8-104.3	9.5	9.99	105.0	11R	4	2020	205.8-215.4	9.6	3.34	34.8		
12H	2	0315	104.3-113.8	9.5	9.25	97.3	12R	4	2155	215.4-225.1	9.7	3.90	40.2		
13H	2	0405	113.8-123.3	9.5	9.75	102.0	13R	4	2325	225.1-234.7	9.6	2.82	29.4		
14X	2	0455	123.3-129.1	5.8	7.87	135.0	14R	5	0105	234.7-244.3	9.6	2.75	28.6		
15X	2	0620	129.1-138.7	9.6	5.29	55.1	15R	5	0235	244.3-253.9	9.6	2.63	27.4		
16X	2	0825	138.7-148.3	9.6	1.35	14.0	16R	5	0420	253.9-263.5	9.6	3.69	38.4		
Coring totals:				148.3	142.1	95.8	17R	5	0550	263.5-273.1	9.6	2.31	24.0		
160-967B-							18R	5	0715	273.1-282.7	9.6	3.58	37.3		
1H	2	1055	0.0-5.3	5.3	5.33	100.0	19R	5	0850	282.7-292.3	9.6	0.95	9.9		
2H	2	1140	5.3-14.8	9.5	9.96	105.0	20R	5	1020	292.3-301.9	9.6	1.45	15.1		
3H	2	1225	14.8-24.3	9.5	9.89	104.0	21R	5	1150	301.9-311.6	9.7	1.28	13.2		
4H	2	1310	24.3-33.8	9.5	9.94	104.0	22R	5	1330	311.6-321.1	9.5	0.98	10.3		
5H	2	1355	33.8-43.3	9.5	10.00	105.2	23R	5	1455	321.1-330.8	9.6	0.40	4.2		
6H	2	1440	43.3-52.8	9.5	9.97	105.0	24R	5	1630	330.8-340.5	9.7	0.88	9.1		
7H	2	1530	52.8-62.3	9.5	9.92	104.0	25R	5	1805	340.5-350.1	9.6	3.70	38.5		
8H	2	1620	62.3-71.8	9.5	9.95	105.0	26R	5	1940	350.1-359.7	9.6	0.80	8.3		
9H	2	1710	71.8-81.3	9.5	10.02	105.5	27R	5	2110	359.7-369.3	9.6	0.48	5.0		
10H	2	1800	81.3-90.8	9.5	9.93	104.0	28R	5	2240	369.3-378.8	9.5	1.21	12.7		
11H	2	1855	90.8-100.3	9.5	9.94	104.0	29R	6	0015	378.8-388.4	9.6	1.90	19.8		
12H	2	1945	100.3-109.8	9.5	9.70	102.0	30R	6	0215	388.4-398.1	9.7	0.50	5.2		
13H	2	2030	109.8-119.3	9.5	9.89	104.0	31R	6	0345	398.1-407.7	9.3	0.10	1.1		
14H	2	2130	119.3-121.5	2.2	2.17	98.6	32R	6	0505	407.7-417.4	9.7	0.56	5.8		
Coring totals:				121.5	126.6	104.2	33R	6	0630	417.4-427.0	9.6	0.32	3.3		
160-967C-							34R	6	0750	427.0-436.6	9.6	0.09	0.9		
1H	3	0025	0.0-9.5	9.5	9.83	103.0	35R	6	0920	436.6-446.2	9.6	0.15	1.6		
2H	3	0105	9.5-19.0	9.5	9.81	103.0	36R	6	1105	446.2-455.9	9.7	0.11	1.1		
3H	3	0150	19.0-28.5	9.5	9.96	105.0	37R	6	1245	455.9-465.5	9.6	0.12	1.3		
4H	3	0235	28.5-38.0	9.5	9.95	105.0	38R	6	1415	465.5-475.1	9.6	0.00	0.0		
5H	3	0320	38.0-47.5	9.5	10.00	105.2	39R	6	1540	475.1-484.8	9.7	0.14	1.4		
6H	3	0405	47.5-57.0	9.5	10.02	105.5	40R	6	1715	484.8-494.4	9.6	0.00	0.0		
7H	3	0445	57.0-66.5	9.5	10.02	105.5	41R	6	1910	494.4-504.0	9.6	0.77	8.0		
8H	3	0525	66.5-76.0	9.5	10.00	105.2	42R	6	2130	504.0-513.6	9.6	0.09	0.9		
9H	3	0610	76.0-85.5	9.5	9.84	103.0	43R	6	2325	513.6-523.2	9.6	0.00	0.0		
10H	3	0650	85.5-95.0	9.5	10.13	106.6	44R	7	0105	523.2-532.8	9.6	0.06	0.6		
11H	3	0730	95.0-104.5	9.5	10.01	105.3	45R	7	0245	532.8-542.5	9.7	0.11	1.1		
12H	3	0815	104.5-109.7	5.2	5.22	100.0	46R	7	0440	542.5-552.1	9.6	0.15	1.6		
13H	3	0855	109.7-114.4	4.7	4.76	101.0	47R	7	0620	552.1-561.8	9.7	0.00	0.0		
Coring totals:				114.4	119.6	104.5	48R	7	0925	563.8-571.4	7.6	0.00	0.0		
160-967D-							49R	7	1125	571.4-581.0	9.6	0.11	1.1		
1H	3	1230	0.0-6.7	6.7	6.75	101.0	50R	7	1325	581.0-590.6	9.6	0.10	1.0		
2H	3	1320	6.7-16.2	9.5	10.14	106.7	51R	7	1525	590.6-600.3	9.7	0.07	0.7		
Coring totals:				16.2	16.9	104.2	Coring totals:								
160-967E-							488.4							72.3	14.8
160-967F-							9.5							9.9	104.0
160-967G-							9.5							9.9	104.0

and from Sections 160-967B-7H-4, 114 cm, through 7H-5, 63 cm (53.43-59.43 mbsf). These intervals are cut by faults and include slump folds (Fig. 12). The thicker (7.5 m) interval within Hole 967A contains a basal section with finely banded and laminated sediment and sapropels of variable thickness (Fig. 13A, B). This sequence is also seen in Hole 967B. In Hole 967A, the laminated/banded section is overlain by a 3-m-thick interval of yellowish brown sediment, which is in turn overlain by two sapropels. Neither of these intervals can be correlated with any other part of the sequence. In Holes 967A and 967B this deformed interval is overlain by a chaotic bed (80 cm thick in Hole 967A, 52 cm thick in Hole 967B) of clast-supported, rounded to angular fragments of unconsolidated nannofossil ooze, clay, and sapropel (Fig. 14A, B). In Hole 967B, this interval is overlain by a sapropel. In Hole 967C, the deformed sediments are absent, and this interval is represented only by a 144-cm-thick chaotic bed that resembles that in Holes 967A and 967B (Fig. 14A, B). The entire interval is interpreted to represent a sediment slide or slump unit, overlain by a debris-flow deposit. Intriguingly, the sequence in Hole

967A suggests a hiatus at the top of the slide interval, but the overlying sediments in Hole 967C appear to be older than those in Hole 967A, which rules out a common hiatus. It appears that the "debris flow" unit in the three holes may not be directly correlatable (see "Biostratigraphy and Sedimentation Rates" section, this chapter).

Sapropels

Eighty discrete centimeter- to decimeter-thick, dark gray (5Y 4/1) to very dark gray (5Y 3/1) or black (5Y 3/1) sapropels were identified in Unit I. These sapropels are obviously represented by decreasing peaks of spectroscopic reflectance at 550 nm (Fig. 10). Most of these beds can be correlated among the holes (Table 2). In composition, they are clay or foraminifer clay with up to 12% pyrite and organic matter (3%-17% TOC—see "Organic Geochemistry" section, this chapter). All contain variable amounts of volcanic glass, quartz, inorganic calcite, and plant fragments.

Many sapropels are finely laminated on a submillimeter scale. Some sapropels are interrupted by thin beds and laminae of millime-

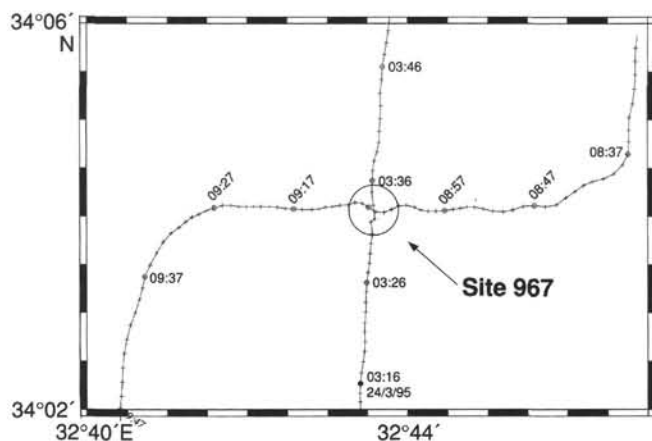


Figure 6. Track chart showing survey lines across Site 967.

ter- to centimeter-thick, homogeneous dark gray (N4) clay (see below). The occurrence of these intercalations is restricted to two intervals of the sedimentary succession (Fig. 8): 0–11 and 28–58 mbsf.

Within the top 10 m of the unit, several well-preserved sapropels may be tentatively correlated with the established Mediterranean sapropel nomenclature (McCoy, 1974). The topmost sapropel (S1) is 21 cm thick, contains pteropod shells, and is interrupted by a 2-cm-thick clay. Below this at 4.37 mbsf (Hole 967A), S2 is absent from this sequence. Sapropel S3 also contains pteropods, is 8 cm thick, and displays a 2-mm-thick dark clay bed, 1 cm from the base. A prominent pair of 4-cm-thick sapropels at 5.47 and 5.70 mbsf (Hole 967D) corresponds to sapropel S4 (Fig. 15). Sapropel S5 is 27 cm thick, laminated throughout, and contains three 2–15-mm-thick intercalations of dark gray (N4) clay (Fig. 16). The next sapropel found beneath S5 (presumably S6) is a 50-cm composite bed with a laminated basal section, containing several millimeter- to centimeter-scale interbeds of dark gray (N4) clay. The upper 20 cm contains foraminifer-rich intervals, of which the top 10 cm is highly bioturbated by *Planolites*. Two further, relatively thick (20 cm) sapropels containing laminated intervals occur between 9 and 10.5 mbsf. The remaining sapropel within this upper group at 11 mbsf is relatively thin (~5 cm) and is pervasively burrowed with *Chondrites*. The interval between 11 and 18 mbsf (Holes 967B and 967C, 12–20 mcd) contains only one correlatable sapropel, which is pervasively bioturbated by *Chondrites*.

The interval between 18 and 25 mbsf (Holes 967A, 967B, and 967C) (20–26 mcd) contains a group of seven relatively thin (2–6 cm) sapropels that are generally dark gray (5Y 3/1) and unlaminated and contain foraminifers. Some of these beds are strongly bioturbated by *Zoophycos* (rather than *Chondrites*). The interval between 25 and 31 mbsf (Hole 967A) (26–33 mcd) does not contain any sapropels.

From 31 to 88 mbsf (Hole 967A) (33–92 mcd) sapropels occur regularly in groups or “packets” of beds with a 50-cm spacing typically separating individual beds and with 1–2 m separating the packets. The most distinctive intervals free of sapropels occur between 57 and 61 mbsf (restricted to the slump interval in Hole 967A), between 70 and 76 mbsf (Hole 967A) (75–80 mcd), and between 79 and 81 mbsf (Hole 967A) (83–85.5 mcd). All these intervals contain yellowish brown (10YR 5/6) sediment.

The sapropels within the lower part of the sequence (lower Pliocene to lower Pleistocene) are typically between 5 and 20 cm thick and are variably bioturbated, generally by *Chondrites*. In some cases, only the upper part of the bed is affected (Fig. 17A, B); in others, the entire sapropel is pervasively burrowed (Fig. 18A, B). Many

of the sapropels, which are black or very dark gray in color, are underlain by 2–3 cm of paler colored (gray or dark gray) sediment. These intervals correspond to the “proto-sapropel” interval first proposed by Stanley and Maldonado (1979).

Turbidites

A number of distinctive interbeds occur within the upper 40 m of the nannofossil ooze and nannofossil clay of Unit I. The most common variety is color- and compositionally graded from gray (5Y 5/1) nannofossil clay (>50% clay) to grayish brown (10YR 5/2) or pale brown (10YR 6/3) clayey nannofossil ooze or nannofossil ooze (Fig. 19). They are typically between 2 and 10 cm thick, may occur in stacks of beds, and locally make up as much as 50% of the sequence. These beds are interpreted to be the deposits of low-density, clay-rich turbidity currents, with clay-rich bases grading up to into the “back-ground” deposition of nannofossil ooze.

The other, less common interbeds are composed mainly of uniform, dark gray (N4) clay. These are most commonly observed as millimeter- to 5-cm-thick intercalations within sapropels (Fig. 16). They also occur with sapropels and are more rarely graded from silty or sandy gray (N5) bases to dark gray (N5) clay, which may be up to 25 cm thick. One such sand at the base of a 24-cm-thick bed (Section 160-967D-1H-4, 140 cm) includes mica (both muscovite and biotite), which is characteristic of Nile-derived turbidites (Cita et al., 1984).

Ash

Three thin discrete ash layers, 0.5-, 3-, and 2-cm-thick, were identified in the upper part of Unit I (Sections 160-967A-1H-1, 35 cm, 0.35 mbsf; 1H-2, 35–38 cm; and 1H-7, 17–18 cm). Minor quantities (1%–3%) of volcanic glass are disseminated throughout the dominant lithology of Unit I.

Lithostratigraphic Unit II

Description: Nannofossil clay and nannofossil ooze with minor fragments of micritic limestone and inorganic calcite

Intervals: Sections 160-967A-11H-5 through 13H-4, Cores 160-967B-12H and 13H, 160-967C-12H and 13H, and 160-967E-1R and 2R

Depth: 100–119.3 mbsf, Hole 967A; 100.3–119.3 mbsf, Hole 967B; 104.5–114.4 mbsf, Hole 967C; 109.5–128.7 mbsf, Hole 967E

Age: early Pliocene to middle Pliocene

The lithology of Unit II is composed of intercalations of well-consolidated light brown (7.5YR 6/4) to very pale brown (10YR 7/3) nannofossil clay and nannofossil ooze containing silt to granule-sized fragments of micritic limestone and inorganic calcite. A number of foraminifer-rich graded beds, displaying distinctive sharp erosional bases, were identified in the upper part of the unit. These beds have been interpreted as turbidites.

The nannofossil component decreases downhole from 75% to 26% between 100 and 119.3 mbsf (Fig. 11). On the other hand, micritic rock fragments and clay increase from 0% to 40% and from 2% to 43%, respectively, through the same interval.

There was no core recovery in the interval between 120 and 125 mbsf. However, information derived from the FMS and gamma-ray downhole tools indicates the presence of gypsum in that interval (see “Downhole Measurements” section, this chapter).

Lithostratigraphic Unit III

Description: Foraminifer nannofossil chalk

Intervals: Section 160-967A-13H-4 through Core 16X, 160-967B-14H, and 160-967E-3R through 33R

Depth: 119.3–140.05 mbsf, Hole 967A; 119.3–121.5 mbsf, Hole 967B; 128.7–427.0 mbsf, Hole 967E

Age: Late Cretaceous (Campanian) to middle Eocene

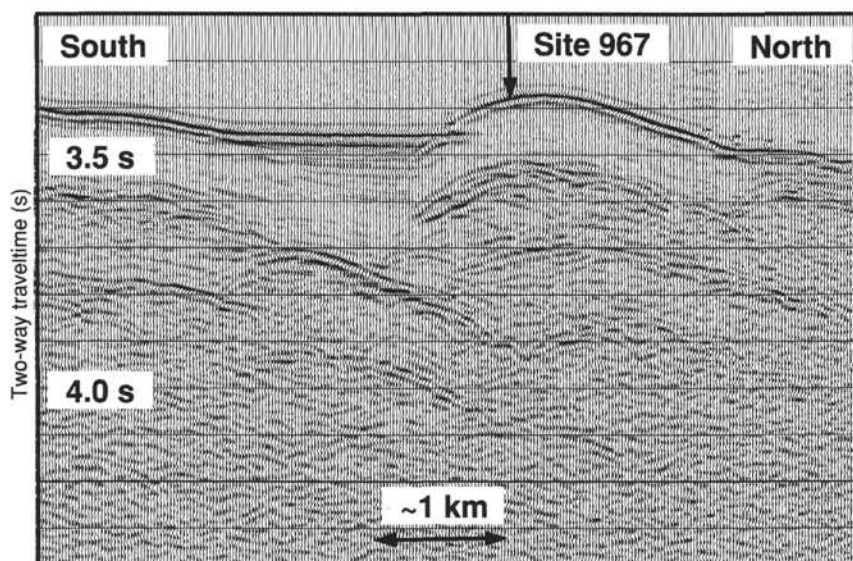


Figure 7. South to north seismic line across Site 967 showing the asymmetric structure drilled.

The lithology of Unit III is dominated by burrow-mottled and well-lithified foraminifer nannofossil chalk. Some intervals have intercalated layers of finely burrowed nannofossil chalk and thin intervals of dark organic-rich, laminated calcilitite. The color of the chalk varies from white (5Y 8/1, 10YR 8/1) to light gray (10YR 7/1, 10YR 7/2, and 5Y 7/1) and pale green (10Y 7/1). Fine-scale color banding was commonly observed.

The chalk includes concentrations of planktonic and benthic foraminifers and small particles (<2 mm) of glauconite, which are concentrated in some intervals. Inorganic calcite is predominant (up to 80%) below 120 mbsf and coincides with a decreasing nannofossil content (Fig. 11). Mollusk shells and rare crinoid ossicles occur in several intervals. Burrows of *Planolites*, *Chondrites* (Fig. 20), *Zoophycos* (Fig. 21), and *Teichichnus* occur with sporadic purplish halos around the burrows. Millimeter-thick, bed-parallel laminations are present in the chalk and some are gently inclined. Fine ripple lamination and discrete thin layers containing foraminifer concentrates are locally developed.

The nannofossil chalk also contains dark gray (N6) nodules of chert (Cores 160-967E-8R, 9R, and 13R). There is abundant disseminated pyrite and scattered small (from 1 to 2 mm) pyrite nodules. Black chert micronodules containing pyrite (Fig. 22) and a thin bed of glauconite and pyrite-rich sand occur in Core 160-967E-17R (263.5–273.1 mbsf). Glauconite grains are disseminated throughout the interval between 340.5 and 350.1 mbsf (Core 160-967E-25R), and finely laminated, black bituminous limestone is present between 369.3 and 378.8 mbsf (Core 160-967E-28R). Fractures and faults occur sporadically (Fig. 23) (see “Structural Geology” section, this chapter).

Lithostratigraphic Unit IV

Description: Well-cemented shallow-water limestone
Interval: Cores 160-967E-34R through 42R
Depth: 427.0–504.16 mbsf
Age: Late Cretaceous to early Pliocene

Core recovery in Unit IV was very low (1.5% on average).

The top of Unit IV is defined by the first appearance of porous biosparite with calcareous algae and mollusk fragments as the dominant clasts. In Core 160-967E-39R (475.1–484.8 mbsf), coral and encrusting red algae dominate. The color of the limestone varies from

white (10YR 8/1) to light gray (10YR 7/2) and very pale brown (10YR 7/3).

Finely laminated, black bituminous limestone is present in Core 160-967E-35R (436.6–446.2 mbsf) and crinoid ossicles are rarely present. Fractures and faults occur throughout the lowest interval in the unit (see “Structural Geology” section, this chapter).

Lithostratigraphic Unit V

Description: Brecciated limestone
Interval: Cores 160-967E-44R through 51R
Depth: 504.16–590.69 mbsf
Age: Late Cretaceous

Core recovery in Unit V averaged 0.5%.

The lithology of the unit is dominated by white (10YR 8/1) to light gray (10YR 7/2) pervasively brecciated limestone (see Figs. 41, 42 in “Structural Geology” section, this chapter). It is composed mainly of angular clasts, which are typically less than 3 cm, within a very dark gray (10YR 3/1) fine-grained matrix. Fragments recovered from the upper part of the unit include light gray (5Y 7/2) to gray (5Y 5/1) chert and very pale brown (10YR 7/4) calcarenite. Some pieces of fine-grained light brownish gray (10YR 6/2) calcarenite contain some traces of primary lamination. The brecciated limestone includes a small number of clasts of light gray (10YR 7/2) sheared calcarenite, some of which are cut by fractures. Within these rocks some slickensided surfaces are present (see “Structural Geology” section, this chapter).

Depositional History

The depositional history of the succession recovered at Site 967 involves both shallow- and deep-water accumulation processes.

The succession above the limestones is relatively complete except for a short hiatus at the end of the late Pliocene. The age of the limestone is known with reasonable certainty to about 380 mbsf (Core 160-967E-29R); beyond that depth the age is inferred as syn- or pre-Late Cretaceous.

Using the lithologic composition of the limited core recovery, the following is tentatively proposed.

Sometime during the syn- or pre-Late Cretaceous a shallow-water limestone succession was deposited (Unit IV). Subsidence allowed a

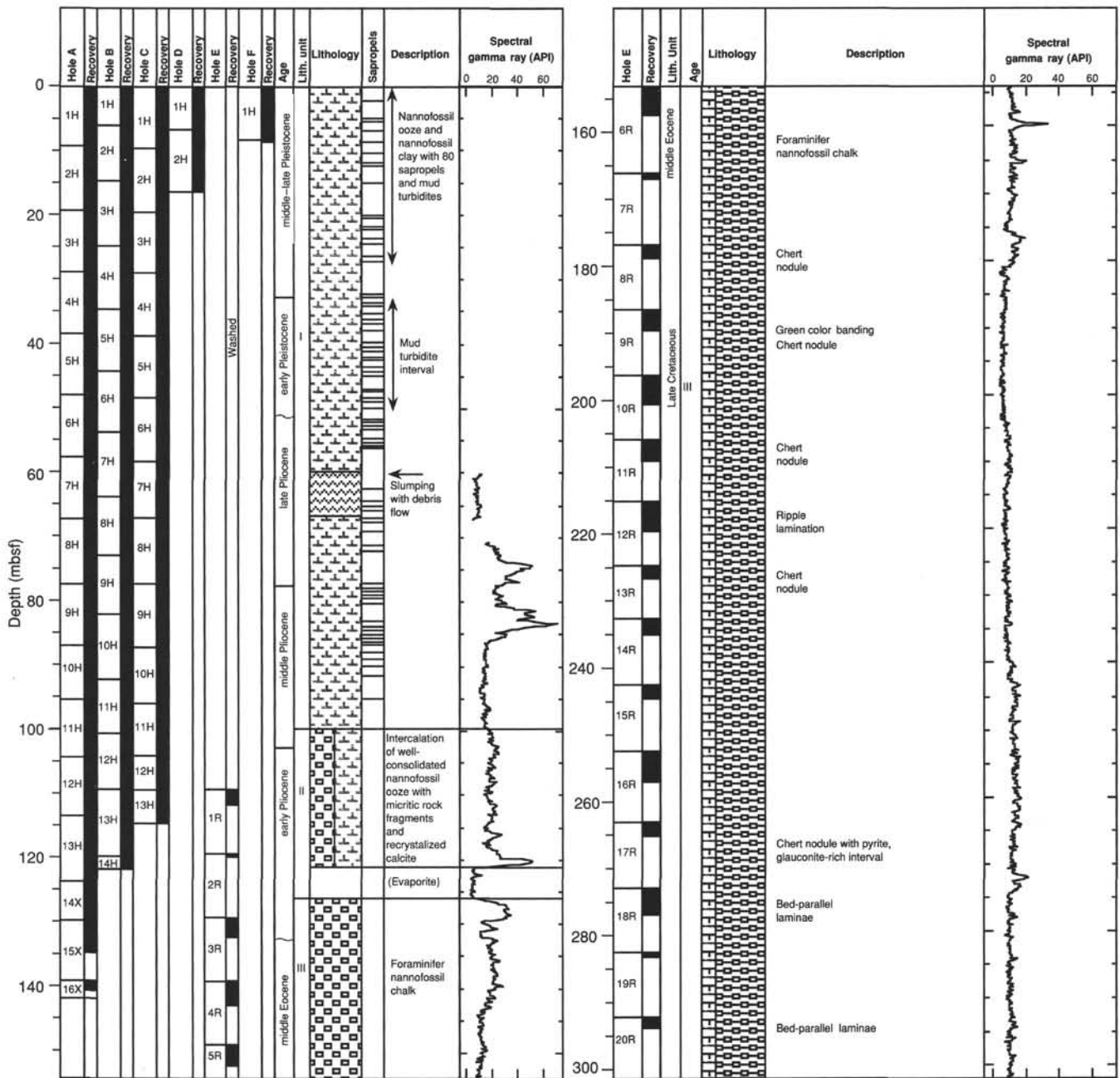


Figure 8. Core recovery, lithostratigraphic summary, and age information for Site 967. Within intervals of poor core recovery, references in parentheses are from the downhole measurement data.

sequence of foraminifer and nannofossil biomicrites to accumulate conformably in deep water during the Late Cretaceous through the middle Eocene (Unit III).

Deep-water pelagic carbonate deposition ended some time during or after the middle Eocene. There is then a gap in the record until the early Pliocene. However, in the intervening thin interval, planktonic microfossils of middle Miocene, Oligocene, and late Miocene to early Pliocene age were recovered (see "Biostratigraphy and Sedimentation Rates" section, this chapter). This indicates that some deep-water sedimentation took place in the vicinity of Site 967. At some time, possibly in the late Miocene, the underlying sediments were uplifted and surface exposure took place, perhaps involving faulting. Gypsum accumulated presumably in the Messinian. Deep-water dep-

osition ensued through the early Pliocene, following tectonic subsidence and transgression at the end of the Messinian desiccation crisis, and has continued with the accumulation of sapropels and mud turbidites (of possible Nile derivation) through the Pleistocene to Holocene.

BIOSTRATIGRAPHY AND SEDIMENTATION RATES

Calcareous Nannofossils

Calcareous nannofossils were studied from core-catcher samples collected from Holes 967A, 967C, 967D, and 967E. To provide high-

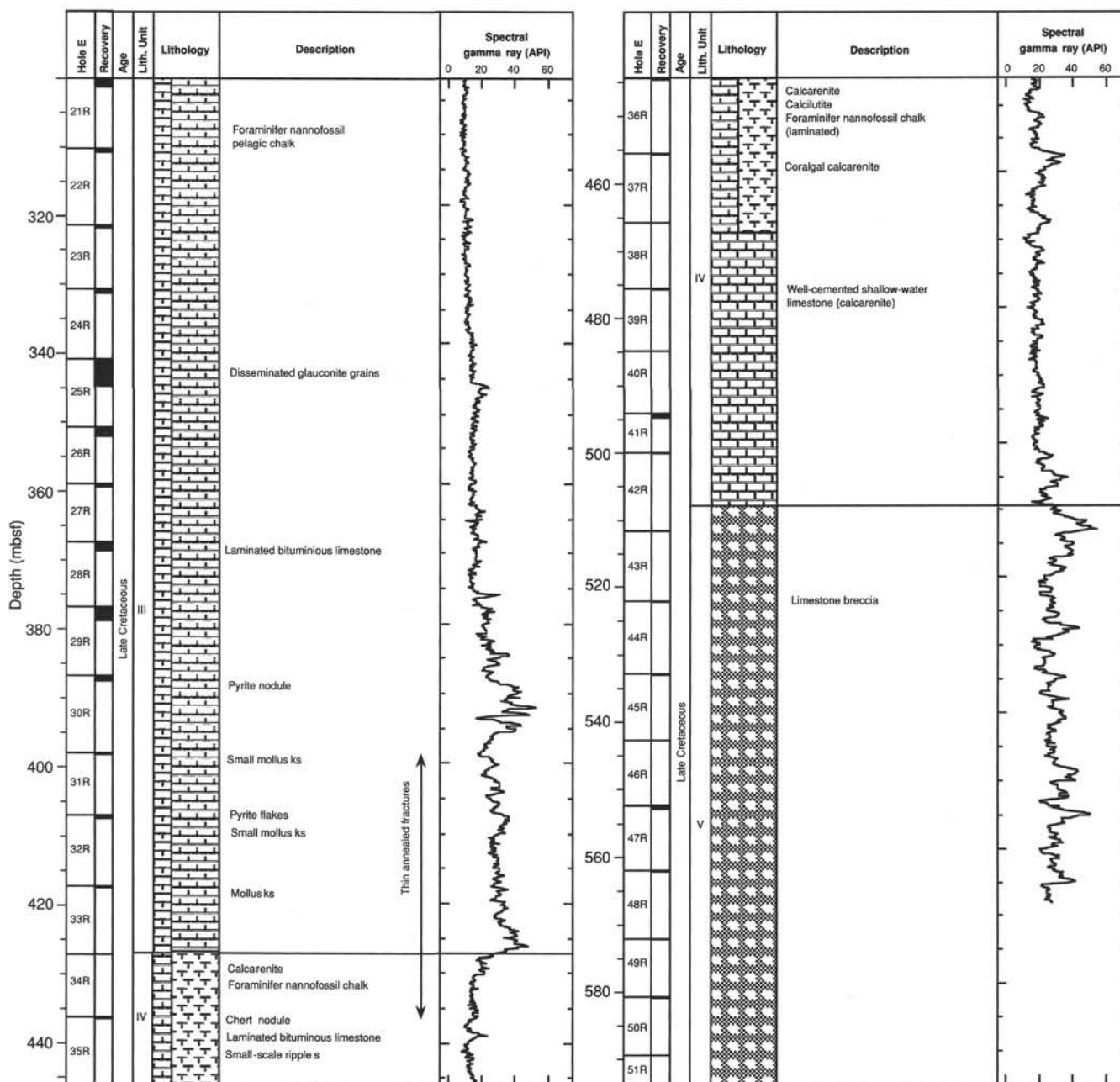


Figure 8 (continued).

er resolution biostratigraphy, additional samples were collected from each section of core that contained sediment or lightly indurated rock from Hole 967A. The age of the samples analyzed ranges from latest Pleistocene to late Santonian. Miocene, Oligocene, and upper Eocene rocks are not present at Site 967.

Hole 967A

The calcareous nanofossil biostratigraphy from Hole 967A is typified by assemblages that range from the Pleistocene through middle Eocene age. Calcareous nanofossils are abundant or common in all of the samples analyzed from 0 to 116 mbsf. Below 116 mbsf, abundance is variable with some barren intervals present. Preservation varies from very good in the Pleistocene and upper Pliocene sed-

iments to poor in some oozes and chalks associated with lower Pliocene and Eocene samples. Reworking is variable and consists of Pliocene-Miocene, Eocene, Paleocene, and Cretaceous age taxa. A summary of the biostratigraphy is described below and displayed in Figure 24.

The base of the first biozone (MNN21) was detected in Sample 160-967A-1H-CC. This zone is defined by the presence of *Emiliana huxleyi* in quantities lower than those of the acme zone, which was not identified upsection. The accompanying assemblage includes small *Gephyrocapsa* (<3.5 μm), *Gephyrocapsa oceanica* s.l., *Helicosphaera kamtneri*, *Coccolithus pelagicus*, *Rhabdosphaera clavigera*, and *Pontosphaera japonica*.

Samples 160-967A-2H-1, 130 cm, through 2H-6, 96 cm, were placed into Zone MNN20, which is a gap zone defined by the absence

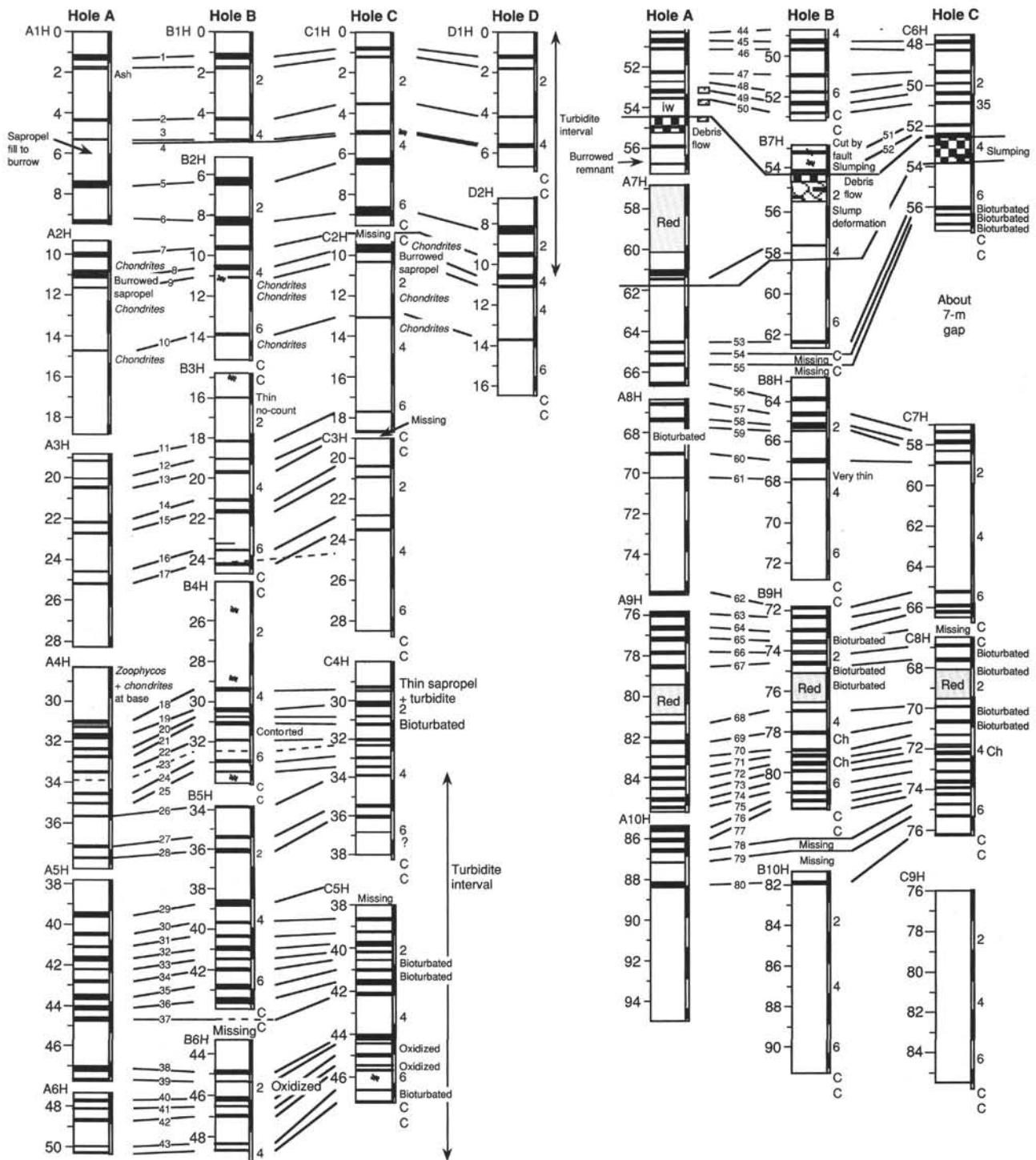


Figure 9. Correlation among the five holes drilled at Site 967. The shaded bar on the right-hand side of the schematic indicates the intervals of each hole used to compile the composite lithologic spliced section.

of both *E. huxleyi* and *Pseudoemiliania lacunosa*. The accompanying assemblage is similar to that found uphole.

Samples 160-967A-2H-CC through 4H-3, 132 cm, contain nanofossils from Zone MNN19f. The upper boundary of the zone is defined by the last occurrence of *P. lacunosa*, whereas the lower boundary is defined by the first occurrence of *Gephyrocapsa* sp. 3. *Gephyrocapsa* sp. 3 is located in Sections 160-967A-2H-5 through

4H-3, 132 cm. The accompanying assemblage is similar to that of the preceding zone.

Samples 160-967A-4H-4, 13 cm, through 4H-CC contain nanofossils from Zone MNN19e. This interval is interpreted as a gap zone identified by the absence of *Gephyrocapsa* sp. 3 and large *Gephyrocapsa* (>5.5 μm). Small *Gephyrocapsa* and *P. lacunosa* dominate the accompanying assemblage.

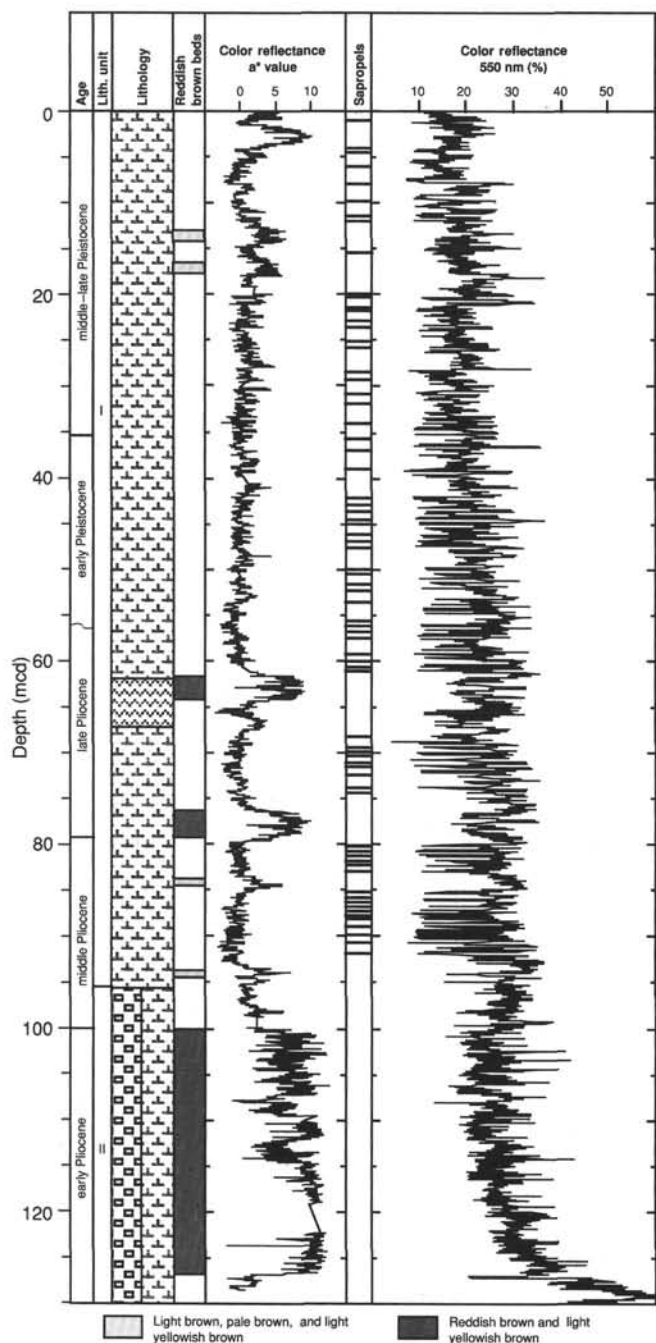


Figure 10. Spliced lithostratigraphic composite section. Columns indicate, from left to right: age; unit; lithologic summary; location of reddish brown beds indicating intervals where the sediment ranges from light brown (10YR 6/3) to reddish brown (5YR 5/4); color reflectance a^* value (values greater than zero indicate a red chroma); location of sapropels; and color reflectance at 550 nm. Each of the 80 sapropels is represented by a minimum, having about 10% reflectance, at the 550-nm band. The reddish brown intervals may be divided into two groups of different color: (1) light brown (10YR 6/3), pale brown (10YR 6/3), and light yellowish brown (10YR 6/4) and (2) reddish brown (5YR 5/4) and light yellowish brown (10YR 6/4). The light brown intervals (1) have also been identified at Sites 964 and 966.

Samples 160-967A-5H-1, 135 cm, through 5H-7, 45 cm, contain nannofossils from Zone MNN19d. This zone is identified by the presence of large *Gephyrocapsa* ($>5.5 \mu\text{m}$). The accompanying assemblage is dominated by small *Gephyrocapsa*, *P. lacunosa*, and *G. oceanica* s.l.

Samples 160-967A-6H-1, 120 cm, and 6H-2, 120 cm, contain nannofossils from Zone MNN19c. This zone is a gap zone defined by an absence of both *Calcidiscus macintyreii* and large *Gephyrocapsa* ($>5.5 \mu\text{m}$). Small *Gephyrocapsa* and *G. oceanica* s.l. dominate the assemblage.

Samples 160-967A-6H-3, 20 cm, through 6H, 130 cm, contain nannofossils from Zone MNN19a. This interval is a gap zone identified by absence of both *G. oceanica* s.l. and *Discoaster brouweri*. Zone MNN19b, which contains both *G. oceanica* s.l. and *C. macintyreii*, is missing. Therefore, the boundary between Zones MNN19a and MNN19c in Hole 967A represents an absence of approximately 0.1–0.6 m.y. of the geologic record owing to a hiatus or unconformity. The accompanying assemblage is diverse and includes *P. lacunosa*, *H. kamptneri*, small *Gephyrocapsa*, *Syracosphaera pulchra*, and small reticulofenestrads.

Samples 160-967A-6H-7, 21 cm, through 8H-5, 120 cm, contain nannofossils from Zone MNN18. In this zone, *D. brouweri* and *Discoaster triradiatus* occur in the absence of both *Discoaster pentaradiatus* and *G. oceanica* s.l. In Core 160-967A-7H nannofossil abundance and preservation diminish owing to the presence of turbidites. The accompanying assemblage is similar to that of the previous zone.

Samples 160-967A-8H-6, 120 cm, through 9H-3, 130 cm, contain nannofossils from Zone MNN17–16b. This zone is recognized as the interval between the last occurrence of *D. pentaradiatus* and the last common occurrence of *Discoaster tamalis*. The accompanying assemblage includes small *Gephyrocapsa*, *D. brouweri*, *Discoaster surculus*, *Discoaster intercalaris*, and small reticulofenestrads.

Samples 160-967A-9H-4, 130 cm, through 11H-6, 30 cm, contain nannofossils belonging to Zone MNN16a. This zone is identified by the common occurrence of *D. tamalis* above the last occurrence of *Reticulofenestra pseudoumbilicus*. The accompanying assemblage is similar to that found in the preceding zone.

Samples 160-967A-11H-7, 30 cm, through 12H-4, 23 cm, contain nannofossils belonging to Zone MNN14–15. The abundance of *Discoaster asymmetricus* varies from few to absent in these samples and makes placement of the lower boundary of this zone tenuous. The accompanying assemblage is similar to that found in the preceding zone, with common to few specimens of *D. surculus* observed.

Samples 160-967A-12H-5, 20 cm, through 12H-6, 30 cm, contain nannofossils belonging to Zone MNN13. This zone is identified by the presence of *Helicosphaera sellii* below the common occurrence of *D. asymmetricus*. Additional changes from the preceding zone include the disappearance of *P. lacunosa* and small *gephyrocapsids* and an increase in calcite overgrowths on discoasters. A few specimens of *Amaurolithus delicatus* are also present in some samples.

Sample 160-967A-13H-1, 77 cm, is the lowermost sample that can be confidently placed into a Pliocene zone. This sample contains a moderately preserved assemblage that includes *A. delicatus*, *D. surculus*, *D. pentaradiatus*, *Discoaster variabilis*, *Sphenolithus abies*, *R. pseudoumbilicus*, and *Amaurolithus tricorniculatus*. *H. sellii* does not occur in the assemblage, which places this sample into Zone MNN12.

The interval between Samples 160-967A-13H-1, 77 cm, and 14X-3, 64 cm, is problematic because of severe overgrowths of calcite on many specimens and a general decline in abundance. The nannofossils are not age diagnostic in this interval.

From Samples 160-967A-14X-2, 76 cm, through 16X-CC, the nannofossils exhibit both variable abundance and preservation. Some of the samples are barren to rare and poorly preserved, whereas others have few, moderately preserved nannofossils. The assemblage in-

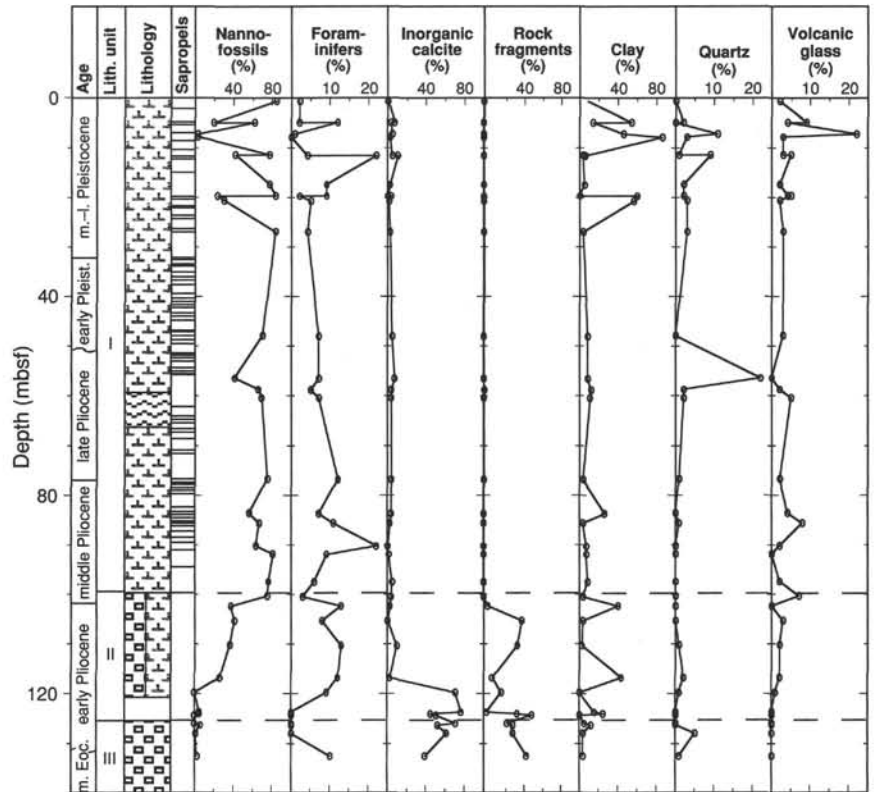


Figure 11. Smear-slide data of dominant sedimentary components in the upper 140 m of Hole 967A.

cludes *Ericsonia formosa*, *Cyclicargolithus floridanus*, *Dictyococites bisecta*, *Discoaster saipanensis*, *Discoaster barbadiensis*, and a calcite-overgrown chiasmolith that is interpreted as *Chiasmolithus grandis*. This assemblage is tentatively placed into the combined middle Eocene Zones NP15–16. However, this interpretation does not agree with foraminiferal interpretations that show the presence of Oligocene/Miocene and early Pliocene age species in samples from the same intervals. For this reason, Figure 24 shows the age of these samples as early Pliocene.

Hole 967C

Thirteen core-catcher samples were studied from Hole 967C. These samples were placed into zonations and compared with interpretations of samples collected from each section in Hole 967A. Generally, the two records agree; however, discrepancies in depth and overlaps occur in some zones (Fig. 25). These inconsistencies can be attributed to either incorrect depths that do not account for unrecovered material (see “Composite Depths” section, this chapter) or incorrect identification of gap zones in the Pleistocene portion of the sequence. In either case, shore-based studies should account for these discrepancies through additional biostratigraphic work and composite section correlations.

Hole 967D

Hole 967D consists of only two core-catcher samples from the middle-upper Pleistocene. Sample 160-967D-1H-CC contains rare quantities of *E. huxleyi* and was placed into Zone MNN21 (Fig. 25). Sample 160-967E-2H-CC is dominated by *G. oceanica* s.l. and small *Gephyrocapsa*, but does not contain *E. huxleyi*. This sample was placed into Zone MNN20.

Hole 967E

Hole 967E recovered rocks and sediments from 51 cores. The hole was washed to 109.5 mbsf and rotary drilled to a total depth of 600 mbsf. From approximately 109.5 to 390 mbsf, moderately to poorly preserved nannofossils were recovered. Most of the samples could be zoned. Cores below 390 mbsf either contain nannofossils that could not be distinguished to the species level or are devoid of nannofossils. None of the cores below Core 160-967E-30H was assigned to a nannofossil zonation.

Sample 160-967E-1R-CC contains an assemblage that includes *A. delicatus*, *D. surculus*, *D. pentaradiatus*, *D. variabilis*, *S. abies*, and *R. pseudoumbilicus*. *A. tricorniculatus* and *Amaurolithus primus* were not observed in this sample; therefore, the sample was placed in Zone MNN13. Reworked Paleogene species of *C. floridanus* and *D. bisecta* were also observed.

No samples were analyzed from Core 160-967E-2R. Sample 160-967E-3R-CC contains a chalk with an assemblage that includes *D. barbadiensis*, *D. saipanensis*, *E. formosa*, *Reticulofenestra umbilica*, and *Discoaster deflandrei*. The nannofossils in this core were placed in middle Eocene Zone NP16–17. Because this sample contains early Pliocene age foraminifers, Figure 24 shows this interval as early Pliocene in age.

Section 160-967E-4R-CC was not analyzed. Samples 160-967E-5R-CC through 7R-CC contain nannofossils similar to those from the preceding zone, with the addition of a calcite-overgrown chiasmolith that is interpreted to be *C. grandis*. This assemblage is tentatively placed into Zone NP16–15.

Beginning in Sample 160-967E-8R-CC, a Late Cretaceous assemblage occurs. The nannofossils are moderately to poorly preserved and abundance is variable. Diversity is low, which together with severe overgrowths of calcite on some taxa, suggests that selec-

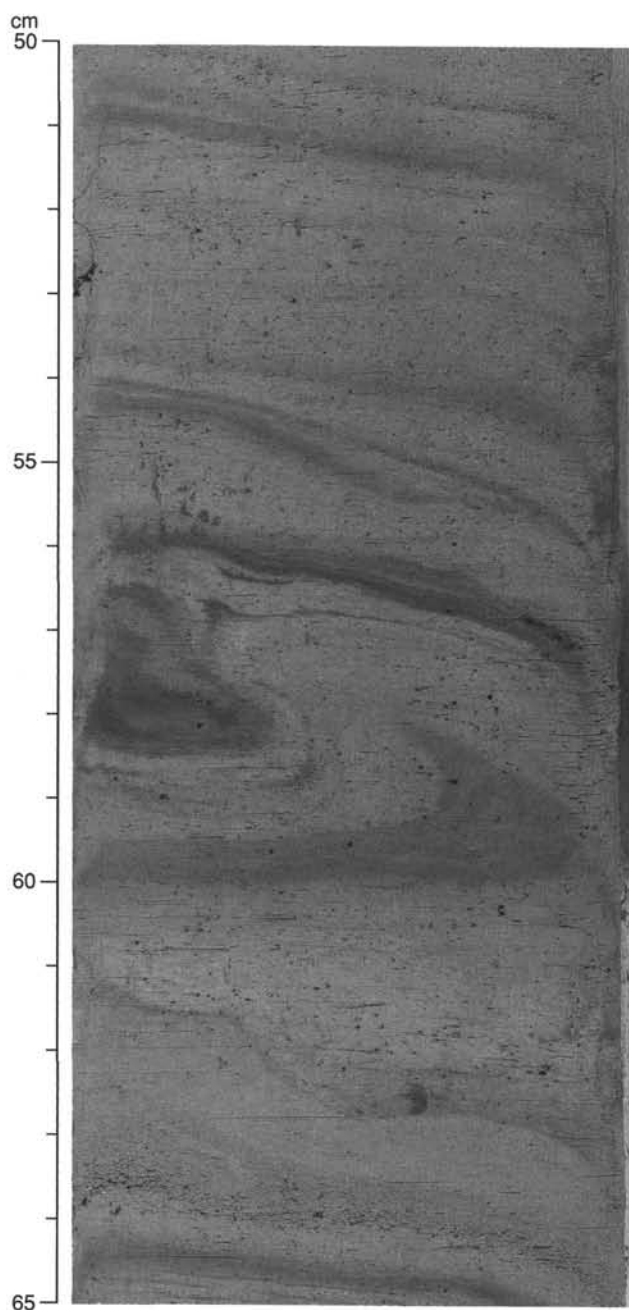


Figure 12. Example of the distinctive intervals of deformed sediments, cut by faults and including slump folds in Hole 967A (Section 160-967A-7H-3, 50–65 cm).

tive dissolution has most likely affected the assemblage. Sample 160-967E-8R-CC contains *Micula murus* and an accompanying assemblage that includes *Arkangelskiella cymbiformis*, *Micula decussata*, *Watzernaria barnesae*, *Prediscosphaera cretacea*, and *Microrhabdulus decoratus*. This assemblage was placed in the uppermost Mastrichtian Zone NC23.

Sample 160-967E-9R-CC contains the same poorly preserved assemblage as above, with the addition of *Lithraphidites quadratus*. This assemblage was placed in Zone NC22.

Samples 160-967E-10R-CC through 13R-CC contain an assemblage similar to the preceding Cretaceous zones without the markers *M. murus* or *L. quadratus*. This assemblage results in a placement of these samples in gap Zone NC21.

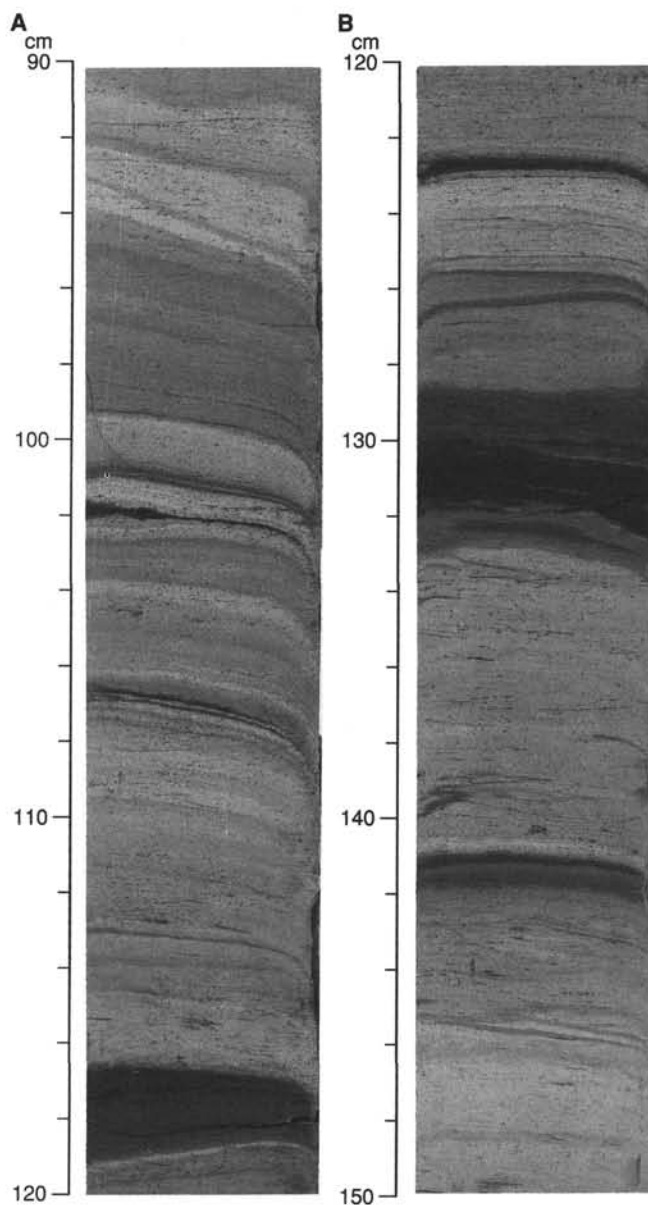


Figure 13. Examples of the interval within Hole 967A (A. Section 160-967A-7H-3, 90–120 cm; B. Section 160-967A-7H-3, 120–150 cm) containing a basal section with finely banded and laminated sediment and variably thick sapropels.

Samples 160-967E-14R-CC through 17R-CC contain a slightly more diverse assemblage than those from uphole and include *Quadrum trifidum*. Additional nannofossils identified from these samples include the same species as described above with *Lucianorhabdus cayeuxii*, *Lithraphidites carniolensis*, and *Quadrum gothicum*. These samples were placed into Zone NC20.

No samples were analyzed from Core 160-967E-18R. Core 160-967E-19R did not contain *Q. trifidum*, but otherwise contained an assemblage similar to that of the samples uphole. The absence of *Q. trifidum* indicates that this sample, and probably Core 160-967E-18R, is within Zone NC19b.

Cores 160-967E-20R and 21R do not contain *Q. gothicum*, but still contain *Ceratolithoides aculeus*. Therefore, these samples were placed into Zone NC19a. *Aspidolithus parvus*, which is a consistent part of the assemblage uphole, was not seen below Sample 160-967E-23R-CC. The first occurrences of *C. aculeus* and *A. parvus* are

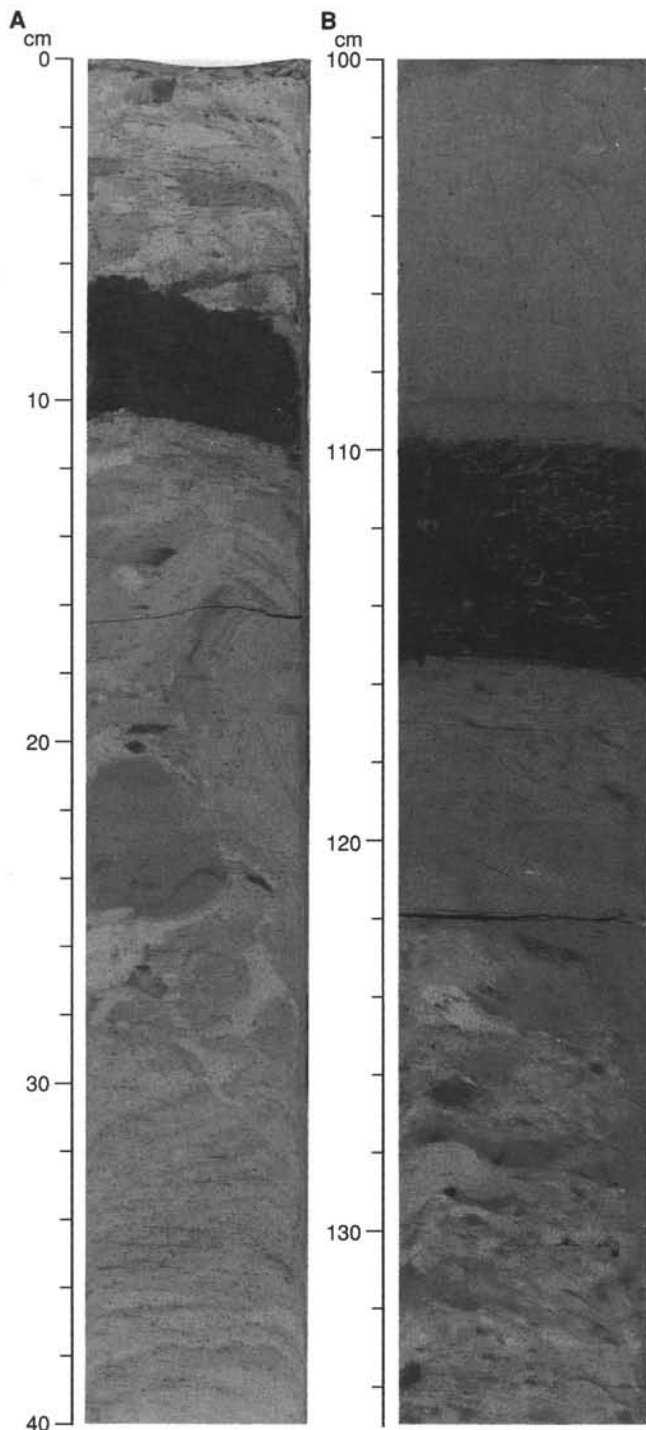


Figure 14. Examples of the chaotic bed in Holes 967A and 967B of clast-supported, rounded to angular fragments of unconsolidated nanofossil ooze, clay, and sapropel. **A.** Section 160-967A-6H-6, 0–40 cm. **B.** Section 160-967B-7H-1, 100–135 cm.

both late Campanian markers and serve as boundaries for the tops of Zones NP18 and NP17, respectively. The accompanying assemblage is similar to that of previous samples without species of *Quadrum*.

The next significant change in assemblage occurs in Sample 160-967E-27R-CC, where nannofossils were observed. Below this sample, *A. cymbiformis* is absent from the assemblage. The first occur-

rence of *A. cymbiformis* is an event in NP17; however, this event is very close to the first occurrence of *A. parvus*. The data from Hole 967E show these events to be four cores apart. This peculiarity raises suspicion that the first occurrence of the *A. parvus* datum may be placed at too high a level in this hole.

The last occurrence of *Eprolithus floralis* was the last event observed. As with *A. cymbiformis*, this event occurs usually within Zone NC17 near *A. parvus*, but was instead seen in Sample 160-967E-30R-CC.

Planktonic Foraminifers

Hole 967A was studied in detail in order to provide a complete stratigraphic record of the sedimentary sequence, and all core catchers containing suitable sediments for planktonic foraminiferal studies were analyzed, together with 91 additional samples. In addition, a few samples from Core 160-967C-6H and core catchers and samples from Hole 967E were also analyzed for their planktonic foraminiferal content.

Planktonic foraminifers range in abundance from absent in the lower part of the section to dominant at Site 967, as previously observed for Site 966. They consist of diversified and poorly to well-preserved Pleistocene and Pliocene faunas. According to the zonation scheme of Cita (1975) emended by Sprovieri (1993), the interval spanning the *Truncorotalia truncatulinoides excelsa*–*Globigerina cariacensis* Zones was identified for the Pleistocene, and seven zonal boundaries were identified for the Pliocene that encompass Zones MPL6 through MPL2 (Fig. 24). The sediments recovered in the lower part of the sequence contain a mixed assemblage of middle Eocene, Oligocene, early and late Miocene, and/or Pliocene age faunas, according to the zonation schemes of Blow (1979), Iaccarino (1985), and Spezzaferri (1994).

Hole 967A

As observed at Sites 963–966, the Pleistocene sequence cannot be zoned because the boundary between the *Truncorotalia truncatulinoides excelsa* and *Globigerina cariacensis* Zones was not recognized owing to the scarcity of *T. truncatulinoides excelsa*. However, the latter species is more continuously present at Hole 967A and occurs down to Sample 160-967A-4H-2, 103–106 cm. Faunal assemblages are generally well preserved and abundant and highly similar to those observed at Sites 963–966.

The highest Pliocene assemblages occur in Sample 160-967A-6H-3, 59–61 cm, based on the presence of the Pliocene taxon *Globigerinoides extremus*. An abundance increase in sinistral *Neogloboquadrina pachyderma*, marking the upper boundary of Zone MPL6, was not identified in Hole 967A. The lowest occurrence of *Globorotalia inflata*, which normally marks the base of Zone MPL6, was identified in Sample 160-967A-6H-2, 79–81 cm, above the highest occurrence of *G. extremus*. This indicates that this zone may be missing, as corroborated by the presence of debris flows within the interval (see “Lithostratigraphy” section, this chapter).

The upper boundary of Zone MPL5b was tentatively identified in Sample 160-967A-6H-3, 59–61 cm, by the first occurrence of the Pliocene species *G. extremus*, and its lower boundary was identified by the last occurrence of *Globorotalia bononiensis* in Sample 160-967A-8H-4, 55–57 cm.

Samples 160-967A-8H-5, 55–57 cm, through 10H-3, 69–61 cm, contain *G. bononiensis* and are attributed to Zone MPL5a.

The highest occurrence of *Sphaeroidinellopsis* spp. in Sample 160-967A-10H-4, 69–71 cm, marks the top of MPL4b. This zone was identified through Sample 160-967A-11H-5, 68–70 cm.

Zone MPL4a was identified from Samples 160-967A-11H-5, 128–130 cm, through 12H-1, 65–67 cm. Its top is marked by the highest occurrence of *Globorotalia puncticulata*.

The highest occurrence of *Globorotalia margaritae* and the lowest occurrence of *G. puncticulata* identify Zone MPL3 from Samples 160-967A-12H-2, 61–63 cm, through 12H-4, 71–73 cm.

Samples 160-967A-12H-5, 61–63 cm, through 13H-1, 77–79 cm, were attributed to Zone MPL2 based on the absence of *G. puncticulata*.

Samples 160-967A-13H-2, 67–69 cm, through 13H-4, 68–70 cm, contain Zone MPL1, based on the absence of *G. margaritae*. The lowermost Pliocene was tentatively identified in Hole 967A, based on the *Sphaeroidinellopsis* acme occurring in Sample 160-967A-13H-3, 69–71 cm.

Pliocene planktonic foraminiferal assemblages do not display significant changes throughout the sequence with respect to the previous holes, with the exception of the presence or absence of marker species of each biozone and climatically induced variations in faunal abundances.

Samples from Cores 160-967A-14X and 15X contain an interval nearly barren of planktonic foraminifera. Only a few non-age-diagnostic specimens of *Turborotalia quinqueloba*, *Orbulina universa*, and *Zeaglobigerina nepenthes* are present. Samples 160-967A-15X-CC through 16X-CC contain mixed middle Eocene, Oligocene, early Miocene, and early Pliocene age assemblages.

Hole 967C

Five samples were analyzed from Core 160-967C-6H (Samples 160-967C-6H-3, 10–12 cm, 6H-3, 68–70 cm, 6H-3, 123–125 cm, 6H-4, 14–16 cm, and 6H-4, 36–38 cm) to provide a more precise correlation of the sapropels identified in this hole (see “Lithostratigraphy” section, this chapter). All the analyzed samples contain *G. inflata* in the absence of the calcareous nannofossils *G. oceanica* s.l. and *D. brouweri*; hence, their assignment was made to Zone MPL6 (foraminifera) and MNN19a (nannofossils). These samples represent the uppermost Pliocene interval, which is missing in Hole 967A. Therefore, the depositional hiatus identified in Hole 967A is reduced in magnitude in Hole 967C.

Hole 967E

The Pliocene-Quaternary sedimentary sequence and the underlying middle Eocene sediments are separated at Site 967 by a hiatus extending from the Miocene to the upper Eocene (Fig. 24).

As observed for the lower part of the sedimentary sequence in Hole 967A, Samples 160-967E-3R-CC and 4R-CC contain a mixed middle Eocene, Oligocene, early and late Miocene, and/or early Pliocene age assemblage.

Sample 160-967E-5R-CC contains a planktonic foraminiferal assemblage attributed to the interval from Zones P11 to P14, consisting of *Globigerinatheka subconglobata*, *Globigerinatheka index*, *Acarinina rugosoaculeata*, *Acarinina rotundimarginata*, *Planorotalites pseudoscutulus*, and the *Acarinina bulbrooki* group.

Zone P11 was identified in Samples 160-967E-6R-CC and 7R-CC based on the presence of *Morozovella aragonensis*, *Truncorotaloides lybiaensis*, *A. bulbrooki*, and *Acarinina brodermanni*.

A second, extended hiatus separating middle Eocene and Upper Cretaceous sediments was identified in Hole 967E.

An Upper Cretaceous (upper Santonian to Maastrichtian) sedimentary sequence was recovered from Cores 160-967E-8R through 30R. Planktonic foraminiferal faunas are generally moderately diversified and well- to moderately preserved throughout the sequence. Only a few intervals, confined to the lower part of the sequence, are devoid of planktonic foraminifera (Fig. 24).

Five planktonic foraminiferal biozones were identified according to the zonal scheme of Erba et al. (in press). Ranges of some taxa follow those of Caron (1985). Although the four Zones *Contusotruncana contusa*–*Racemiguembelina fructicosa*, *Gansserina gansseri*,

Globotruncanella havanensis, and *Globotruncanella elevata* have not been identified, the sequence does not show significant hiatuses, and the zones may be only apparently missing owing to the spaced sampling.

The *Abathomphalus mayaroensis* Zone was identified from Samples 160-967E-8R-CC through 10R-CC. The marker species is present, together with common *Rugoglobigerina rugosa*, *Rugoglobigerina hexacamerata*, *Globotruncanella stuartiformis*, *Globotruncanella stuarti*, *Globotruncana aegyptiaca*, *Heterohelix globulosa*, and *Heterohelix striata* and rarely *C. contusa*, *Globotruncana fornicata*, and *Racemiguembelina fructicosa*.

The zonal boundary between *G. gansseri* and *G. aegyptiaca* was not observed owing to the scarcity of *G. gansseri*. This interval was identified from Samples 160-967E-11R-CC through 18R-1, 51–53 cm. The planktonic foraminiferal assemblages are similar to those observed in the zone above with the exception of *Globotruncana lineiana*, *Globotruncana ventricosa*, *Globigerinelloides praerihillensis*, and rare specimens of *Globotruncana lapparenti*.

Only Sample 160-967E-19R-CC was attributed to the *Globotruncanella calcarata* Zone based on the presence of rare specimens of the marker species.

The *G. ventricosa* Zone was identified from Samples 160-967E-20R-CC through 23R-CC. The lowest occurrences of *H. striata*, *Marginotruncana pseudolinneiana*, and *Contusotruncana patelliformis* were observed in this zone.

Samples 160-967E-26R-CC through 29R-2, 87–89 cm, contain the *Dicarinella asymetrica* Zone. This zone includes the highest occurrences of *Heterohelix reussi* and of *Marginotruncana* cf. *sigali* in Sample 160-967E-26R-CC.

Sedimentation Rates

Sedimentation rates for Hole 967A were calculated using 15 calcareous nannofossil and planktonic foraminiferal events (Table 3). The data are plotted on an age vs. depth curve shown in Figure 26. An error line is shown on the figure to indicate the degree of uncertainty as to the location of the nannofossil and foraminiferal events within the hole.

Calculated sedimentation rates vary from 5.3 to 57.5 m/m.y. through the sequence. Eight significant shifts in sedimentation rates were observed. From the seafloor to the first occurrence of *P. lacunosa* (0.46 Ma) the sedimentation rate was approximately 43.5 m/m.y. The sedimentation rate decreased to 28.3 m/m.y. in the interval from the last occurrence of *P. lacunosa* to the first occurrence of *Gephyrocapsa* sp. 3 (0.99 Ma). Between the last and first occurrences of large *Gephyrocapsa* (>5.5 μ m) (1.25 and 1.5 Ma, respectively), sedimentation rates increased to 30.5 m/m.y.

The next observed datum is the last occurrence of *D. brouweri* (1.99 Ma), representing a time interval of 0.5 m.y. The absence of two fossil datums that normally occur within this interval may indicate that the section between the first occurrence of large *Gephyrocapsa* (1.5 Ma) and the last occurrence of *D. brouweri* (1.99 Ma) represents a depositional hiatus. However, these two events are separated by a conspicuous debris-flow unit (see “Lithostratigraphy” section, this chapter) that may have eroded part of the sequence. In the interval between the last occurrence of *D. brouweri* and the last occurrence of *G. puncticulata* (3.57 Ma) the sedimentation rate constantly averaged 30.3 m/m.y.

The sedimentation rate decreased significantly to about 7.2 m/m.y. from the last occurrence of *G. puncticulata* to the last occurrence of *R. pseudoumbilicus* (3.85 Ma). A new increase in the sedimentation rate to 35.6 m/m.y. occurred from the last occurrence of *R. pseudoumbilicus* to the last common occurrence of *G. margaritae* (3.94 Ma). It was followed by a new decrease to the minimum value of 5.3 m/m.y. from the latter event to the first occurrence of *G. puncticulata* (4.52 Ma), which in turn was succeeded by an increase to the maximum val-

Table 2. Position of sapropels recovered at Site 967.

Number	Core, section, interval (cm)	Depth (mbsf)	Thickness (cm)	Number	Core, section, interval (cm)	Depth (mbsf)	Thickness (cm)	Number	Core, section, interval (cm)	Depth (mbsf)	Thickness (cm)
160-967A-				160-967B-				160-967C-			
1	1H-1, 112-133	1.12	21	1	1H-1, 107-127	1.07	20	1	1H-1, 55-75	0.55	20
2	1H-3, 130-138	4.30	8	2	1H-3, 129-138	4.29	9	2	1H-3, 65-75	3.65	10
3	1H-4, 78-83	5.28	5	3	1H-CC, 18-25	5.26	7	3	1H-4, 27-31	4.77	4
4				4				4	1H-4, 47-52	4.97	5
5	1H-5, 145-169	7.50	24	5	2H-1, 110-137	6.40	177	5	1H-5, 74-103	6.74	29
6	1H-CC, 3.5-18	9.09	14.5	6	2H-2, 145-197	8.25	52	6	1H-6, 120-169	8.70	49
7	2H-1, 56-74	10.74	18	7	2H-3, 128-146	9.58	18	7			
8	2H-1, 143.5-180.5	10.95	37	8	2H-4, 65-87	10.45	22	8	2H-1, 36-69	9.86	33
9	2H-2, 81-86	11.61	5	9	2H-4, 121-133	11.01	12	9	2H-1, 117-124	10.6	7
10	2H-4, 84-90	14.64	6	10	2H-6, 110-120	13.90	10	10	2H-3, 102-108	13.5	2
11	3H-1, 33-36	19.13	3	11	3H-3, 43-47	18.23	4	11	2H-6, 98-101	17.9	8
12	3H-1, 128-130	20.08	2	12	3H-3, 137-138	19.17	1	12	2H-CC, 15-50	19.2	7
13	3H-2, 10-24	20.40	14	13	3H-4, 24-30	19.54	6	13	3H-1, 0-4	19.0	0
14	3H-3, 33-38	22.13	5	14	3H-5, 38-45	21.18	7	14	3H-2, 145-150	21.9	5
15	3H-3, 92-97	22.72	5	15	3H-5, 81-93	21.61	12	15	3H-3, 33-50	22.3	3
16	3H-4, 121-124	24.51	3	16	3H-6, 123-126	23.53	3	16	3H-4, 77-78	24.2	7
17	3H-5, 35-40	25.15	5	17	3H-7, 20-42	24.00	22	17	4H-1, 142-150	30.5	0
18	4H-2, 125-127	31.05	2	18	4H-4, 96-102	29.76	6	18	4H-2, 50-72	30.5	0
19	4H-3, 31-52	31.61	21	19	4H-5, 19-22	30.49	3	19	4H-2, 110-113	31.1	0
20	4H-3, 101-109	32.31	8	20	4H-5, 58-62	30.88	4	20	4H-3, 6-9	31.5	6
21	4H-3, 136-146	32.66	10	21	4H-5, 105-114	31.35	9	21	4H-3, 67-74	32.17	7
22	4H-4, 60-67	33.40	7	22	4H-6, 32-38	32.12	6	22	4H-3, 121-123	32.71	2
23				23				23	4H-4, 21-23	33.21	2
24	4H-5, 14-28	34.44	14	24	4H-6, 133-145	33.13	12	24	4H-4, 67-73	33.67	6
25	4H-5, 67-71	34.97	4	25	4H-7, 35-39	33.65	4	25	4H-4, 126-138	34.26	12
26	4H-5, 126-137	35.56	11	26	5H-1, 0-6	33.80	6	26	4H-5, 125-132	35.75	7
27	4H-6, 132-142	37.12	10	27	5H-1, 148-157	35.28	9	27	4H-6, 33-50	36.33	17
28	4H-7, 43-51	37.73	8	28	5H-2, 62-79	35.92	17	28			
29	5H-2, 7-36	39.37	29	29	5H-4, 15-43	38.45	28	29	5H-1, 60-65	38.60	5
30	5H-2, 111-119	40.41	8	30	5H-4, 120-127	39.50	7	30	5H-1, 116-117	39.16	1
31	5H-3, 25-28	41.05	3	31	5H-5, 23-33	40.03	10	31	5H-2, 16-24	39.66	8
32	5H-3, 76-95	41.56	19	32	5H-5, 82-99	40.62	17	32	5H-2, 65-67	40.15	2
33	5H-3, 138-141	42.18	3	33	5H-5, 149-156	41.29	7	33	5H-2, 115-124	40.65	9
34	5H-4, 40-52	42.70	12	34	5H-6, 52-64	41.82	12	34	5H-3, 38-50	41.38	12
35	5H-4, 113-132	43.43	19	35	5H-6, 133-152	42.63	19	35	5H-3, 87-109	41.87	22
36	5H-5, 18-41	43.98	23	36	5H-7, 40-66	43.20	26	36	5H-3, 138-150	42.38	12
37	5H-5, 72-92	44.52	20	37	6H-1, 149-169	44.79	20	37	5H-5, 52-66	44.52	14
38	5H-7, 25-45	47.05	20	38	6H-2, 75-78	45.55	3	38	5H-5, 113-115	45.13	2
39	5H-CC, 26-32	47.70	6	39	6H-2, 115-133	45.95	18	39	5H-6, 0-15	36.00	15
40	6H-1, 31-51	47.61	20	40	6H-3, 22-26	46.52	4	40	5H-6, 47-49	36.47	2
41	6H-1, 91-92	48.21	1	41	6H-3, 67-80	46.97	13	41	5H-6, 87-96	36.87	9
42	6H-1, 131-142	48.61	11	42	6H-4, 47-50	48.27	3	42	5H-7, 45-47	37.95	2
43	6H-2, 101-104	49.81	3	43	6H-4, 97-105	48.77	8	43	5H-CC, 7-22	38.30	15
44	6H-2, 140-146	50.20	6	44	6H-4, 140-161	49.20	21	44	6H-1, 25-37	47.75	12
45	6H-3, 27-42	50.57	15	45	6H-5, 46-59	49.76	13	45	6H-1, 69-72	48.19	3
46	6H-3, 72-83	51.02	11	46	6H-6, 25-44	51.05	19	46	6H-2, 30-44	49.30	14
47	6H-4, 32-44	42.62	12	47	6H-6, 86-104	51.66	18	47	6H-2, 83-92	49.83	9
48	6H-4, 82-84	43.12	2	48	6H-7, 113-115	53.43	2	48	6H-2, 131-150	50.31	19
49	6H-4, 124-140	43.54	16	49	6H-CC, 0-19	53.00	19	49	6H-3, 33-40	50.83	7
50	6H-5, 17-22	53.47	5	50	7H-1, 57-67	53.37	10	50	6H-4, 0-5	52.00	5
51				51	7H-1, 109-114	53.89	5	51	6H-4, 44-49	52.44	5
52	7H-6, 15-26	64.45	11	52	7H-7, 52-64	62.32	12	52	6H-6, 107-120	56.07	13
53	7H-6, 65-76	64.95	11	53				53	6H-7, 0-5	56.50	5
54	7H-6, 129-139	65.59	10	54				54	6H-7, 53-58	57.03	5
55	7H-CC, 21-38	66.45	17	55	8H-1, 97-116	63.27	19	55			
56	8H-1, 12-36	66.42	24	56	8H-2, 11-28	63.91	17	56	7H-1, 21-38	57.21	17
57	8H-1, 84-100	67.14	16	57	8H-2, 72-97	64.52	25	57	7H-1, 76-96	57.76	20
58	8H-2, 115-132	68.95	17	58	8H-2, 133-138	65.13	5	58	7H-1, 79-92	57.79	13
59				59	8H-3, 100-117	66.30	17	59	7H-2, 79-92	59.29	13
60	8H-2, 115-132	68.95	17	60	8H-4, 69-70	67.49	1	60	7H-6, 93-109	65.43	16
61	8H-3, 89-93	70.19	4	61	9H-1, 2-5	71.82	3	61			
62	8H-7, 63-85	75.93	22	62	9H-1, 44-54	72.24	10	62	7H-7, 0-8	66.00	8
63	9H-1, 6-19	75.86	13	63	9H-1, 95-111	72.75	16	63	7H-7, 50-65	66.50	15
64	9H-1, 64-85	76.44	21	64	9H-2, 10-19	73.40	9	64			
65	9H-1, 127-135	77.07	8	65	9H-2, 59-65	73.89	6	65	8H-1, 36-46	66.86	10
66	9H-2, 43-52	77.73	9	66	9H-2, 119-128.5	74.49	9.5	66	8H-1, 100-110	67.50	10
67	9H-2, 112-128	78.42	16	67	9H-4, 75-80	77.05	5	67	8H-3, 33-39	69.83	6
68	9H-4, 93-101	81.23	8	68	9H-5, 7-19.5	77.87	12.5	68	8H-3, 113-127	70.63	14
69	9H-5, 35-49	82.15	14	69	9H-5, 77.5-82	78.58	4.5	69	8H-4, 30-34	71.30	4
70	9H-5, 112-118	82.92	6	70	9H-5, 119-130	78.99	11	70	8H-4, 70-80	71.70	10
71	9H-6, 7-23	83.37	16	71	9H-6, 13-24	79.43	11	71	8H-4, 120-128	72.20	8
72	9H-6, 60-74	83.90	14	72	9H-6, 56-70	79.86	14	72	8H-5, 9-24	72.59	15
73	9H-6, 108-126	84.38	18	73	9H-6, 106-117	80.36	11	73	8H-5, 58-71	73.08	13
74	9H-7, 9-28	84.89	19	74	9H-7, 10-13	80.90	3	74	8H-5, 108-118	73.58	10
75	9H-CC, 8-21	85.50	13	75	9H-7, 53-62	81.33	9	75	8H-6, 0-10	74.00	10
76	10H-1, 7-24	85.37	17	76	9H-CC, 130-135	82.77	5	76	8H-6, 43-57	74.43	14
77	10H-1, 62-79	85.92	17	77				77	8H-6, 82-93	74.82	11
78	10H-1, 112-128	86.42	16	78				78	8H-6, 135-140	75.35	5
79	10H-2, 26-31	87.06	5	79				79	8H-CC, 13-25	76.35	12
80	10H-2, 132-155	88.12	23	80	10H-1, 64.5-77.5	81.95	13	80			

Table 2 (continued).

Number	Core, section, interval (cm)	Depth (mbsf)	Thickness (cm)
160-967D-			
1	1H-1, 110-128	1.10	18
2	1H-3, 126-135	4.26	9
3	1H-4, 92-96	5.42	4
4	1H-4, 114-119	5.64	5
5			
6	2H-1, 139-187	8.09	48
7	2H-2, 134-152	9.54	18
8	2H-3, 67-69	10.37	2
9	2H-3, 147-153	11.17	6
10	2H-5, 131-138	14.01	7

ue of 12.89 m/m.y in the interval between the first occurrence of *G. puncticulata* to the first common occurrence of *G. margaritae* (5.10 Ma).

PALEOMAGNETISM

Paleomagnetic measurements were made on cores from Holes 967A through 967C, following the methods discussed in the "Explanatory Notes" chapter (this volume). The NRM was routinely measured at 10-cm intervals on the archive half of each core section for each hole after AF demagnetization at the appropriate level. Hole 967A was subjected to demagnetization at 20 mT, whereas Holes 967B and 967C were demagnetized at 25 mT. NRM intensities were measurable throughout the recovered sequence and were well above the noise level of the magnetometer after demagnetization at each of the selected AF demagnetization levels (Fig. 27). Many of the intensity peaks shown in Figure 27 coincide with sapropels, as discussed by Roberts et al. (this volume).

Forty-two discrete samples from Hole 967A were subjected to stepwise AF demagnetization to assess the reliability of the whole-core measurements. Most discrete samples were stably magnetized and the paleomagnetic direction can be determined readily from straight lines that are directed to the origin of the vector component diagrams (Fig. 28). The discrete sample data indicate that a strong drill-string overprint is removed at 10 mT and that stable directions are usually reached by 20 mT (Fig. 28). The data from the discrete samples verify much of the whole-core record. However, significant discrepancies exist in parts of the record, particularly between about 48 and 75 mbsf (Fig. 29). Discrete samples from this interval indicate predominantly reverse polarity, whereas the whole-core results are indicative of normal polarity. The discrepancy probably results from normal overprinting that could not be removed from the whole-core record at 20 mT within this interval. The whole-core results in the interval from 56 to 64 mbsf, which contains a debris flow, were removed for the sake of clarity.

The polarity pattern in Hole 967A is obscure in the upper part of the record, but, in conjunction with the biostratigraphic data (see "Biostratigraphy and Sedimentation Rates" section, this chapter), it is possible to delineate a tentative magnetic polarity stratigraphy that needs to be validated by shore-based studies. A transition from normal to reverse polarity is evident between 76 and 78 mbsf based on discrete samples. This interval occurs between the last common occurrence of *Discoaster tamalis* and the last occurrence of *Discoaster pentaradiatus*, which were dated at 2.82 and 2.51 Ma, respectively, in the Mediterranean (Sprovieri, 1993). This polarity transition, therefore, most likely represents the Gauss/Matuyama boundary. Few discrete samples were measured below 90 mbsf because much of the sediment is dominated by a red clay that was not fully demagnetizable by AF methods, presumably because of the presence of significant amounts of hematite. Any interpretation of this interval

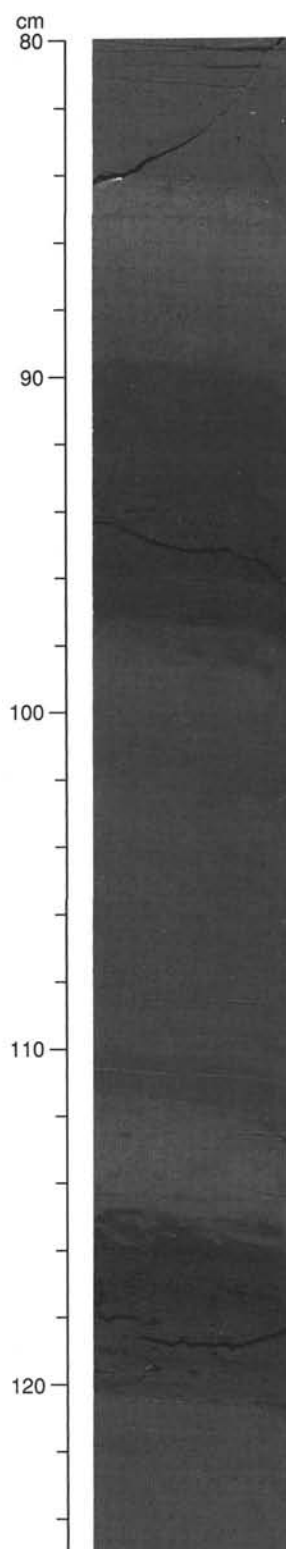


Figure 15. Example of sapropels S3 and S4 from Unit I (Section 160-967D-1H-4, 80-125 cm). The uppermost bed, S3, contains pteropod fragments, is 80 cm thick, and displays a thin, 2-mm-thick, dark clay bed, 1 cm from the base. A prominent pair of 4-cm-thick sapropels at 5.47 and 5.70 mbsf (Hole 967D) corresponds to the sapropel S4 *sensu* McCoy (1974).

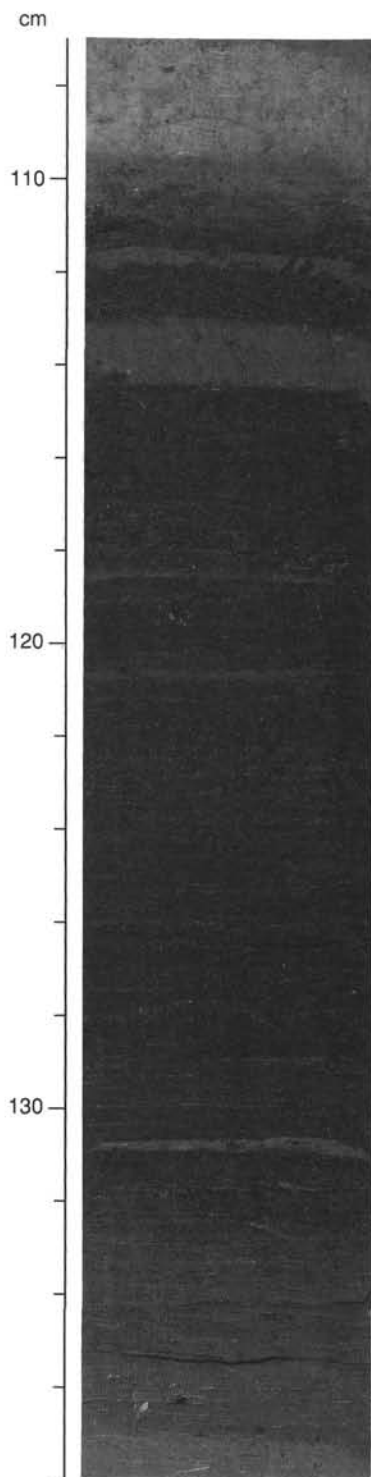


Figure 16. Example of sapropel S5 from Unit I (Section 160-967B-2H-1, 107–138 cm). The S5 bed is 27 cm thick and laminated throughout and contains three 2–15-mm-thick intercalations of dark gray (N4) clay at 111.5–111.7, 113–114.5, and 130.7–130.9 cm.

should be treated with caution because AF demagnetization was the only method used to recover paleomagnetic information. Nevertheless, a transition from reverse to normal polarity at 103 mbsf may represent the Gilbert/Gauss boundary. Furthermore, two zones of

reverse polarity at 87 and 94 mbsf may represent the Kaena and Mammoth Subchrons, respectively. These inferred positions for the Gilbert/Gauss boundary, Mammoth and Kaena Subchrons, and Gauss/Matuyama boundary are consistent with the biostratigraphic data (see “Biostratigraphy and Sedimentation Rates” section, this chapter), as shown on Figure 30. We do not include a polarity zonation on Figure 29 or a table showing the inferred positions of these polarity boundaries because of the highly tentative nature of this interpretation. As is also the case at most other sites studied in Leg 160, the magnetic polarity stratigraphy is highly uncertain in the Brunhes Chron and in most of the Matuyama Chron.

Superficial similarity among the whole-core results from Holes 967A, 967B, and 967C (Fig. 31) suggests that it should be possible to obtain a useful composite magnetostratigraphy from Site 967 after detailed post-cruise investigation.

STRUCTURAL GEOLOGY

The six holes drilled at Site 967 can be divided into five lithostratigraphic units in terms of lithostratigraphy, age, FMS, and seismic data (see “Lithostratigraphy,” “Biostratigraphy and Sedimentation Rates,” “Downhole Measurements,” and “Site Geophysics” sections, respectively, this chapter):

- Unit I: nannofossil ooze with interlayered organic-rich layers (middle Pliocene–Pleistocene);
- Unit II: “transition zone” (sequence containing a mixture of chaotically deposited nannofossil clays with lithoclasts) with a basal evaporite sequence (Miocene(?), lower Pliocene);
- Unit III: pelagic calcilutites and foraminifer-bearing nannofossil chalks (Eocene–Upper Cretaceous) interlayered with cherts;
- Unit IV: shallow-water calcarenites interbedded with cherts; and
- Unit V: brecciated and deformed calcarenites.

The sediments of the different units obtained contain various deformation structures (Fig. 32). Unit I is a predominantly horizontally bedded sequence with rare tilted beds. The inclined bedding planes are thought to be related to intervals of current deposition and microfaulting. Unit II is a transition zone between Unit I and the lithified carbonate deposits of Unit III below. Both deformational and sedimentary structures are rare in these lithoclast-bearing muds. Unit III consists of nannofossil chalks with a varying amount of clay and foraminifers. Microfaulting (dominantly normal) and intense fracturing of the well-lithified material were observed. Below 475 mbsf, less intense deformation of shallow-water carbonates is indicated by rare fractures and microveins. Unit V is characterized by an increasing intensity of diagenetic alteration and deformation of the calcarenites. Carbonate clasts are cut by microfractures and veins and are intensely brecciated in places. Evidence for shear along particular planes and pressure solution was found in the basal part of Hole 967E.

Owing to poor recovery deeper in the hole (Units III–V), the abundance of structural features decreases strongly (Fig. 32A). Low recovery is simplistically compensated for the limestones of Units IV and V by plotting the abundance of faults per meter (Fig. 32B).

Data

Measurement of structures in three dimensions in Units I and II was permitted only in Holes 967A and 967C because of the necessity of preserving intact sapropel sequences for post-cruise sampling. The Tensor orientation tool was run in Holes 967A through 967C, and results of the measurements on cores from Holes 967A and 967C were reoriented to their original geographic orientation (Fig. 33).

Units III, IV, and V were recovered primarily by RCB drilling. Although structures were measured with respect to the core liner

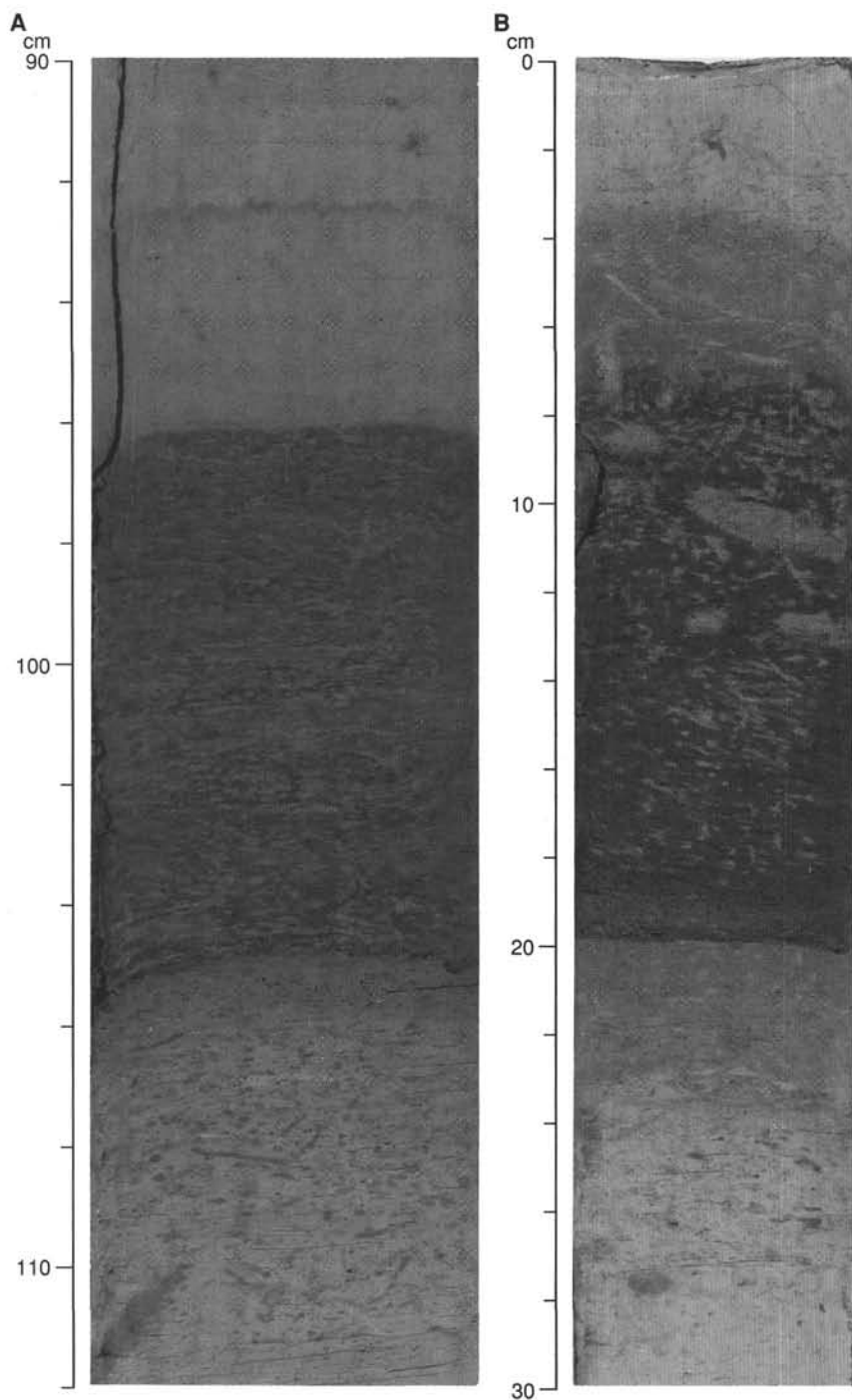


Figure 17. Examples of the sapropels within the lower part of the Unit I sequence (upper Pliocene to lower Pleistocene: **A**, Section 160-967B-6H-4, 90–112 cm; **B**, Section 160-967B-9H-5, 0–30 cm). These beds are typically between 5 and 20 cm thick and are variably bioturbated, generally by *Chondrites*. In some cases, only the uppermost part of the bed is affected.

throughout these intervals, rotation of lithified sediment relative to the core liner could not be determined. As a result it is not possible to reorient the measurements to geographic orientation.

A list of the structural measurements collected at this site is given in Table 4.

Description of the Deformational Features

Units I and II

Unit I contains a dominantly horizontally bedded sequence of nannofossil ooze and clay interlayered with debris-flow deposits (Fig. 34). Graded layers, tilted sedimentary beds, slightly irregular to

chaotic sedimentary deposits (e.g., Sections 160-967A-7H-2 and 3, 160-967B-7H-1 through 6, and 160-967C-6H-4 and 5) indicate mass movement and current deposition. Rarely, sediment sliding and slumping have caused minor folding (Fig. 35).

The majority of the faults in Unit I are high-angle planar microfaults with normal offsets in the order of 0.2–6 cm. Although most of the fault geometries observed in this sequence are single high-angle faults, microfaults with more diffuse zones of deformation and moderate to high dip angles were also found (e.g., Sections 160-967A-7H-2 through 5 and 160-967B-7H-2 and 3; for an example, see Fig. 36). Within these zones, anastomosing fractures and microveins (with millimeter offsets and some different colored fills) join fault

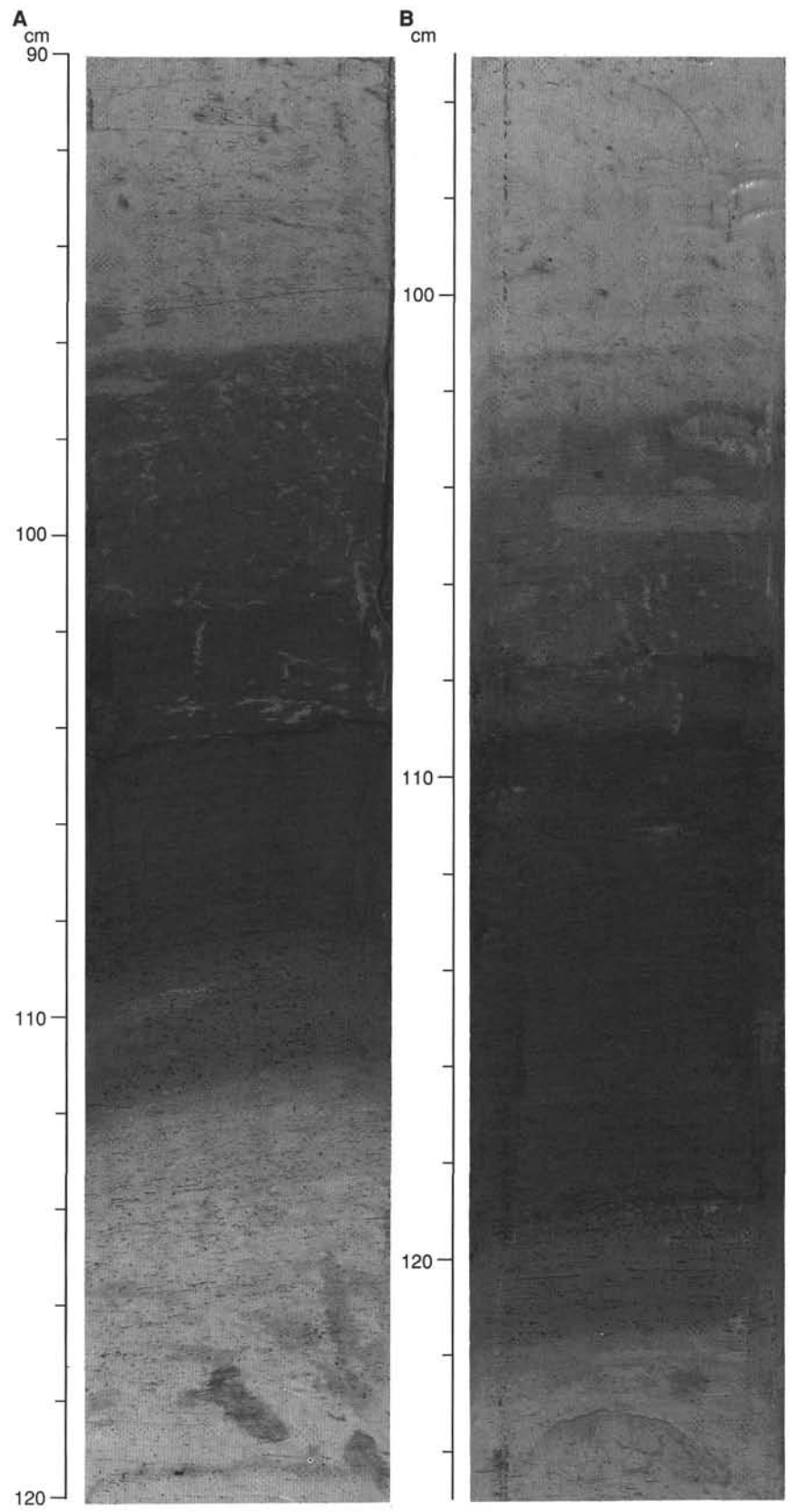


Figure 18. Examples of an entire sapropel from Unit I that was pervasively burrowed. **A.** Section 160-967B-8H-1, 90–120 cm. **B.** Section 160-967B-8H-3, 95–125 cm.

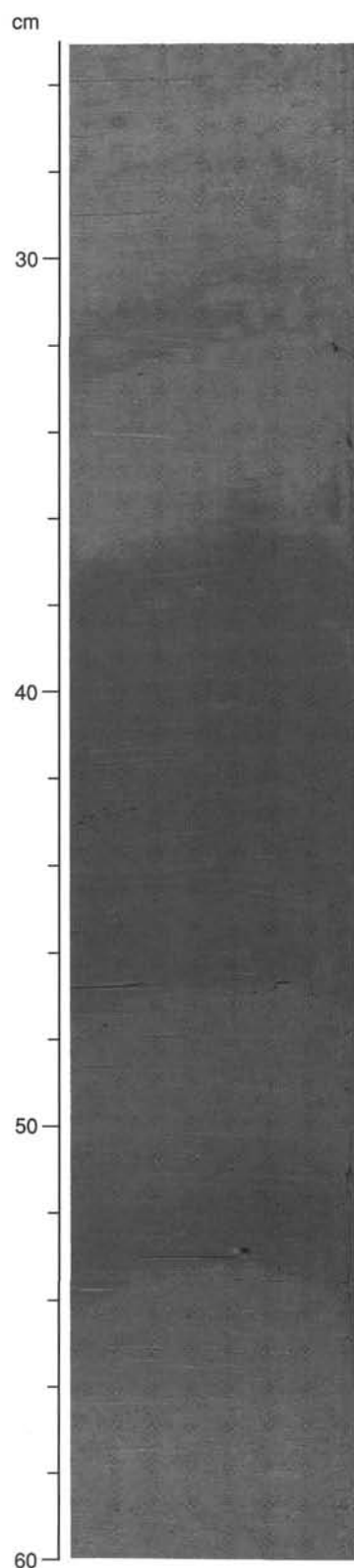


Figure 19. Color grading from gray (5Y 5/1) nannofossil clay to grayish brown (10YR 5/2) and/or pale brown (10YR 6/3) nannofossil ooze at Section 160-967A-1H-4, 25–60 cm.

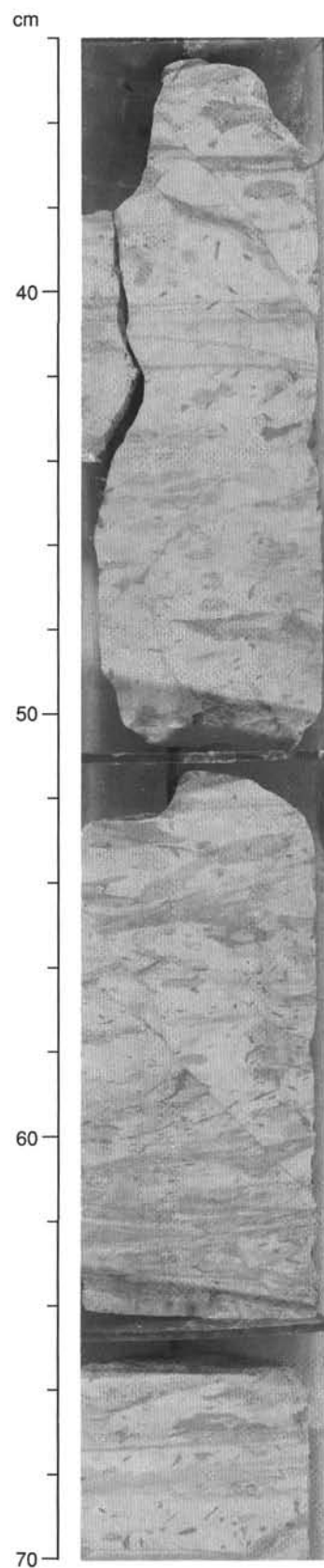


Figure 20. Example of *Planolites*- and *Chondrites*-mottled well-lithified foraminifer nannofossil chalk (Section 160-967E-9R-1, 34–70 cm).

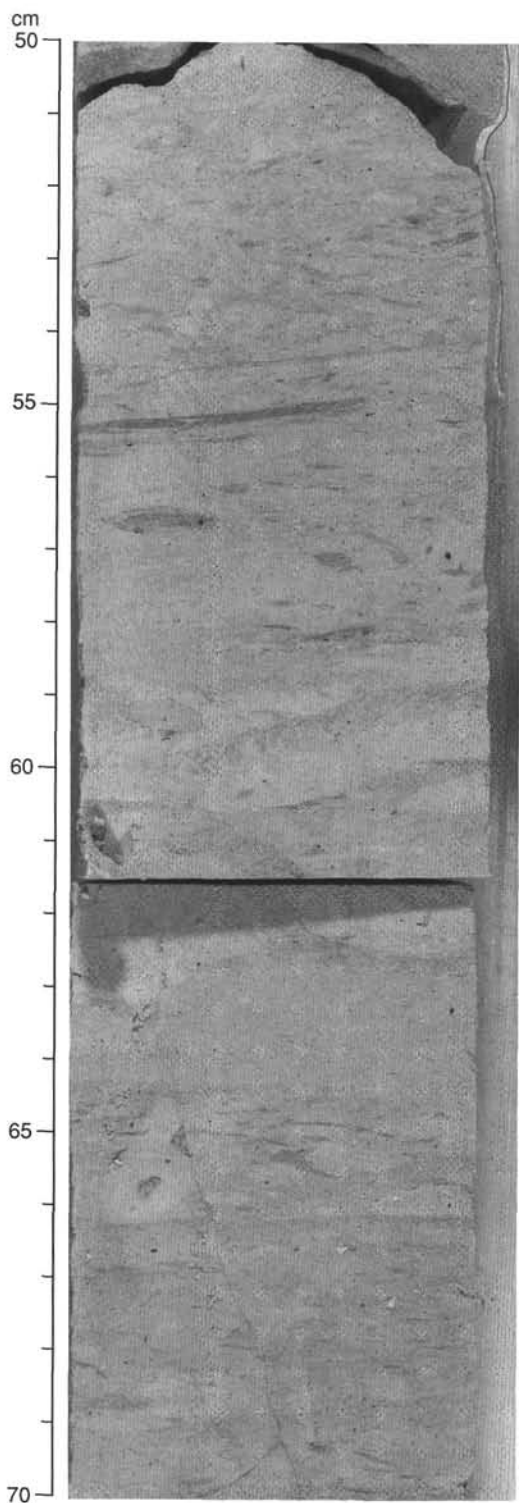


Figure 21. Example of *Zoophycos*-mottled and well-lithified foraminifer nannofossil chalk (Section 160-967E-17R-1, 50–70 cm).

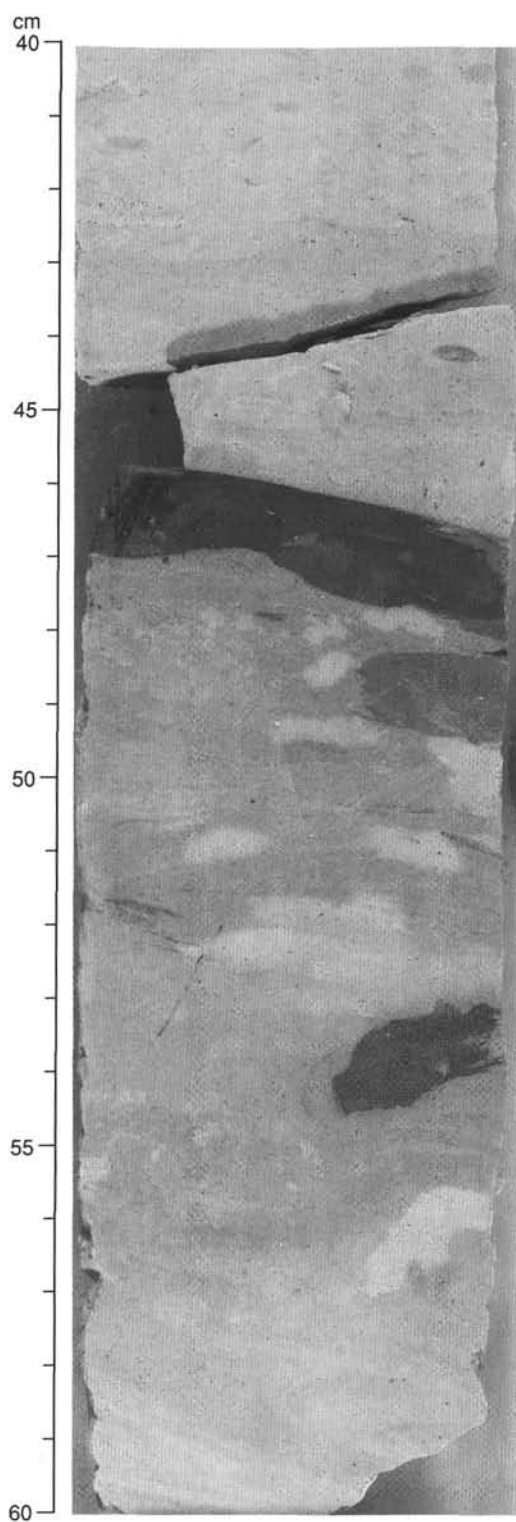


Figure 22. Example of black chert nodules within the foraminifer nannofossil chalk (Section 160-967E-6R-3, 40–60 cm).

surfaces. In some cases, small reverse faults with distinct offsets of a few millimeters occur both as single features and as sets of “en echelon” faults (cf., Table 4).

The angles of the fault planes for which it was possible to calculate a true dip with respect to the core liner (Holes 967A, 967C, and 967E) scatter almost randomly between 0° and 90° (Fig. 37). These observations suggest that a sample bias in terms of the orientation of

fault traces visible on the core face and 0°-dip plane (which may be related to the drilling process; cf., “Structural Geology” section, “Site 964” chapter, this volume) can be excluded (Table 4). For some of the microfaults it was not possible to match offset intervals on either side of the faults. In these instances, the sense of movement could not be determined, but the displacement was inferred to have been greater

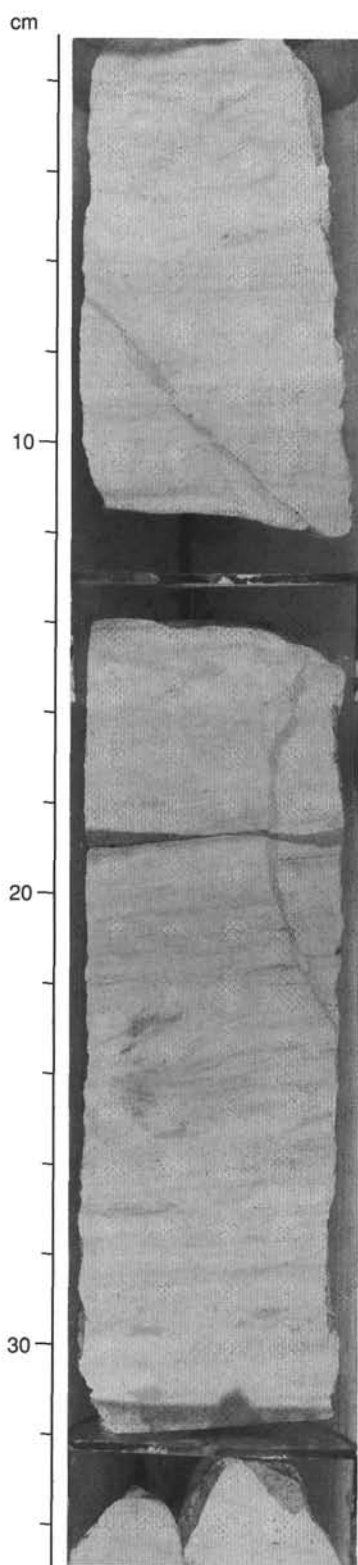


Figure 23. Example of sporadic fractures within the foraminifer nannofossil chalk (Section 160-967E-6R-3, 1–35 cm).

than the length of the fault exposed in the core face. Moderate- to high-angle planar discontinuities (named “microveins” following the usage of Lindsley-Griffin et al., 1990; Behrmann, Lewis, Musgrave, et al., 1992; Westbrook, Carson, Musgrave, et al., 1994), marked either by the trace of a dark mineral (possibly sulfide) or material enriched in organic matter along their length, were also observed.

The transition from Unit I to Unit II occurs between 108 mbsf (Hole 967C) and 119 mbsf (Hole 967E). It is marked by a fairly abrupt change from horizontally to subhorizontally bedded, faulted nannofossil ooze and clay to mud conglomerates and fine-grained, homogeneous, structureless muds with limestone lithoclasts in which little evidence of bedding is observed (e.g., Sections 160-967A-13H-4 through 16X-CC, 160-967B-13H-5 through 14H-2, 160-967C-13H-1 through 13H-CC, and 160-967E-2R-1). The matrix-supported texture is thought to represent primary depositional fabrics (probably as debris flows with significant amounts of carbonate lithoclasts toward the base of the transition zone).

Within Unit II, homogeneous calcareous muds split along partings perpendicular to cut faces, but contain no deformational structures. A higher quantity of clay (Fig. 11, see “Lithostratigraphy” section, this chapter) and an increase in consolidation may be responsible for the observed fabrics. The base of the transition zone is defined by an evaporite interval (at 120–125 mbsf in Hole 967E) identified by characteristic changes in FMS signatures and anomalies in SO_4^{2-} and chlorinity profiles with depth (see “Downhole Measurements” and “Inorganic Geochemistry” sections, this chapter).

Unit III

Pelagic carbonate represented mainly by calcilutites and nannofossil chalk, showing pervasive burrowing and a distinct subhorizontal to slightly dipping ($<20^\circ$) fabric, are the dominant lithologies of Unit III. Graded beds on a centimeter to decimeter scale are related to current deposition in a marine shelf environment. Furthermore, rare debris-flow deposits were found. A significant increase in the intensity of deformation (up to 30 measurements per core where recovery did not exceed 40%–50%; e.g., Core 160-967E-14H) occurs within this unit (Fig. 32B).

Both single microfaults and sets of dominantly normal faults crosscut the fabric with moderate to steep angles (Fig. 38). Determinable offsets, ranging from 0.1 to 1.2 cm, suggest only minor tectonic movement along these planes. However, open fractures with altered/weathered and polished surfaces commonly have slickensides that indicate downdip transport. The amount of displacement along these fractures could not be estimated, but most likely exceeds the measured offsets (cf., Table 4). Over certain intervals, more intense deformation is reflected by conjugate faulting, fracturing, and folding on a centimeter scale (Fig. 39). Crosscutting steep conjugate normal faults with a different orientation indicate failure in an almost rectangular orientation relative to each other. In one case, an open fissure with boundaries defined by penetrative fractures and microfaults contains a less deformed sediment infill of unbroken foraminifer tests (“Neptunian dike” system; Fig. 40, and VCD forms on the CD-ROM, back pocket). Burrows inside the fissure are less flattened than those outside and above it, which suggests that the infill was in some way protected from compaction. However, microfaults, sediments, and infill are all cut by burrows, suggesting that both fissure formation on the seafloor and infill occurred prior to complete lithification of any of the sediments involved.

The traces of microfaults and fractures are commonly joined by anastomosing microfractures and veins, filled with both calcite cement, sulfide, and organic-rich matrix material. Some sets of normal microfaults could be related to debris-flow deposition (see below, and Fig. 40).

Optical microscope studies on thin sections added information on textures and deformational fabrics. A well-developed, subhorizontal

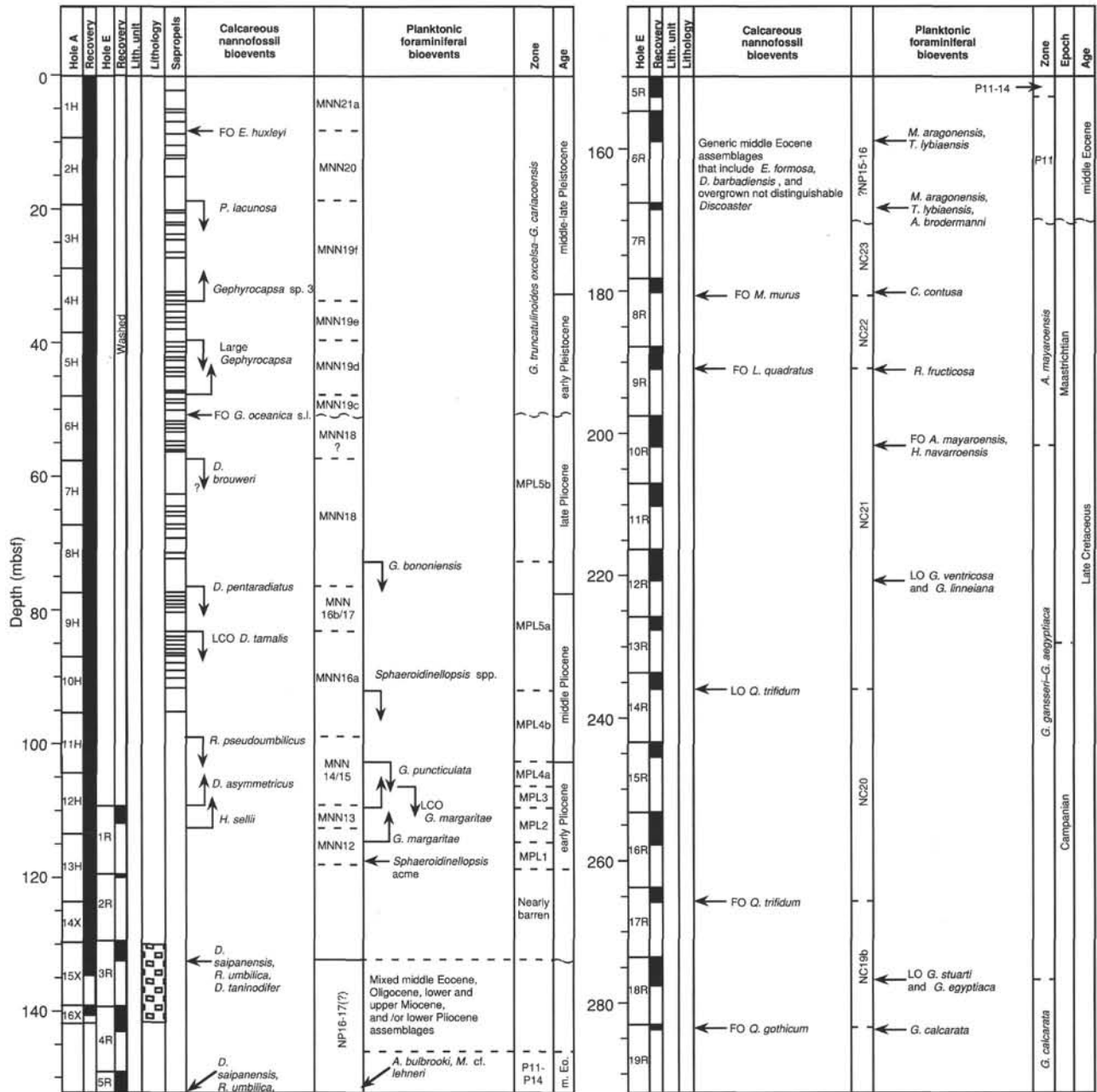


Figure 24. Composite of biostratigraphic events recognized at Holes 967A and 967E including the lithostratigraphic record.

to slightly dipping fabric was observed in the nannofossil chalk. Deformation is also indicated by fragmentation and dissolution of foraminifer tests and alignment along the fabric. Two types of microveins could be distinguished within this unit, but these may be related to the same deformational process. In most cases, subhorizontal, darkened cracks are filled with organic-rich matrix. Both foraminifers and organic matter are slightly enriched along small microveins, with a preferred orientation outside obvious burrow structures. These features intersect the whole specimen (>5 cm) and are spaced at least 100 µm apart (e.g., Section 160-967E-30R-1, 30–34 cm). In addition, some of the chalk contains very poorly developed veins that are only 4–10 µm wide, a few millimeters in length, and healed with calcite (e.g., Section 160-967E-35R-1, 13–15 cm). Sets of closely spaced small normal microfaults (width of trace, <15 µm; length, 150 µm), with

offsets in the order of 1 mm (e.g., Section 160-967E-19R-1, 0–5 cm), penetrate both the initial fabric and replacement chert layers and clasts (up to 2 cm in length and with offsets of about 4 mm; e.g., Section 160-967E-19R-1, 0–6 cm).

Several intervals contain detrital calcite grains that are deformed (some are broken) and contain stress twins (e.g., Section 160-967E-26R-1, 4–7 cm). These grains reach up to 3 mm in diameter, are mostly rhombohedral, and show a preferred orientation of their long axis/edges along the main fabric.

Unit IV

The top of Unit IV occurs at about 434 mbsf in Hole 967E. It is defined by a lithologic change from deep-water carbonates (mainly

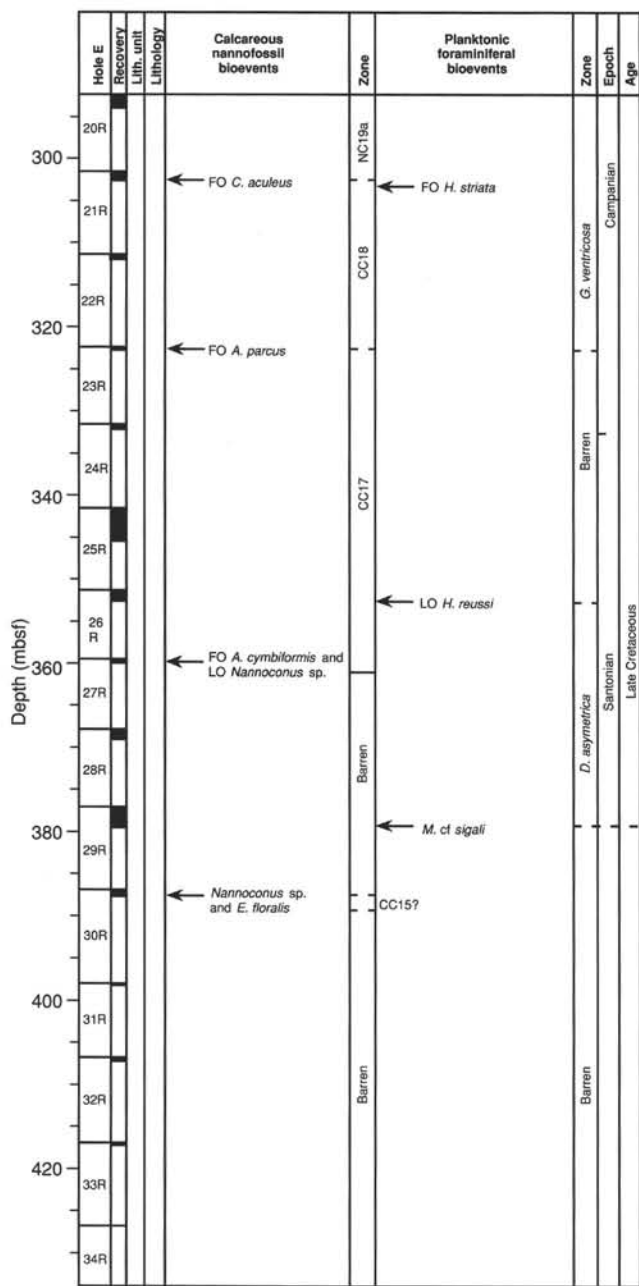


Figure 24 (continued).

nannofossil chalk of middle Eocene age) to shallow-water calcarenites of Late Cretaceous age (see "Lithostratigraphy" section, this chapter) and by a marked change in the character of the mechanical caliper device (MCD) and FMS signatures (see "Downhole Measurements" section, this chapter). The structural features of the rocks recovered also change markedly over this boundary, becoming increasingly fractured. The low recovery of this interval may lead to the overestimation of the amount of deformation, although it is possible that the low recovery itself results from drilling of faulted material. Another possible cause, however, may be the presence of chert, of which fragments were recovered.

Observations on Cores 160-967E-36R through 48R revealed rare microveins cutting the calcarenites. Within the calcarenite succession, a single pebble of laminated green chalk was found with a strong deformational fabric (Section 160-967E-36R-1, 5–8 cm).

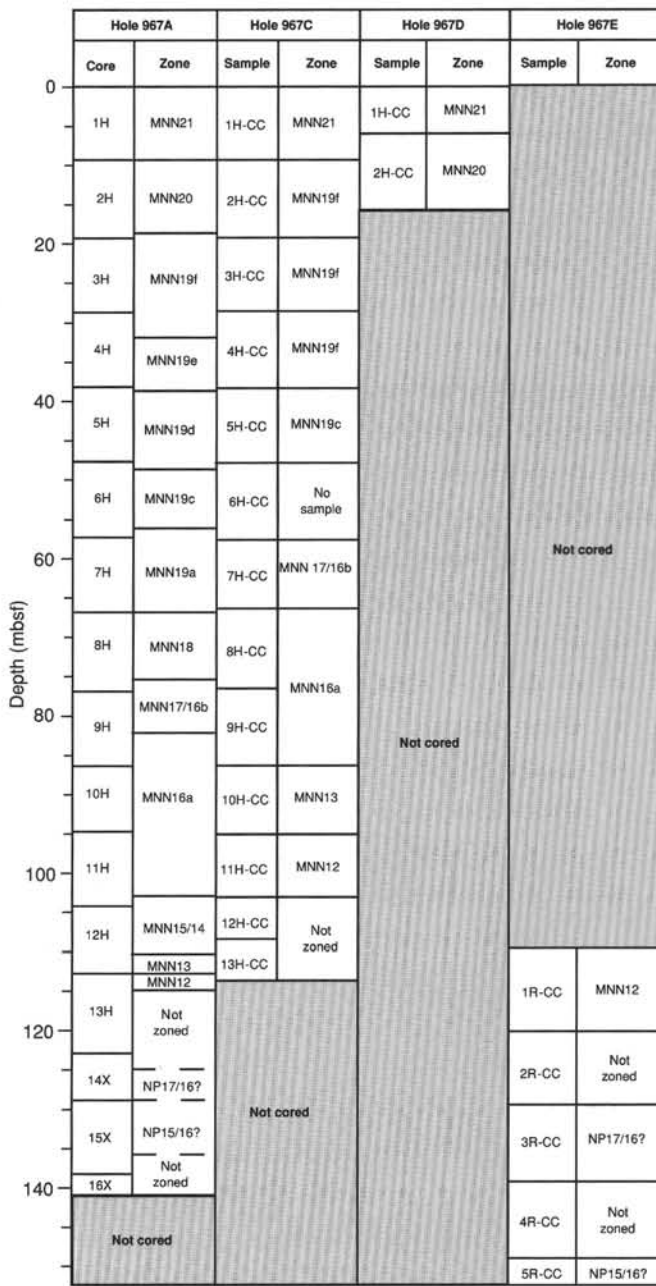


Figure 25. Composite of calcareous nannofossil zones recognized from samples collected from within each section of core in Hole 967A and core-catcher samples recovered from Holes 967C, 967D, and 967E.

Green, millimeter-thick laminae flow around small nodules of light brownish micrite, with small recrystallized calcite shadows. A single, steep normal microfault 10 mm in length crosscuts and offsets the banding by 1 mm.

Optical microscope observations of thin sections revealed that the homogeneous, fine-grained calcareous matrix of the calcarenites is enriched in organic matter along particular planes. The brownish matrix is crosscut by small microveins that are generally filled with organic-rich micrite, calcite, or chalcidony. Small microfractures (mostly about 40–100 μm wide) contain both calcitic or chalcidonic cements along their walls (e.g., Sections 160-967E-41R-1, 12–16 cm, and 160-967E-44R-1, 1–6 cm). Cements range from <5 to 40 μm in grain size and suggest dissolution, mobilization, and recrystalliza-

Table 3. Stratigraphic list of calcareous nannofossil and planktonic foraminifer events for Site 967.

Event	Core, section, interval (cm)	Depth (mbsf)	Depth (mcd)	Age (Ma)
FO <i>E. huxleyi</i> *	160-967A-1H-7, 53	9.03	9.03	0.26
LO <i>P. lacunosa</i>	2H-CC	19.11	19.49	0.46
FO <i>Gephyrocapsa</i> sp. 3	4H-3, 132	32.62	34.5	0.99
LO <i>Gephyrocapsa</i> >5.5 μ m	5H-1, 135	39.15	41.91	1.25
FO <i>Gephyrocapsa</i> >5.5 μ m	5H-7, 45	47.25	50.01	1.5
FO <i>G. oceanica</i> s.l. [†]	6H-2, 120	50	53.56	1.75
LO <i>D. brouweri</i>	6H-7, 24	57.54	61.1	1.99
LO <i>G. bononiensis</i>	8H-5, 55-57	72.86	77.68	2.45
LO <i>D. pentaradiatus</i>	8H-6, 120	75	79.82	2.51
LCO <i>D. tamalis</i>	9H-4, 130	81.6	86.04	2.82
LO <i>Sphaeroidinellopsis</i> spp.	10H-4, 69-71	90.5	94.14	3.22
LO <i>G. puncticulata</i>	11H-5, 128-130	102.09	107.19	3.57
LO <i>R. pseudoumbilicus</i>	11H-7, 30	104.1	109.2	3.85
LCO <i>G. margaritae</i>	12H-2, 61-63	106.42	112.4	3.94
FCO <i>D. asymmetricus</i> [†]	12H-6, 30	109.11	115.09	4.11
FO <i>G. puncticulata</i>	12H-6, 71-73	109.52	115.5	4.52
FCO <i>G. margaritae</i>	13H-1, 77-79	114.58	122.98	5.10

Notes: FO = first occurrence; LO = last occurrence; FCO = first common occurrence; LCO = last common occurrence; * = to be confirmed by scanning electron microscopy; † = not used in sedimentation-rate calculation.

tion of carbonate and silica. Most of the pore space is filled by recrystallized calcite and chalcedony.

Unit V

At 504 mbsf, the first appearance of brecciated calcarenites was found (Section 160-967E-44R-1, 0-8 cm) and this characterizes the top of Unit V (Fig. 41). The angular to subangular (<1 mm to 2.5 cm in diameter) clasts of calcarenite are cemented with calcite (Fig. 42). An enrichment of organic matter along the partly polished contacts is suggested by the dark brownish colors and from thin-section observations. Along the shear planes, slickensides indicate approximately downdip movement. The presence of stylolites indicates that pressure solution occurred within the calcitic clasts.

Calcite precipitation occurred in low-strain areas between broken, sheared clasts. Anastomosing microveins within the angular clasts are filled with both calcite and organic material and show no systematic orientation relative to the core coordinates. Rare foraminifer tests are usually broken.

Interpretation

For Units I and II, the association of faults with the transition from a sequence of undisturbed horizontal bedding to one in which debris-flow deposits and tilted beds occur suggests that processes related to the initiation of downslope movement also resulted in faulting. Isolated limestone clasts in fine-grained nannofossil ooze may also be a product of faulting supplying coarse blocks of older limestone to deeper water environments. However, given their basal position in Unit II, these clasts could also have been generated by erosion prior to debris-flow deposition.

The high-angle faults found in this interval may have been caused by differential compaction after debris-flow and slump deposition. The more brittle behavior of the sediment in the lower part of Unit II may be related to an increase in clay mineral content (see "Lithostratigraphy" section, this chapter) causing increased consolidation and cohesion.

Within the well-lithified micritic chalk, small-scale offsets along variably dipping faults probably reflect syn- to early postsedimentary faulting (e.g., a set of normal faults above the debris-flow deposits, Fig. 39) that may be related to slumping and differential movement of semilithified sediments. The pervasive steep faults with slickensides probably reflect a later tectonic event. The chemically altered

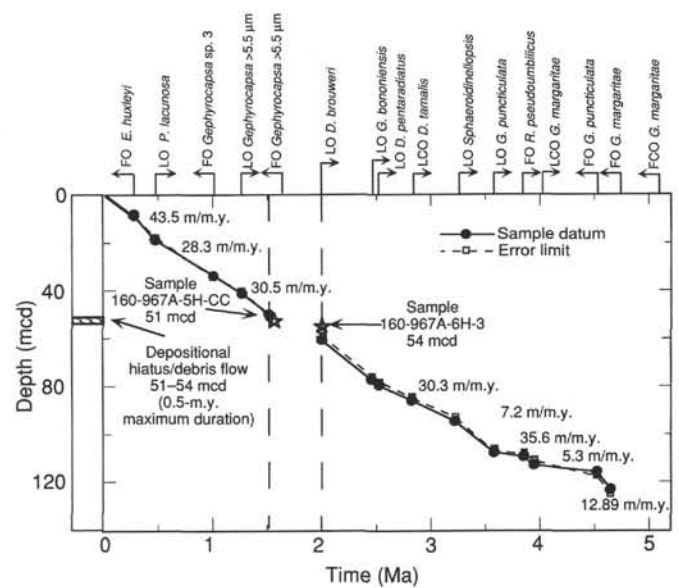


Figure 26. Age vs. depth diagram showing selected calcareous nannofossil and planktonic foraminifer datums with corresponding sedimentation rates. The line corresponds to the sample where the marker species was found for the corresponding first or last occurrence datum; the dashed line corresponds to the nearest sample where the marker species was not found.

surfaces of these faults and fractures indicate that they have been used as fluid conduits. One possible explanation for the changes in heat flow across the Unit III/Unit II boundary (see "Physical Properties" section, this chapter) is that these fractures transported fluid up through Unit III, but that the clay-rich material at the base of Unit II acted as a seal, preventing flow up into the upper part of the succession.

Bearing in mind the poor recovery, the observed fracturing of the calcarenites in Unit IV appears to increase toward the base of the sequence (Fig. 32). The brecciated pebbles found in Unit V were generated by faulting, an interpretation that is supported by the abundance of slickenside surfaces both crosscutting and between clasts. Thus, although the extent of faulting is impossible to estimate given the lack of material, it is possible that the downhole increase in fracturing in Unit IV relates to the proximity of an intensely faulted zone in Unit V.

COMPOSITE DEPTHS

High-resolution (2-10-cm scale) data collected on whole cores on the MST and percent color reflectance collected on split cores from Holes 967A through 967D and Hole 967F were used to determine depth offsets in the composite section. On the composite depth scale, sedimentary features present in adjacent holes were aligned so that they occur at approximately the same depth. Working from the top of the sedimentary sequence, a constant was added to the depth in meters below seafloor for each core in each hole to arrive at a composite depth for that core. The depth offsets that make up the composite depth section are given in Table 5. Continuity of the sedimentary sequence was documented for the intervals between 0 and 61 mcd and between 70 and 130 mcd. A composite record was not constructed for the section below 130 mcd as no MST data were collected on the RCB cores from Hole 967E.

Percent color reflectance (collected at 2-cm intervals) and magnetic susceptibility data (collected at 3-cm intervals) were the primary parameters used for correlation purposes at this site. Natural

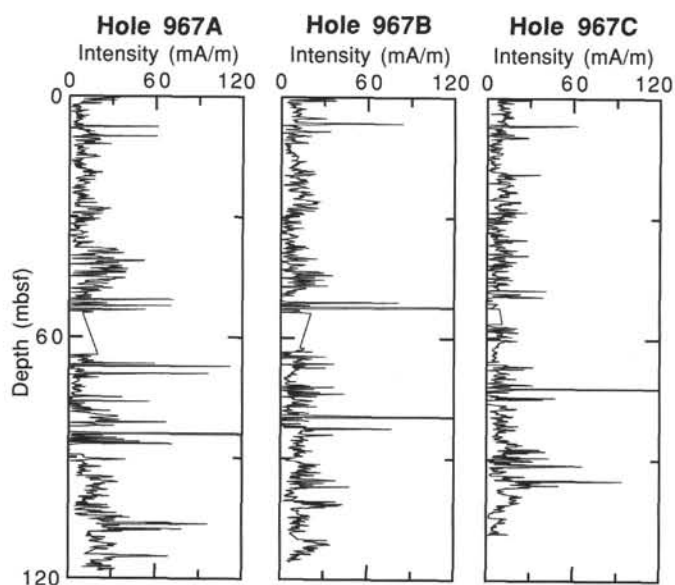


Figure 27. NRM intensity after AF demagnetization at 20 mT for Hole 967A and at 25 mT for Holes 967B and 967C.

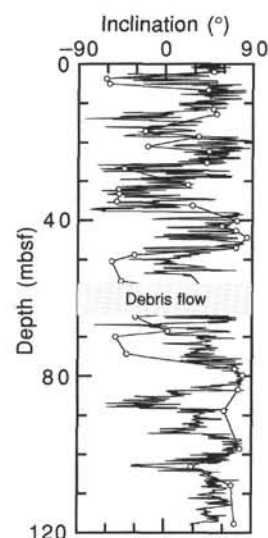


Figure 29. Whole-core paleomagnetic inclination data for Hole 967A (measured at 20 mT) compared with inclinations from stepwise demagnetized discrete samples. Inclinations for discrete samples were determined by linear regression fits to multiple demagnetization points in each case. See text for discussion of the results. Data are not shown in the interval from 56 to 64 mbsf because of the presence of a debris-flow unit.

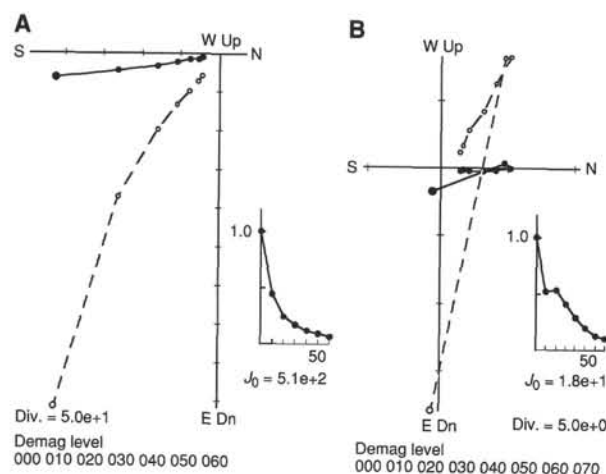


Figure 28. Representative vector component demagnetization diagrams for discrete samples that were subjected to stepwise AF demagnetization. **A.** Typical normal polarity (Sample 160-967A-1H-2, 48 cm; 1.98 mbsf); **B.** Typical reverse polarity (Sample 160-967A-1H-3, 70 cm; 12.94 mbsf). Open (solid) symbols represent projections onto the vertical (horizontal) plane. Demagnetization steps (in mT) are shown below each diagram.

gamma-ray data (collected at 10-cm intervals) and GRAPE wet-bulk density data (collected at 2-cm intervals) provided supplementary verification of core overlap and depth offsets.

The percent color reflectance records (550-nm wavelength) and magnetic susceptibility data used to verify core overlap for Site 967 are shown on a composite depth scale in Figures 43 and 44, respectively. The cores from Holes 967A, 967B, 967C, 967D, and 967F provide continuous overlap to approximately 61 mcd (base of Core 160-967A-6H). Continuity of the section was confirmed primarily with data from the first three holes (Holes 967A, 967B, and 967C), as Holes 967D and 967F consist of two and one mud-line cores, respectively. Between 57 and 66 mbsf (61–70 mcd), the section consists of a slumped unit (see “Lithostratigraphy” section, this chapter). Inter-hole comparison of MST and color reflectance data could not verify

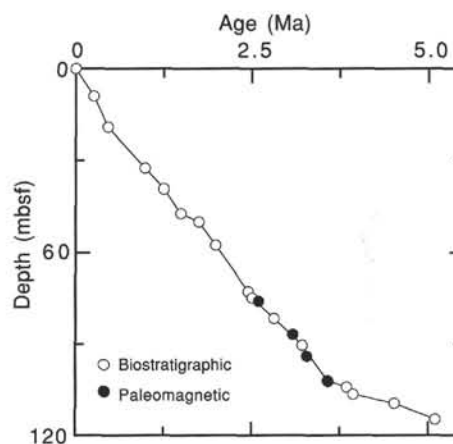


Figure 30. Age vs. depth plot for preliminary magnetostratigraphic data compared with the positions of biostratigraphic datums (see “Biostratigraphy and Sedimentation Rates” section, this chapter). The datums shown (from higher to lower in the sequence) are the interpreted positions of the Gauss/Matuyama boundary, middle Kaena Subchron, middle Mammoth Subchron, and Gilbert/Gauss boundary.

complete overlap in this interval but could not discount it either, as no apparent gap exists in the data. Between 66 and 123 mbsf (70–130 mcd) data from cores from Holes 967A, 967B, and 967C confirm continuous overlap. The continuity of the section could not be confirmed for the sequence below 130 mcd. Although MST data were collected on XCB cores in this interval (Cores 160-967A-14X through 16X), similar data were not collected on the RCB cores from Hole 967E recovered across this interval.

Significant stratigraphic gaps (greater than 2 m) occur only in Hole 967C. Most between-core gaps in Holes 967A, 967B, 967D, and 967E are less than 1 m, with many less than 50 cm. A 7-m gap occurs between Cores 160-967C-6H and 7H (64–71 mcd). The equivalent depth interval in Holes 967A and 967B consists of a

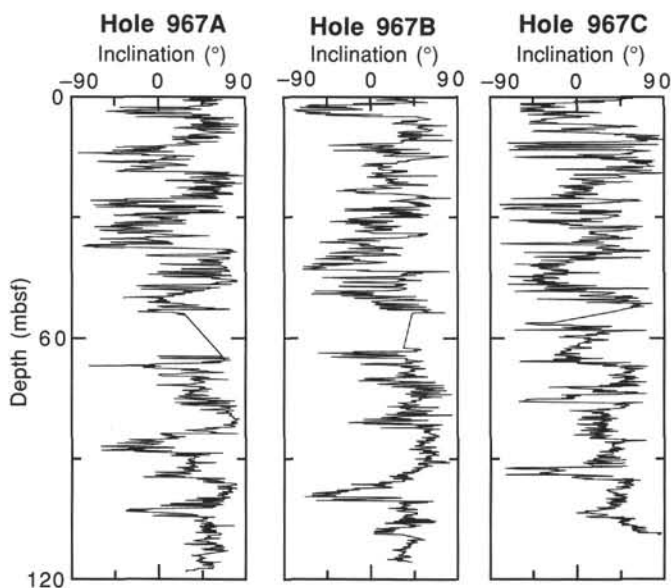


Figure 31. Paleomagnetic inclinations measured on archive-half cores using the shipboard pass-through magnetometer for Hole 967A (after AF demagnetization at 20 mT). Data from Holes 967B and 967C were subjected to AF demagnetization at 25 mT.

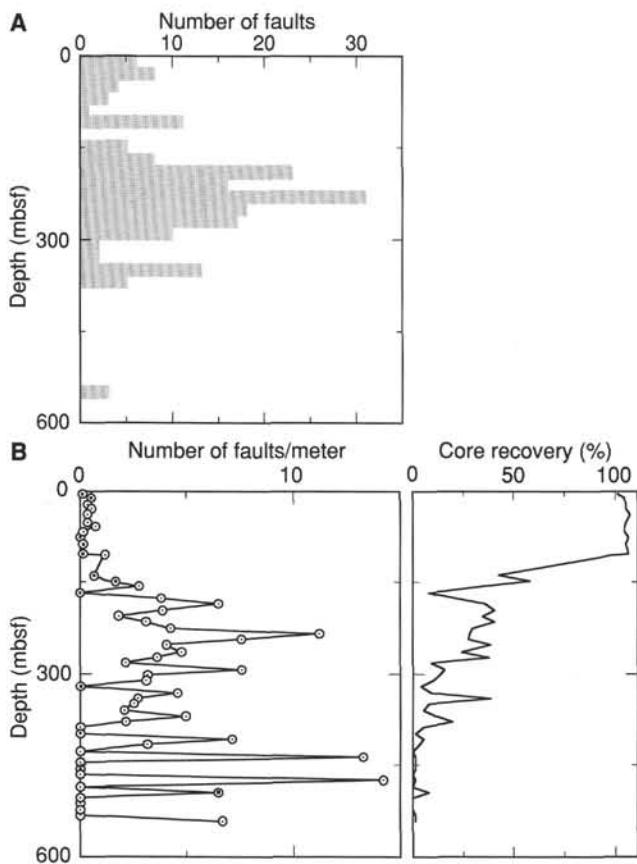


Figure 32. Composite frequency plots of structural features (microfaults, fractures, and veins) with depth in Holes 967A through 967C for Units I and II and Hole 967E for Units III, IV, and V. **A.** Total number of structural features vs. depth. **B.** Number of faults per meter (low recovery is simplistically compensated for) and percentage recovery.

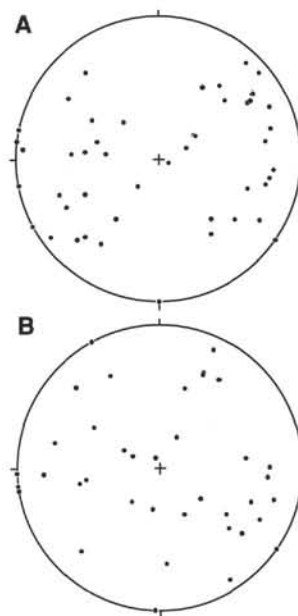


Figure 33. **A.** Lower hemisphere equal-area projection of poles to faults from Holes 967A and 967C with respect to core coordinates. **B.** Lower hemisphere equal-area projection of poles to faults from Holes 967A and 967C corrected to geographic coordinates using Tensor tool data.

slumped unit (see “Lithostratigraphy” section, this chapter), which suggests that this interval was removed from the section in Hole 967C. The “gap” is therefore an artifact of the composite construction procedure and not a true coring gap.

Stretching and compression of the sedimentary features in aligned cores indicates distortion of the cored sequence and, possibly, variations in the sedimentation rate among the holes. Distortion of the sequence was particularly severe at this site as compared to Sites 963 through 966. Because much of the distortion occurs within individual cores on depth scales of less than 9 m, it was not possible to align many features in the color reflection and magnetic susceptibility records accurately by simply adding a constant to the mbsf core depth. Examples of within-core distortion can be seen in Figures 43 and 44 (e.g., compare Cores 160-967A-6H and 160-967B-7H; Cores 160-967A-9H and 160-967B-9H). The apparent overlap of Cores 160-967A-9H and 10H results from aligning stretched/compressed sections between two or more holes (Fig. 43). In this case, sapropels at the top of Core 160-967A-10H were aligned with equivalent sapropels from the base of Core 160-967C-8H. This alignment results in what appears to be a 2-m overlap between Cores 160-967A-9H and 10H. However, the base of Core 160-967A-9H is stretched compared to equivalent sections in Holes 967B and 967C. Simple within-core linear squeezing of the section would remove this apparent overlap. Within-core depth-scale changes, as in this example, will require post-cruise processing to align many sedimentary features.

Following construction of the composite depth section for Site 967, a single spliced record was assembled from the aligned cores. The Site 967 spliced record can be used as a sampling guide to recover a single sedimentary sequence. The spliced record consists primarily of cores from Holes 967A, 967B, and 967C. Intervals with significant disturbance or distortion were avoided where possible. The tie points for the splice are given in Table 6. As within-core distortion was considerable at this site, a small (20 cm) depth discrepancy may result when comparing composite depths generated from the offset depth table (Table 5) with composite depths of a single down-core record (e.g., percent color reflectance) generated using the splice

Table 4. Structural data collected at Site 967.

Core, section, interval (cm)	Depth (mbsf)	Feature	Offset width (cm)		Orientation on core face (degrees)		Second apparent orientation (degrees)		Calculated orientation (degrees)		Geographic orientation (degrees)		Comments
			Feature	(cm)	Apparent dip	Direction	Dip	Direction	Dip	Direction	Dip	Direction	
160-967A-1H-4, 93-98	5.43	F			51	270	Vertical		90	0		Microfault underlain by erosive surface	
2H-2, 45-49	11.25	F	1		28	90	0	305	43	35		Normal fault	
2H-3, 7-16	12.37	DI	0.2		Vertical		Not visible					Drilling-induced fracturing	
2H-3, 12-14	12.42	DI	0.3		82	90	0	324	83	54		Drilling-induced fracturing	
2H-3, 12-14	12.42	F	0.4		76	90						Normal fault	
2H-4, 10-16	13.90	F			44	270	0	319	52	229		Normal fault	
2H-5, 88-100	16.18	F	3		61	90	0	315	69	45		Normal fault	
2H-5, 94-100	16.24	F	0.5		61	90	0	34	65	124		Normal fault	
3H-3, 0-28	21.80	FR	4-6		79	270	0	320	82	230	58	Open fracture, with variable offset	
3H-3, 0-32	21.80	FR	0.5		Vertical		0	331	90	62	152	Open fracture, with variable offset	

Note: Feature symbols defined in Table 2 ("Explanatory Notes" chapter, this volume).

Only part of this table is reproduced here. The entire table appears on the CD-ROM (back pocket).

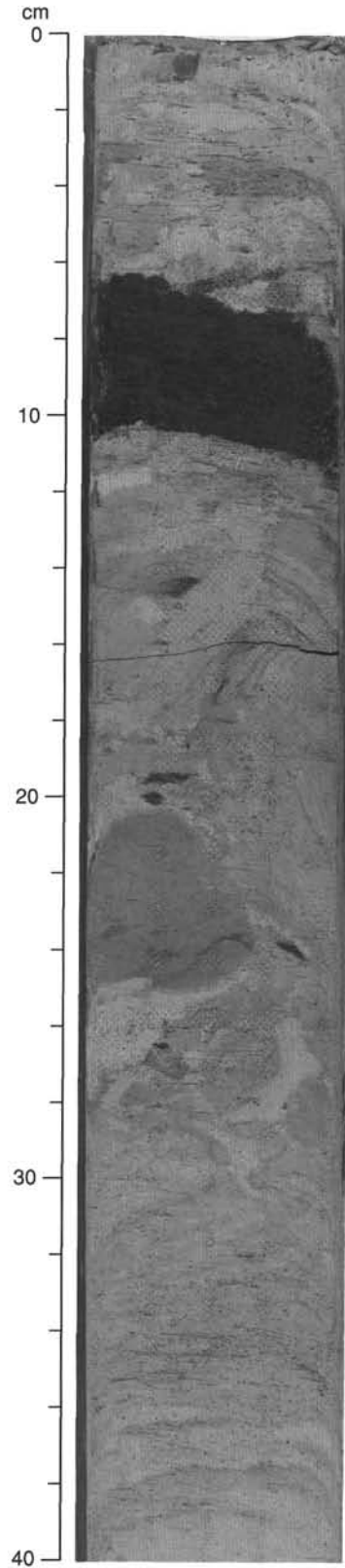


Figure 34. Debris-flow deposits showing irregular sedimentary patterns, including rotated and deformed clasts of layered sediments, a matrix consisting of nanofossil ooze, and an erosional tilted basal surface in Section 160-967A-6H-6, 0-40 cm.

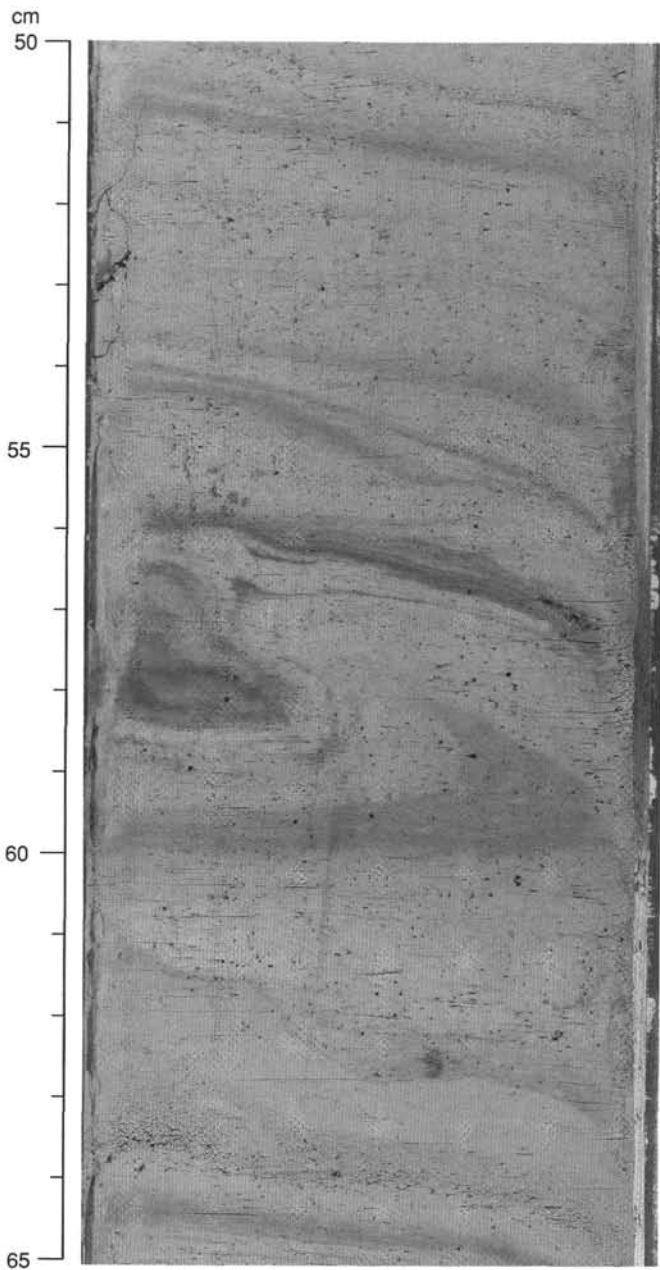


Figure 35. Slump fold in a sequence of slightly to moderately tilted nannofossil oozes that resulted from gravity-driven current deposition at Section 160-967A-7H-3, 50–65 cm. Also, see core photographs (Section 5, this volume).

table (Table 6). This discrepancy results from within-core misalignments of stratigraphic features (see discussion in previous paragraph) used to make the splice.

INORGANIC GEOCHEMISTRY

Sixteen interstitial-water samples were obtained at Site 967 from 5.95 to 150.36 mbsf, using both the standard ODP titanium/stainless-steel squeezer (Manheim and Sayles, 1974) and a Teflon-lined squeezer (Brumsack et al., 1992). The retrieved pore waters were subsequently analyzed for salinity, alkalinity, chloride, sulfate, lithium, potassium, rubidium, sodium, calcium, magnesium, strontium,

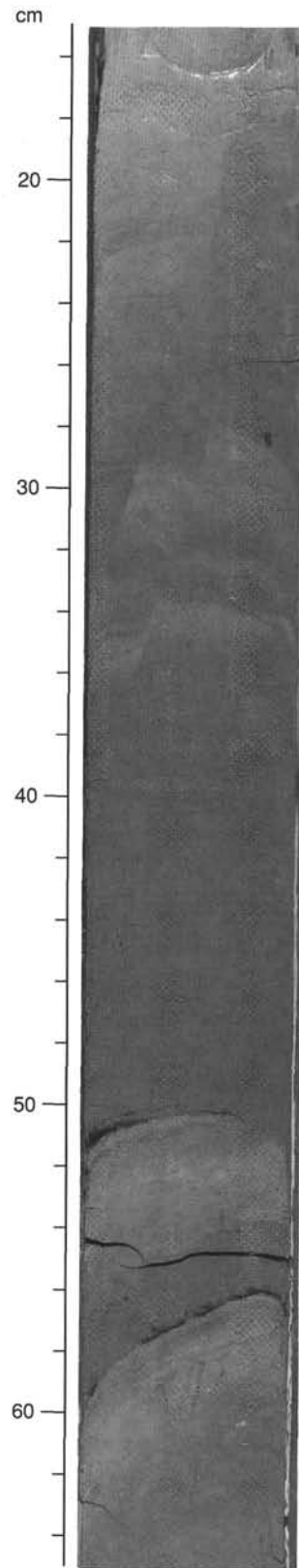


Figure 36. High-angle normal microfaults offsetting a color-laminated nannofossil ooze at Section 160-967B-3H-1, 15–65 cm.

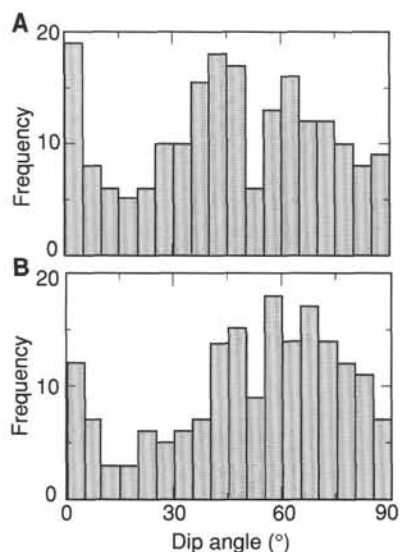


Figure 37. Frequency plot of true dip angles of microfaults measured in (A) Holes 967A and 967C for Units I and II and (B) in Hole 967E for Units III–V.

ammonium, and silica by the methods described in the “Explanatory Notes” chapter (this volume). In general, most major constituents in the top 30 m are lower than the estimated bottom-water values. It is uncertain whether this phenomenon is related to bottom-water concentrations that are relatively low at this site or to other sediment-related processes (see “Inorganic Geochemistry” section, “Site 966” chapter, this volume). Apparently, below 30 mbsf the high-salinity regime dominates the concentration-depth profiles of most elements (Table 7).

Organic Matter Degradation and Silica-Related Processes

Degradation of sedimentary organic matter at Site 967 has resulted in an increase in the pore-water contents of ammonium and alkalinity relative to seawater in the top 10–40 mbsf (Fig. 45). The slight depletion of sulfate in this depth interval indicates that minor bacterial sulfate-reduction processes do occur. The rapid release of ammonium during decomposition of organic matter in the top 10–40 mbsf may induce ion exchange reactions at mineral surfaces with a corresponding uptake of some ammonium and release of lithium, as seen in the increase in lithium in the uppermost sample compared to deep-water concentrations (Fig. 45).

The silica vs. depth profile increases sharply in the first few meters, then remains fairly constant at relatively low concentration levels of 200 μM down to 100 mbsf (Fig. 45), which suggests equilibrium with clay minerals and/or quartz. Amorphous silica phases are unlikely to be present in significant amounts. Below this depth interval a significant increase in silica up to 800 μM may be related to silica transformation reactions involving amorphous silica (opal-A/CT transformation), but contamination and/or lateral flow at 140 mbsf cannot be excluded (see also below).

Indications for the Presence of Evaporites

The profiles of salinity, chloride, and sodium vs. depth all demonstrate progressive downhole increases in Hole 967A (Fig. 46), reaching values almost twice those of seawater in the lowermost sample taken (150 mbsf). The shape of these profiles suggests that evaporites or an evaporite brine is present deeper downhole; in view of the perfect 1:1 correlation of sodium and chloride, this is presumably a halite brine or salt (Fig. 47). In addition to sodium and chloride, potassium,

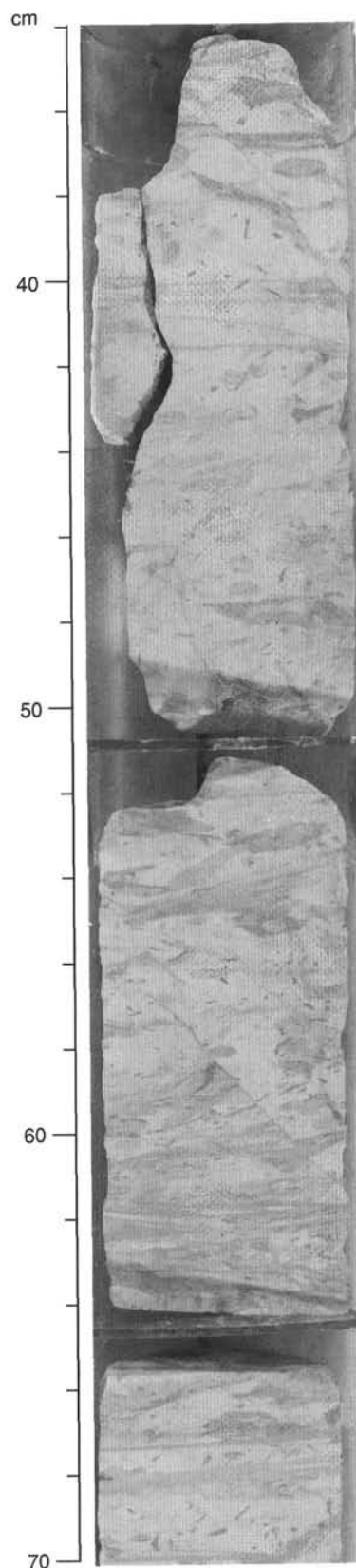


Figure 38. Steep normal faults in heavily burrowed nanofossil chinks of Unit III in Section 160-967E-9R-1, 34–70 cm. The dominant fabric is sub-horizontal and shows graded layers resulting from current deposition.

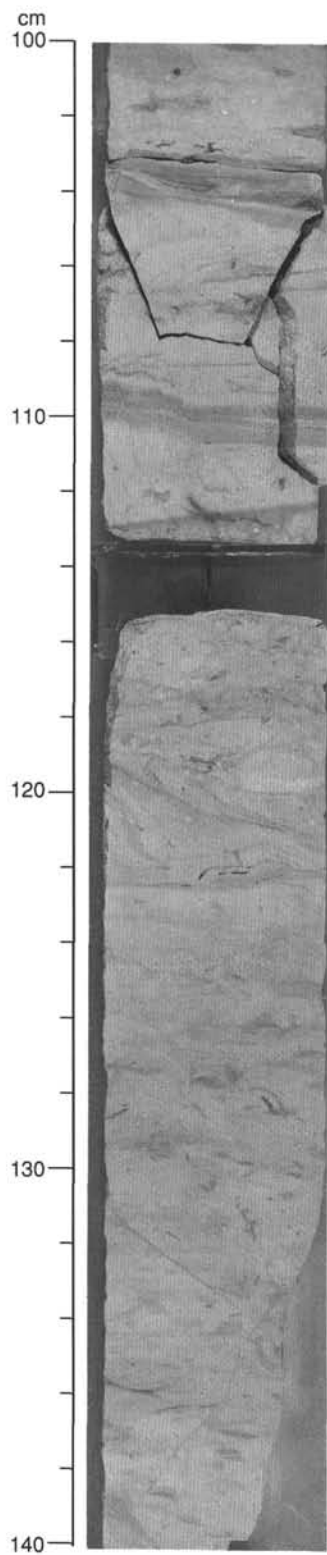


Figure 39. Example of different deformational features in the nanofossil chalk of Unit III at Section 160-967E-14R-1, 100–140 cm. Folding on a small scale occurs between 103 and 105 cm, just above a set of conjugate normal faults that offset a faintly laminated interval by about 2 mm (107–111 cm). From 115 to 122 cm, irregularly deposited (debris flow/slump?) deposits occur. In the interval below 123 cm, healed fractures and microveins cut the core face with steep dips.

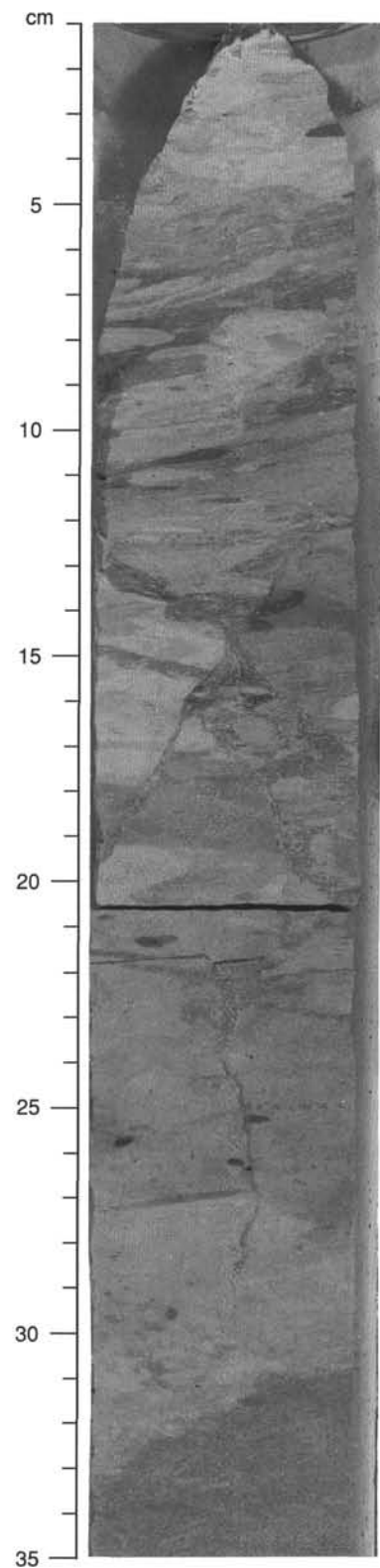


Figure 40. Set of steeply dipping normal faults crosscutting and offsetting each other observed at Section 160-967E-6R-3, 1–35 cm. The feature is interpreted as a "Neptunian dike" (see text).

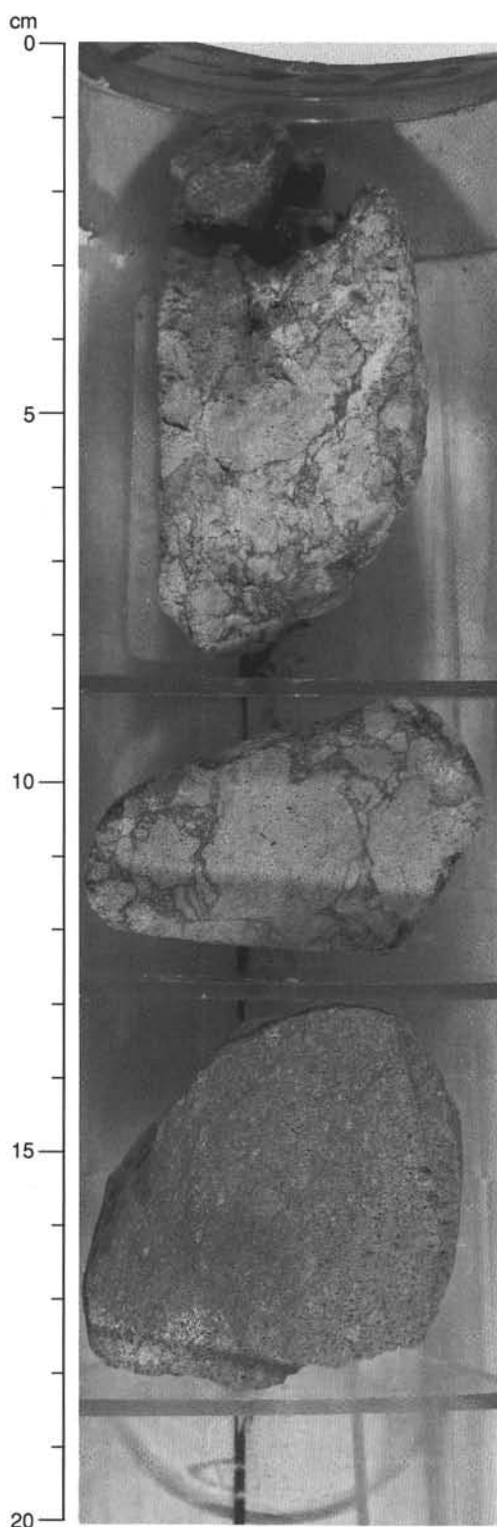


Figure 41. Two brecciated pieces and one unbroken pebble of calcarenite (Unit V) in Section 160-967E-46R-1, 0–20 cm. See text.

rubidium, strontium, and sulfate may at least partly originate from the same source (Figs. 48, 49), whereas possible relations with calcium and magnesium are highly obscured by carbonate recrystallization and precipitation reactions (Fig. 47; see the following discussion of gypsum). Extrapolations of the four lowermost data points vs. depth to zero (pure halite brine) for the strontium/chloride, magnesium/

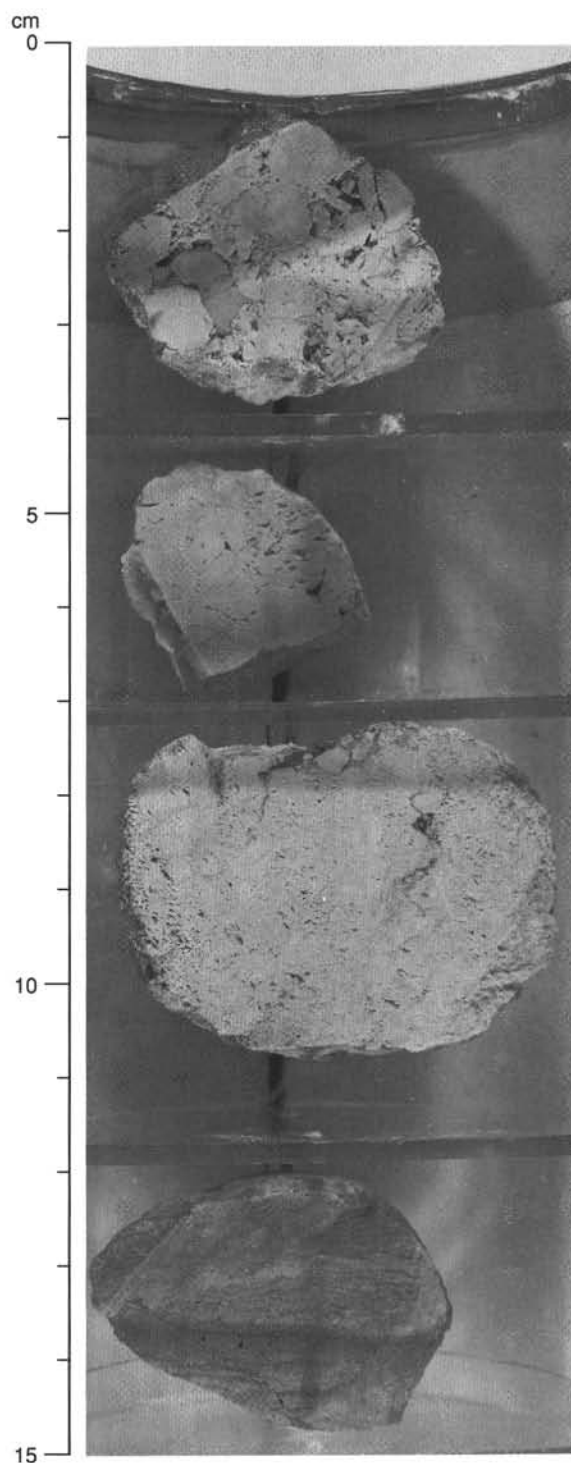


Figure 42. Four pieces of calcarenite (Unit V), three of which are brecciated and bound with calcite cements, in Section 160-967E-50R-1, 0–15 cm. See text.

chloride, and sulfate/chloride ratios (Fig. 50) point toward a surprisingly consistent depth interval of approximately 200 mbsf for the inferred halite source, provided that the lithology above and below 150 mbsf is similar. No halite has been observed at this depth in the sediments or in the logs. It must be noted that the actual presence of a halite evaporite is not necessary. The halite “source” could as well be explained by a lateral flow of a halite brine at this depth level or by a flow of lower brine concentrations at slightly shallower depth levels.

Table 5. Site 967 composite depth section.

Core	Depth (mbsf)	Offset (m)	Depth (mcd)
160-967A-			
1H	0.00	0.00	0.00
2H	9.30	0.38	9.68
3H	18.80	1.16	19.96
4H	28.30	1.88	30.18
5H	37.80	2.76	40.56
6H	47.30	3.56	50.86
7H	56.80	4.42	61.22
8H	66.30	4.82	71.12
9H	75.80	4.44	80.24
10H	85.30	3.64	88.94
11H	94.80	5.10	99.90
12H	104.30	5.98	110.28
13H	113.80	8.40	122.20
160-967B-			
1H	0.00	0.03	0.03
2H	5.30	0.88	6.18
3H	14.80	2.08	16.88
4H	24.30	3.22	27.52
5H	33.80	3.68	37.48
6H	43.30	5.00	48.30
7H	52.80	5.36	58.16
8H	62.30	7.42	69.72
9H	71.80	8.36	80.16
10H	81.30	10.06	91.36
11H	90.80	11.22	102.02
12H	100.30	12.22	112.52
13H	109.80	11.40	121.20
160-967C-			
1H	0.00	0.59	0.59
2H	9.50	1.58	11.08
3H	19.00	3.02	22.02
4H	28.50	3.20	31.70
5H	38.00	5.00	43.00
6H	47.50	6.76	54.26
7H	57.00	14.60	71.60
8H	66.50	15.36	81.86
9H	76.00	16.82	92.82
10H	85.50	17.30	102.80
11H	95.00	17.56	112.56
12H	104.50	18.62	123.12
160-967D-			
1H	0.00	0.00	0.00
2H	6.70	1.12	7.82
160-967F-			
1H	0.00	0.12	0.12

Note: See text discussion of Core 160-967A-10H offset anomaly.

Indications for the Presence of Gypsum

The concentration-depth profiles for calcium, sulfate, and strontium clearly indicate that a distinct source occurs for these elements at approximately 120 mbsf (Fig. 49). In addition, the strong correlation of strontium and sulfate in the pore waters above 120 mbsf supports the common origin of these two elements (Fig. 51). Further evidence for a non-chloride-related source for calcium, strontium, and sulfate is seen in plots of element/chloride ratios vs. depth at Hole 967A (Fig. 52).

The pore waters in the four deepest samples of this hole are saturated with respect to gypsum (Fig. 51). All evidence points to a gypsum source at 120 mbsf. Such a gypsum layer was also inferred from logging data (see "Downhole Measurements" section, this chapter). In view of the chloride, salinity, and sodium data, such a layer is unlikely to be continuous because it seems to be "transparent" for diffusion (i.e., the assumed gypsum layer is either dispersed or fractured). Such gypsum or gypsum-related units may well serve as "conduits" for lateral flow. It is unclear at this time what unit may be related to the possible lateral flow at 80 mbsf.

Lateral Flow

The lithium vs. depth profile suggests that a lithium source must be present in the lower part of this site. The lithium/chloride vs. depth

plot (Fig. 48) strongly suggests that lithium input is restricted to an interval between 80 and 120 mbsf.

The irregular shape of the ammonium profile deviates from the smooth profiles usually observed in these concentration and depth ranges (Fig. 45). If we exclude possible contamination, such deviations cannot be attributed to exchange processes and diffusion alone. Lateral advection, in particular at 120 mbsf and to a lesser extent at 80 mbsf, in combination with diffusive processes may explain the observed profiles not only of ammonium, but also of potassium, rubidium, magnesium, and lithium/chloride vs. depth at this site.

Assuming lateral flow, one may conclude that it must be more rapid at 120 mbsf than at 80 mbsf, because for several elements the deviation from a smooth, diffusion-controlled profile is larger at 120 mbsf. These fluids must be depleted in ammonium, potassium, and rubidium and enriched in lithium, magnesium, and silica. In addition, they must have a density (salinity) in line with the intervals above and below, because the salinity, chloride, and sodium vs. depth profiles have a relatively smooth shape (Fig. 46 and see above).

Because lateral flow is inferred at some depth levels at Site 967 (see discussions of the occurrence of faulting, "Structural Geology" and "Downhole Measurements" sections, this chapter), it may also be responsible for the pronounced silica profile in the lower part of this site (i.e., the sharp peak at 140 mbsf; Fig. 45). The only other element that exhibits concentration changes at this particular depth level (140 mbsf) is lithium (Fig. 45).

ORGANIC GEOCHEMISTRY

Volatile Hydrocarbons

As part of the shipboard safety and pollution-prevention monitoring program, hydrocarbon gases were analyzed in Cores 160-967A-1H through 15X, as well as in Cores 160-967E-9R, 13R, 15R, 26R, 29R, and 30R, by the headspace technique. Only trace concentrations of methane were recorded, ranging from 2 to 4 ppm at Hole 967A and from 4 to 15 ppm at Hole 967E.

Carbonate and Organic Carbon

The abundances of total, inorganic, and organic carbon and of calcium carbonate in sediments from Hole 967A are summarized in Table 8. Random sampling was performed for carbonate analysis. For organic matter assessment, samples were specifically taken from the sapropels.

Carbonate contents vary from 4% to 92% and average 38% (151 samples analyzed). In most of the sapropels carbonate contents exceed 20%. A slight tendency for higher carbonate concentrations was observed toward the lower part of the sequence (Fig. 53).

Organic carbon was determined mainly for visually distinguished organic-matter-rich intervals. Values are higher than 2%, with an average of 5% and a maximum of 7.5%. Sapropels in the deeper intervals of the sequence generally show higher organic carbon contents (Table 8, Fig. 53).

Organic Matter Type: C_{org}/N Ratios and Rock-Eval Pyrolysis

C_{org}/N ratios for all sapropels, with few exceptions in the upper part of the sequence, exceed the value of 12; they have an average of 17 and a maximum of 23.3 (Table 8, Fig. 53). As already observed for sapropels at previous sites (see "Organic Geochemistry" section, "Site 964" and "Site 966" chapters, this volume), the surprisingly high values of the C_{org}/N ratio suggest a predominance of terrestrial organic matter that is not in accordance with the indications provided by the Rock-Eval parameters. The high C_{org}/N ratios in the sapropels are tentatively interpreted as representing an effective removal of nitrogen compounds from the marine organic matter during diagenesis.

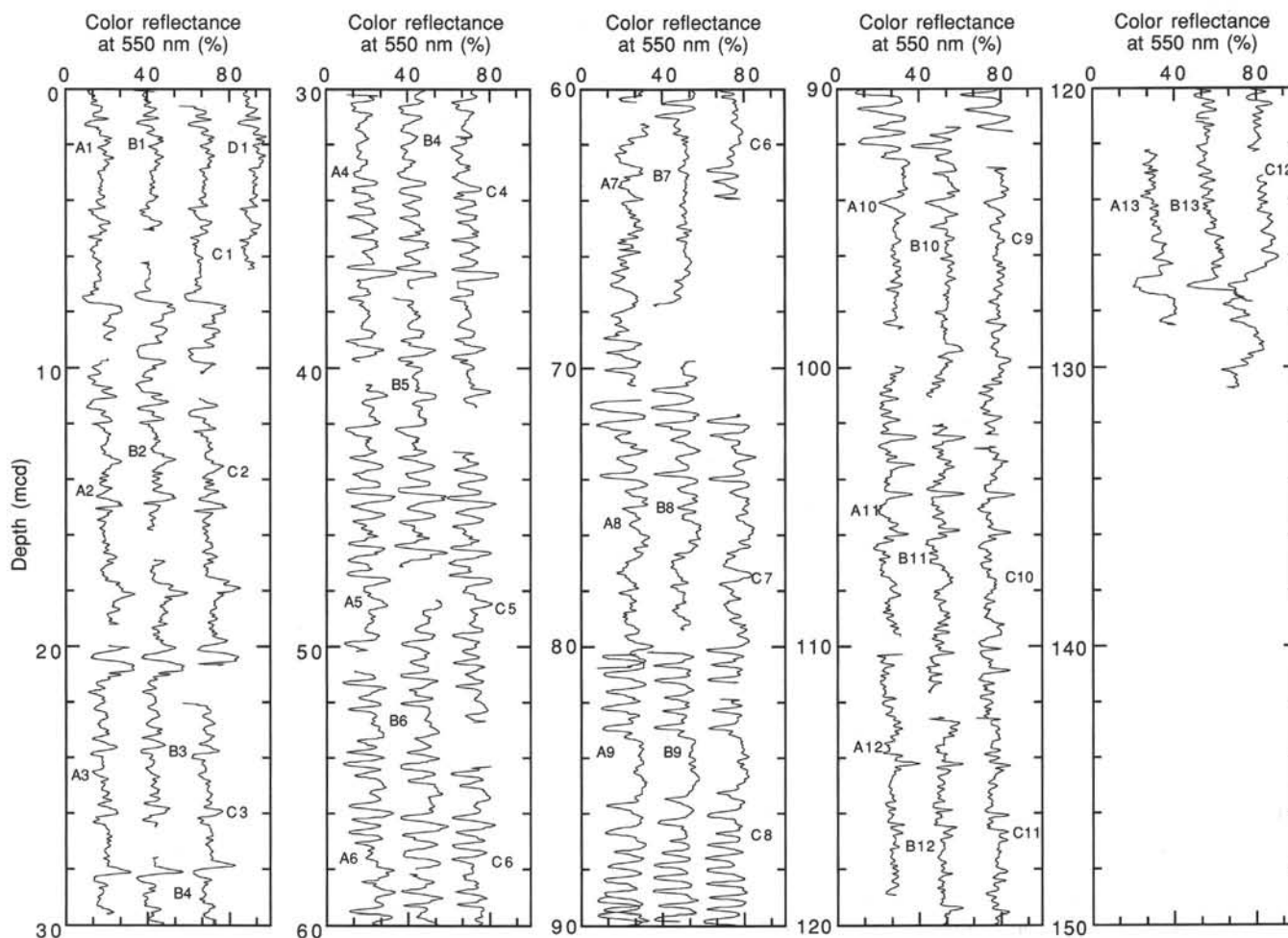


Figure 43. Percent color reflection from Site 967 on the composite depth scale. Holes 967A–967D are offset from each other by a constant (30%). Note the different scale for 0–30 mcd. Cores for each hole are shown (e.g., B3 = Core 160-967B-3H).

The possibility that the primary marine organic matter was already poor in nitrogen-bearing constituents cannot be excluded.

Results of Rock-Eval pyrolysis (Table 9) show that the hydrogen indices for many samples exceed 300, with a maximum value of 461 mg in Core 160-967A-10H. The hydrogen index values indicate partial oxidation of the primary marine organic matter and/or an admixture of terrigenous organic matter. Consistent with the relationship between organic matter type and elemental composition, the oxygen indices show an opposite trend to the hydrogen indices. Oxygen indices in samples from the upper part of the sequence (above about 40 mbsf) are relatively high because of low-temperature (<390°C) decomposition of carbonates during pyrolysis and subsequent trapping of the CO₂ formed together with that derived from organic matter decomposition. There is a general trend toward higher hydrogen indices with increasing organic matter content (Fig. 54).

Sulfur

Sulfur contents are reported in Table 8. They generally exceed 2% in sapropels, average 4%, and have a maximum of 15.5% in Sample 160-967A-8H-1, 88–89 cm. Most of the sulfur is present as pyrite because pyrite concretions were visually detected in the sapropels and abundant disseminated pyrite was observed under the microscope. No significant relationship was observed between the downhole distributions of sulfur and organic carbon.

Extractable Bitumen: Assessment of Paleotemperatures

Seventy-seven sapropel samples were analyzed for long-chain alkenones following the procedure described in the “Explanatory Notes” chapter (this volume). Long-chain alkenones are highly abundant in almost all sapropel extracts, so that ratios of di- and triunsaturated C₃₇ alkenones (U₃₇^k index) could be determined for a first approximation of paleo-sea-surface temperatures based on the calibrations of Prahl and Wakeham (1987), Brassell (1993), and Sikes and Volkman (1993). All the samples tested yielded similar temperature values. Although the ratios calculated from the gas chromatograms may provide a reasonable approximation of the relative temperature changes with age, a mass spectrometric search for compounds possibly coeluting with the alkenones (particularly with the C_{37:3} ketone at low concentrations) is necessary to validate absolute temperatures (which for this reason are not tabulated here).

As shown in Figure 55, sea-surface temperatures were generally high during the Pliocene (below about 50 mbsf) with only small variations, similar to those observed for the corresponding age interval at Site 966 (see “Organic Geochemistry” section, “Site 966” chapter, this volume). These values are higher than those estimated from alkenone indices for sapropels in the Ionian Sea at Site 964 (see “Organic Geochemistry” section, “Site 964” chapter, this volume). The extended Pleistocene section recovered at this site permits a more complete assessment of sea-surface temperatures than at Site 966.

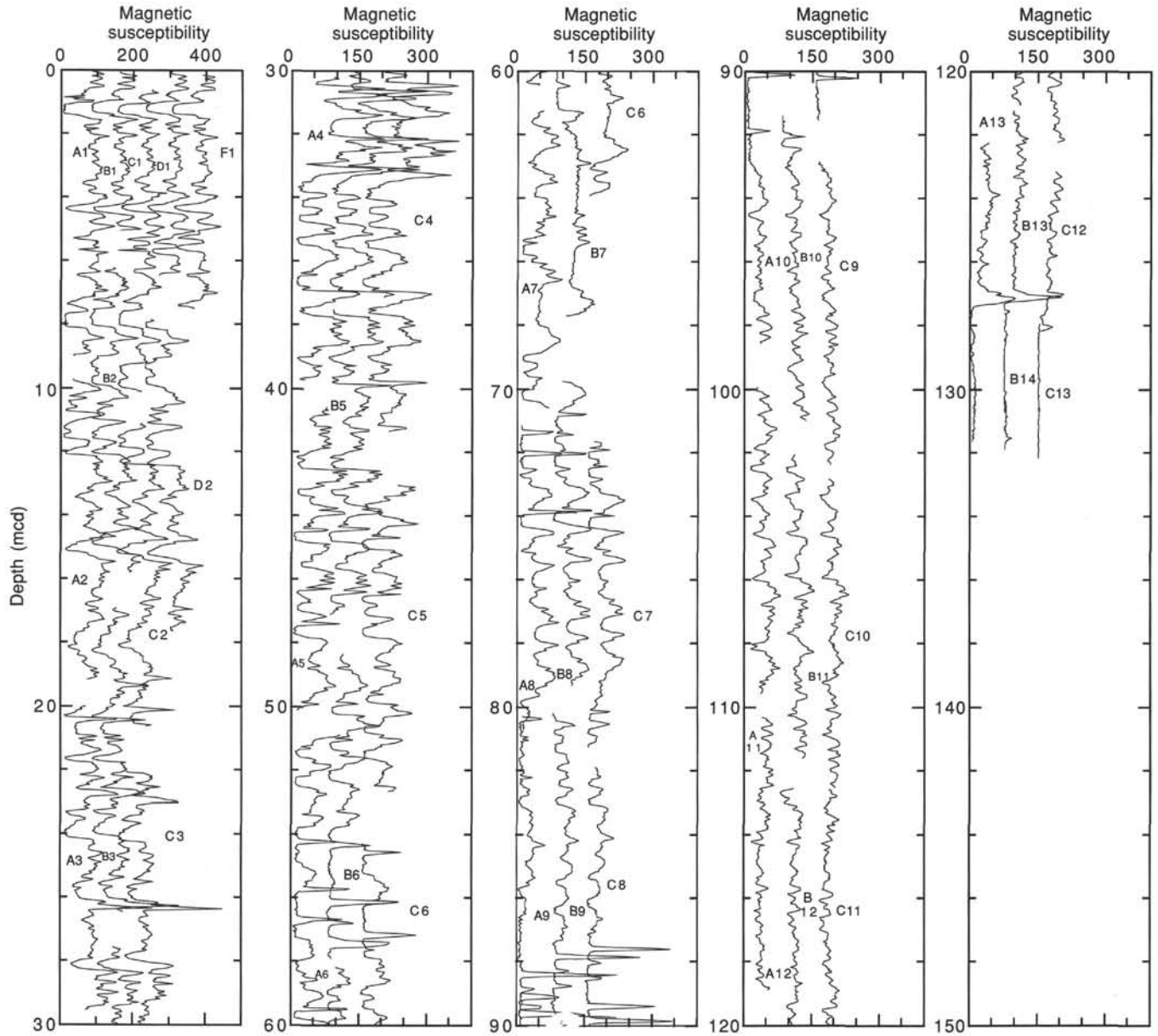


Figure 44. Magnetic susceptibility data (uncorrected instrument units) from Site 967 on the composite depth scale. Holes 967A, 967B, 967C, 967D, and 967E are offset from each other by a constant (50 instrument units). Cores for each hole are shown (e.g., B3 = Core 160-967B-3H).

Variations are more pronounced than in the Pliocene and occur at an average temperature approximately 2°–3°C lower than in the older section. Again, the average temperature is higher and the fluctuations are at smaller amplitudes than in the Ionian Sea (see “Organic Geochemistry” section, “Site 964” chapter, this volume).

The alkenone sea-surface temperature pattern is in general accordance with the results of previous geochemical studies on Mediterranean sapropels (ten Haven, 1986; ten Haven et al., 1987; K.C. Emeis, pers. comm., 1995) and the current understanding of climate development during the past few million years.

PHYSICAL PROPERTIES

Standard physical properties (see “Explanatory Notes” chapter, this volume) were measured in all APC cores obtained at Site 967 and

on lithified samples from RCB and XCB cores (Tables 10–13), although poor recovery limited access to lithified samples. In this section, we describe the downhole distribution of measured physical properties from Hole 967A obtained from APC cores to 140 mbsf and from Hole 967E obtained from RCB and XCB cores between 130 and 570 mbsf.

Index Properties

Bulk and dry densities were measured in every section of unconsolidated sediment down to 140 mbsf. Both increase sharply in the first 10 mbsf (Table 10), which parallels the loss of porosity and water from the sediment/water interface downward (Fig. 56). Between 10 and 140 mbsf, a steady increase in bulk density is matched by decreasing porosity and water content. Below 140 mbsf, the fully lithified nature of the rocks recovered from Hole 967E is reflected in the

Table 6. Site 967 splice tie points.

Hole, core, section, interval (cm)	Depth (mbsf)	Depth (mcd)		Hole, core, section, interval (cm)	Depth (mbsf)	Depth (mcd)
967D-1H-5, 26.0	6.26	6.26	ties to	967A-1H-5, 26.0	6.26	6.26
967A-1H-6, 96.0	8.46	8.46	ties to	967B-2H-2, 78.0	7.58	8.46
967B-2H-3, 86.0	9.16	10.04	ties to	967A-2H-1, 36.0	9.66	10.04
967A-2H-6, 132.0	18.12	18.50	ties to	967B-3H-2, 12.0	16.42	18.50
967B-3H-3, 86.0	18.66	20.74	ties to	967A-3H-1, 78.0	19.58	20.74
967A-3H-6, 44.0	26.74	27.90	ties to	967B-4H-1, 38.0	24.68	27.90
967B-4H-3, 98.0	28.28	31.50	ties to	967A-4H-1, 132.0	29.62	31.50
967A-4H-7, 20.0	37.50	39.38	ties to	967B-5H-2, 40.0	35.70	39.38
967B-5H-3, 50.0	37.30	40.98	ties to	967A-5H-1, 42.0	38.22	40.98
967A-5H-7, 6.0	46.86	49.62	ties to	967B-6H-1, 132.0	44.62	49.62
967B-6H-6, 38.0	51.18	56.18	ties to	967C-6H-2, 42.0	49.42	56.18
967C-6H-4, 24.0	52.24	59.00	ties to	967B-7H-1, 84.0	53.64	59.00
967B-7H-3, 8.0	55.88	61.24	ties to	967A-7H-1, 2.0	56.82	61.24
967A-7H-7, 28.0	66.08	70.50	ties to	967B-8H-1, 78.0	63.08	70.50
967B-8H-5, 96.0	69.26	76.68	ties to	967C-7H-4, 58.0	62.08	76.68
967C-7H-7, 30.0	66.30	80.90	ties to	967B-9H-1, 74.0	72.54	80.90
967B-9H-2, 84.0	74.14	82.50	ties to	967C-8H-1, 64.0	67.14	82.50
967C-8H-6, 110.0	75.10	90.46	ties to	967A-10H-2, 2.0	86.82	90.46
967A-10H-4, 34.0	90.14	93.78	ties to	967B-10H-2, 92.0	83.72	93.78
967B-10H-7, 60.0	90.90	100.96	ties to	967A-11H-1, 106.0	95.86	100.96
967A-11H-4, 14.0	99.44	104.54	ties to	967B-11H-2, 102.0	93.32	104.54
967B-11H-6, 106.0	99.36	110.58	ties to	967A-12H-1, 30.0	104.60	110.58
967A-12H-3, 94.0	108.24	114.22	ties to	967B-12H-2, 20.0	102.00	114.22
967B-12H-5, 126.0	107.56	119.78	ties to	967C-11H-5, 122.0	102.22	119.78
967C-11H-7, 58.0	104.58	122.14	ties to	967B-13H-1, 94.0	110.74	122.14

Table 7. Results of pore-water analysis for Site 967.

Core, section, interval (cm)	Depth (mbsf)	pH	Alkalinity (meq/L)	Salinity (g/kg)	Cl ⁻ (mM)	Mg ²⁺ (mM)	Ca ²⁺ (mM)	SO ₄ ²⁻ (mM)	NH ₄ ⁺ (μM)	SiO ₂ (μM)	K ⁺ (mM)	Sr ²⁺ (μM)	Li ⁺ (μM)	Na ⁺ (mM)
160-967A-														
1H-4, 145-150	5.98	7.63	4.873	38.0	606	57.5	12.0	30.0	124	222	10.9	121	34	509
2H-4, 145-150	15.48	7.43	4.844	38.0	605	56.1	11.5	29.4	193	171	10.6	135	32	520
3H-4, 145-150	24.98	7.33	4.162	38.5	605	57.2	10.7	30.1	262	154	11.4	151	34	517
4H-4, 145-150	34.48	7.29	3.965	38.5	613	57.7	11.7	31.2	300	160	10.7	176	37	497
5H-4, 145-150	43.98	7.53	3.856	40.0	624	58.9	12.7	32.9	341	152	10.8	203	39	524
6H-4, 145-150	53.48	7.42	3.898	40.5	632	60.7	14.2	32.5	330	175	10.9	235	42	520
7H-4, 145-150	62.98	7.35	3.583	41.0	639	61.2	15.8	35.1	309	179	9.9	280	44	528
8H-4, 145-150	72.48	7.39	3.296	41.5	651	62.8	18.9	36.5	303	186	10.3	325	46	524
9H-4, 145-150	81.98	7.37	3.095	43.0	677	64.6	21.6	38.4	285	198	9.8	380	50	550
10H-4, 145-150	91.48	7.16	2.928	44.5	688	64.2	24.6	40.4	326	190	10.6	415	51	598
11H-4, 145-150	100.98	7.42	2.545	46.0	711	65.2	27.7	41.2	318	176	11.0	455	52	602
12H-4, 140-150	110.45	7.37	2.590	47.5	743	66.2	32.2	44.0	318	241	11.5	520	54	641
13H-5, 140-150	121.45	—	—	51.0	781	73.1	38.5	48.0	253	335	8.8	630	56	645
14X-4, 140-150	129.45	7.42	1.339	54.0	819	68.7	39.7	48.0	312	319	11.9	610	56	696
15X-3, 140-150	137.45	—	—	54.2	856	67.6	39.9	43.2	342	807	14.0	535	53	716
160-967E-														
5R-2, 86-99	150.36	—	—	65.0	1053	66.7	46.3	42.3	413	260	19.3	595	61	913

Note: — = no data.

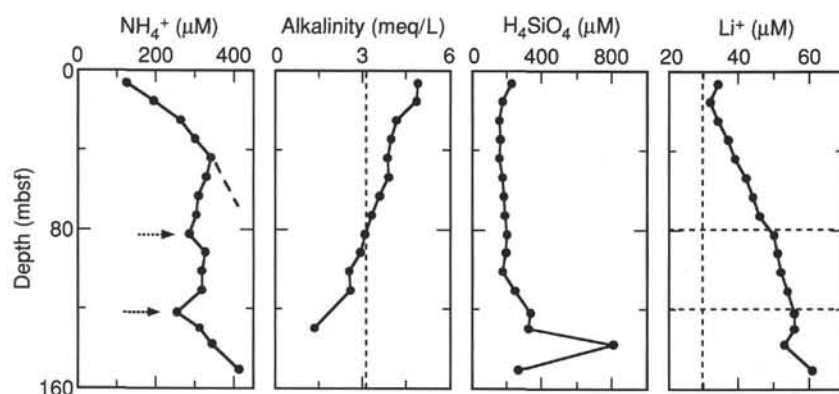


Figure 45. Pore-water vs. depth profiles in Hole 967A for ammonium, alkalinity, silica, and lithium. The vertical dashed line indicates the bottom-water concentration; the ammonium bottom-water concentration is <1 μM. See the discussion of the 80–120 mbsf interval (indicated by arrows and dashed lines) in the text.

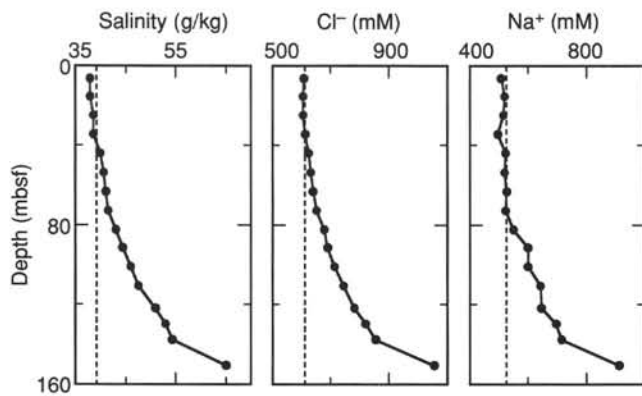


Figure 46. Pore-water vs. depth profiles in Hole 967A for salinity, chloride, and sodium. The dashed line indicates the bottom-water concentration.

abrupt increase in density and decrease in porosity and water content. Index properties densities are systematically higher than logging densities. This implies that the samples recovered may be biased to higher density because they are more mechanically resistant to drilling and coring.

Discrete-sample *P*-wave and Strength Measurements

Horizontal and vertical *P*-wave velocities measured with the digital sonic velocimeter show a generally increasing trend with depth in Holes 967A and 967E (Table 11, Fig. 57), with an abrupt increase from 1.7 to 2.3 km/s at the transition from soft oozes to lithified carbonates. Comparison of the laboratory data with results from downhole measurements shows good agreement and no systematic deviation, which indicates that the available samples are representative of the compressional wave velocity of that interval.

Shear strength, measured in split APC cores using the motorized vane-shear device, shows an overall downhole increase (Table 12, Fig. 57). In detail, a sharp increase in shear strength can be observed in the soft oozes at the transition to lithified carbonates (120–140 mbsf) where the compressional wave velocities increase. A second variation in the pattern of data distribution can be discerned at 60 mbsf, where a distinct rise in shear strength and an increase in scatter are evident.

GRAPE Density

The overall trend of the GRAPE data (Fig. 58A) is toward slightly increasing density with depth, and the rate of density increase is low but constant. A comparison of index properties density measurements with GRAPE density (Fig. 58A) suggests that GRAPE measurements in this hole underestimate density, despite application of the Boyce correction (see “Explanatory Notes” chapter, this volume). This may result from the fact that the calcite mineralogy in the hole differs from the quartz mineralogy assumed in the correction. In addition, GRAPE density is measured in undrained cores, and index properties sample preparation involves some water loss. In order to test the reliability of the GRAPE measurements, we resampled the GRAPE data to match the sample spacing of the index properties measurements. A linear regression ($R = 0.83$) of the two density measures confirms that the corrected GRAPE values underestimate density, but suggests that the GRAPE variations do represent real density changes. Figure 58B indicates that a linear correction could be applied to readjust the GRAPE data.

P-wave Velocity

High-resolution compressional wave velocities were measured using the PWL of the MST (Fig. 59A). The data exhibit two discern-

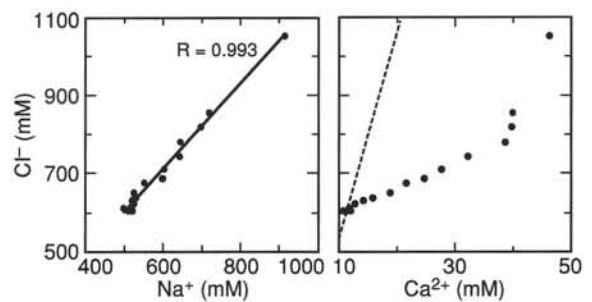


Figure 47. Plots of pore-water data from Hole 967A for chloride vs. sodium and chloride vs. calcium. The dashed line indicates the seawater ratio.

ible increases, one at 60 mbsf and the other at 110 mbsf, and considerable scatter below 125 mbsf. In the transition zone from oozes to carbonates, high velocities from split cores agree with the bottom portion of the PWL velocity plot. A linear regression between discrete-sample velocities and resampled PWL velocities (Fig. 59B) indicates a good correlation ($R = 0.94$). The PWL data appear to be a reliable indicator of downhole velocity changes.

Magnetic Susceptibility

Figure 60 shows the results of magnetic susceptibility measurements from Hole 967A. The general trends of the data are (1) gradually decreasing susceptibility with depth to 80 mbsf; (2) decreasing values between 80 and 90 mbsf; (3) a steplike increase at 90 mbsf; (4) approximately constant values and reduced scatter down to 120 mbsf; (5) a steplike decrease at 120 mbsf; and (6) a constant trend with increased scatter below 120 mbsf. On a finer scale, considerable variation occurs.

Natural Gamma-ray Radiation

NGR values measured for Hole 967A using the MST show several first-order trends (Fig. 61). The general trend is a decrease with depth. Between 0 and 90 mbsf, the scatter of the NGR values is clearly larger than in the lower part; at 120 mbsf, the NGR values increase abruptly again, then decrease again at 130 mbsf. These large-scale variations are correlated ($R = 0.78$) to the amount of organic carbon in the sediments (Fig. 61B). Superposed on these first-order trends are many centimeter- to decimeter-scale variations; the cause of these cannot be inferred from the lithologic descriptions.

Thermal Conductivity

Thermal conductivity at Hole 967A was sampled once per section in all APC cores and at irregular intervals in the RCB cores from Hole 967E (Table 13, Fig. 62). For the hard rocks, the half-space line source was used (see “Explanatory Notes” chapter, this volume). Thermal conductivity values increase overall downhole, but show large variations on the scale of a few meters. This fluctuation is similar to that seen in MST data and probably reflects an interplay of geochemical, sedimentary, and possibly structural effects. The overall increase in thermal conductivity values results from decreasing water content.

Correlation of Lithology and Organic Carbon Content with Physical Properties

The physical properties of the sequence cored in Hole 967A outline five units (Table 14): an upper unit between 0 and 60 mbsf of Pleistocene age; a second unit from 60 to 70 mbsf, which is described as a debris flow; a third unit from 70 to 90 mbsf; a fourth unit between 90 and 120 mbsf; and a fifth unit between 120 and 135 mbsf, which

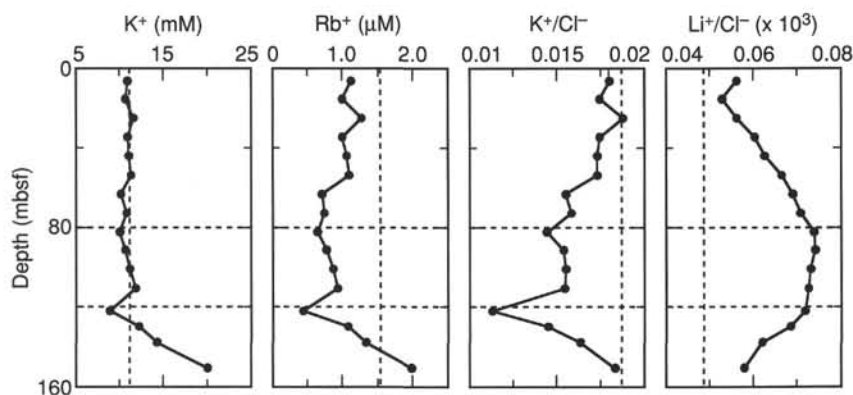


Figure 48. Pore-water vs. depth profiles in Hole 967A for potassium, rubidium, potassium/chloride ratio, and lithium/chloride ratio. The vertical dashed line indicates the bottom-water concentration. See the discussion of the 80–120 mbsf interval in the text.

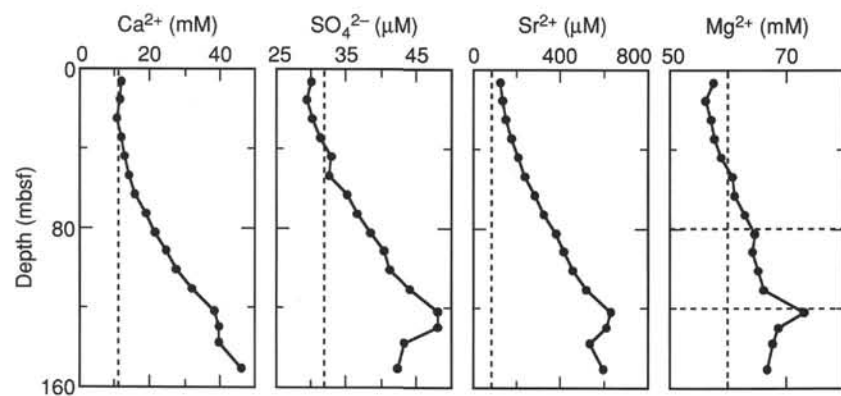


Figure 49. Pore-water vs. depth profiles in Hole 967A for calcium, sulfate, strontium, and magnesium. The vertical dashed line indicates the bottom-water concentration. See the discussion of the 80–120 mbsf interval in the text.

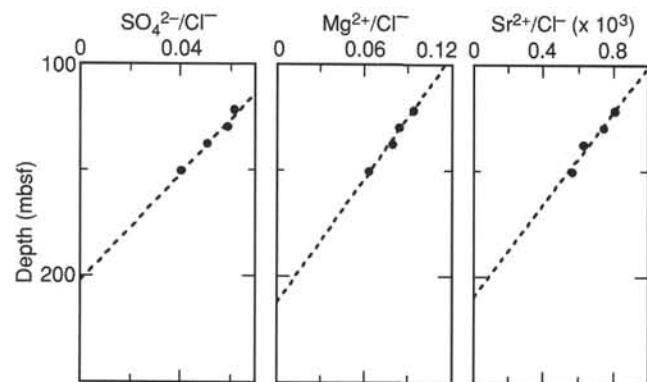


Figure 50. Extrapolation of pore-water vs. depth profiles in Hole 967A for the sulfate/chloride ratio, magnesium/chloride ratio, and strontium/chloride ratio.

comprises calcareous fragments and reworked sediments. The change from the fourth to the fifth unit corresponds to the transition from unconsolidated sediments to sediments containing fragments of carbonate rocks. This is the transition between the Pliocene sequence to the underlying series of reworked material, containing mainly Eocene to Miocene fossils.

A good correlation between the amount of organic carbon in the sediments and NGR can be seen in Figure 62B. The role of C_{org} in determining physical properties is constrained by the correlation of C_{org} with NGR and other physical properties. In Hole 967A, the low C_{org} content corresponds to low values of NGR, water content, and porosity and to high values of color reflectance, compressional wave velocity, and density.

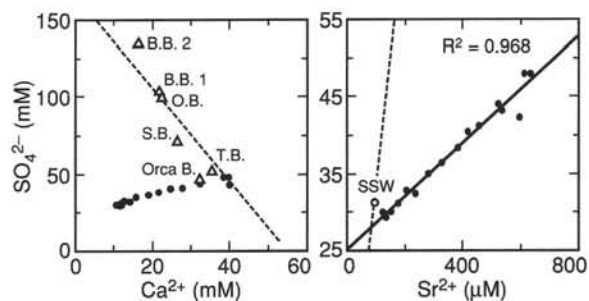


Figure 51. Plots for pore-water data of Hole 967A for sulfate vs. calcium and sulfate vs. strontium. The dashed line in the calcium plot indicates the assumed brine gypsum saturation line; B.B. = Bannock Basin, O.B. = Ostra Basin; S.B. = Scirocco Basin, T.B. = Tyro Basin (all Eastern Mediterranean; de Lange et al., 1990), and Orca Basin, Gulf of Mexico. The dashed line in the strontium plot indicates the seawater ratio; SSW = Mediterranean surface-seawater composition.

DOWNHOLE MEASUREMENTS

Logging Operations and Quality of Logs

At Site 967, a full suite of log data was acquired using the Quad combination, Formation MicroScanner, geochemical logging, and geological high-sensitivity magnetic tool strings (see “Explanatory Notes” chapter, this volume). The Lamont-Doherty temperature logging tool was attached to the bottom of the Quad combination and GLT tool strings. After coring and drilling operations were completed in Hole 967E, the borehole was conditioned with sepiolite drilling mud mixed with seawater. The base of the BHA was set at 91.43 mbsf and pulled up during logging to 72.9 mbsf to maximize the in-

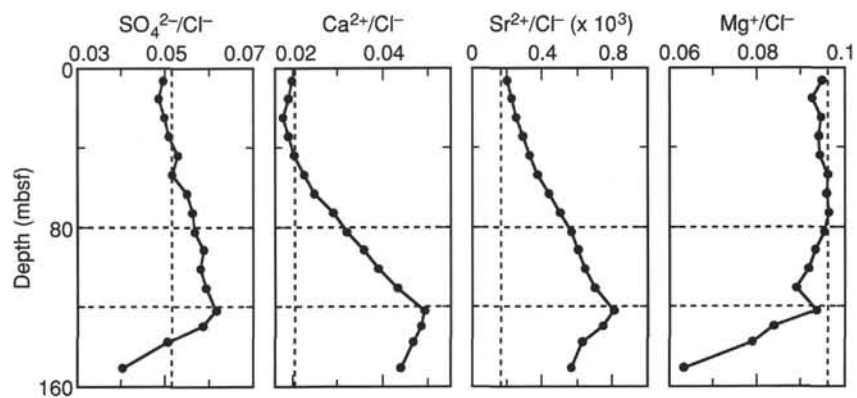


Figure 52. Pore-water vs. depth profiles in Hole 967A for the sulfate/chloride ratio, calcium/chloride ratio, strontium/chloride ratio, and magnesium/chloride ratio. The vertical dashed line indicates the bottom-water concentration. See the discussion of the 80–120 mbsf interval in the text.

Table 8. Concentration of total, inorganic, and organic carbon, calcium carbonate, total nitrogen, and sulfur in sediments from Hole 967A.

Core, section, interval (cm)	Depth (mbsf)	Total carbon (%)	Inorganic carbon (%)	Organic carbon (%)	CaCO ₃ (%)	Nitrogen (%)	Sulfur (%)	C _{org} /N	C _{org} /S
160-967A-									
1H-1, 122-123	1.22	6.53	4.15	2.38	34.57	0.20	2.71	11.9	0.9
1H-1, 140-141	1.40		4.30		35.82				
1H-2, 70-71	2.20		3.82		31.82				
1H-3, 69-70	3.69		3.71		30.90				
1H-3, 132-133	4.32	7.01	3.97	3.04	33.07	0.21	3.85	14.5	0.8
1H-4, 70-71	5.20	3.22	2.95	0.27	24.57	0.05	0.19	5.4	1.4
1H-4, 80-81	5.30	6.20	3.62	2.58	30.15	0.19	4.64	13.6	0.6
1H-5, 70-71	6.70	1.79	1.46	0.33	12.16	0.04	0.14	8.3	2.4
1H-5, 133-134	7.33	1.86	0.74	1.12	6.16	0.08	2.18	14.0	0.5
1H-5, 145-146	7.45	12.36	3.77	8.59	31.40	0.51	4.73	16.8	1.8
1H-6, 25-26	7.75		4.94		41.15				
1H-6, 70-71	8.20		5.59		46.56				
1H-7, 40-41	8.90		4.46		37.15				
1H-CC, 8-9	9.13	7.74	3.47	4.27	28.91	0.25	2.46	17.1	1.7
2H-1, 64-65	9.94	10.39	3.75	6.64	31.24	0.36	5.98	18.4	1.1
2H-1, 87-88	10.17	1.86	1.16	0.70	9.66	0.06	1.60	11.7	0.4
2H-1, 145-146	10.75	6.15	4.20	1.95	34.99	0.14	2.17	13.9	0.9
2H-2, 17-18	10.97	8.25	5.64	2.61	46.98	0.16	3.34	16.3	0.8
2H-2, 60-61	11.40		3.65		30.40				
2H-2, 84-85	11.64	6.95	3.90	3.05	32.49	0.19	4.70	16.1	0.6
2H-3, 60-61	12.90		6.11		50.90				
2H-4, 60-61	14.40		5.46		45.48				
2H-4, 88-89	14.68	7.29	4.64	2.65	38.65	0.17	3.00	15.6	0.9
2H-5, 60-61	15.90		2.82		23.49				
2H-6, 22-23	17.02	1.96	1.72	0.24	14.33	0.04	0.20	6.0	1.2
2H-6, 60-61	17.40		3.32		27.66				
2H-CC, 10-11	18.95	1.54	1.28	0.26	10.66	0.04	0.14	6.5	1.9
3H-1, 35-36	19.15	7.13	3.83	3.30	31.90	0.19	3.72	17.4	0.9
3H-1, 49-50	19.29	5.11	3.78	1.33	31.49	0.09	0.58	14.8	2.3
3H-1, 90-91	19.70		8.18		68.14				
3H-1, 127-128	20.07	6.77	4.91	1.86	40.90	0.13	0.23	14.3	8.1
3H-2, 20-21	20.50	7.29	4.60	2.69	38.32	0.16	1.80	16.8	1.5
3H-2, 110-111	21.40		4.59		38.23				
3H-3, 35-36	22.15	6.82	2.94	3.88	24.49	0.22	4.61	17.6	0.8
3H-3, 86-87	22.66	1.45	0.42	1.03	3.50	0.07	2.13	14.7	0.5
3H-3, 95-96	22.75	8.51	3.75	4.76	31.24	0.22	5.22	21.6	0.9
3H-4, 5-6	23.35		4.67		38.90				
3H-4, 122-123	24.52	5.41	4.13	1.28	34.40	0.10	0.60	12.8	2.1
3H-5, 109-110	25.89		4.25		35.40				
3H-6, 30-31	26.60		3.85		32.07				
3H-6, 82-83	27.12	2.21	0.94	1.27	7.83	0.09	0.99	14.1	1.3
4H-1, 34-35	28.64	2.21	1.60	0.61	13.33	0.05	0.18	12.2	3.4
4H-1, 99-100	29.29	3.15	2.98	0.17	24.82	0.03	0.06	5.7	2.8
4H-2, 129-130	31.09	9.74	3.21	6.53	26.74	0.28	3.05	23.3	2.1
4H-3, 34-35	31.64	8.53	2.61	5.92	21.74	0.30	2.68	19.7	2.2
4H-3, 48-49	31.78	5.36	3.44	1.92	28.66	0.12	3.31	16.0	0.6
4H-3, 93-94	32.23	7.42	2.91	4.51	24.24	0.25	4.86	18.0	0.9
4H-3, 140-141	32.70	9.08	3.24	5.84	26.99	0.33	5.52	17.7	1.1
4H-4, 62-63	33.42	9.05	4.45	4.60	37.07	0.26	9.04	17.7	0.5
4H-4, 95-96	33.75		6.42		53.48				
4H-5, 20-21	34.50	11.03	1.69	9.34	14.08	0.48	7.67	19.5	1.2
4H-5, 70-71	35.00	8.03	3.99	4.04	33.24	0.23	4.61	17.6	0.9
4H-5, 130-131	35.60	7.92	1.90	6.02	15.83	0.30	4.48	20.1	1.3
4H-6, 70-71	36.50		2.06		17.16				
4H-6, 136-137	37.16	10.40	3.76	6.64	31.32	0.37	4.29	17.9	1.5
4H-7, 30-31	37.60		6.36		52.98				
4H-7, 52-53	37.82	8.28	3.79	4.49	31.57	0.23	8.82	19.5	0.5
5H-1, 80-81	38.60		4.66		38.82				
5H-2, 12-13	39.42	6.57	2.40	4.17	19.99	0.25	7.90	16.7	0.5
5H-2, 32-33	39.62	7.19	4.92	2.27	40.98	0.15	4.81	15.1	0.5
5H-2, 115-116	40.45	8.35	3.52	4.83	29.32	0.28	6.57	17.3	0.7
5H-3, 25-26	41.05	5.02	3.67	1.35	30.57	0.10	1.67	13.5	0.8
5H-3, 87-88	41.67	9.10	2.36	6.74	19.66	0.37	5.94	18.2	1.1
5H-3, 110-111	41.90		6.47		53.90				
5H-3, 140-141	42.20	3.40	2.16	1.24	17.99	0.09	1.40	13.8	0.9

Table 8 (continued).

Core, section, interval (cm)	Depth (mbsf)	Total carbon (%)	Inorganic carbon (%)	Organic carbon	CaCO ₃ (%)	Nitrogen (%)	Sulfur (%)	C _{org} /N	C _{org} /S
5H-4, 42-43	42.72	6.90	2.43	4.47	20.24	0.28	8.00	16.0	0.6
5H-4, 63-64	42.93		4.57		38.07				
5H-4, 122-123	43.52	9.52	2.30	7.22	19.16	0.39	9.52	18.5	0.8
5H-5, 20-21	44.00	5.80	3.97	1.83	33.07	0.14	1.42	13.1	1.3
5H-5, 32-33	44.12	6.38	3.68	2.70	30.65	0.19	3.32	14.2	0.8
5H-5, 85-86	44.65	9.40	2.81	6.59	23.41	0.35	5.93	18.8	1.1
5H-6, 40-41	45.70		6.38		53.15				
5H-7, 36-37	47.16	8.03	2.79	5.24	23.24	0.28	3.92	18.7	1.3
5H-CC, 29-30	47.73	4.16	2.52	1.64	20.99	0.12	1.35	13.7	1.2
6H-1, 24-25	47.54		5.31		44.23				
6H-1, 40-41	47.70	12.19	2.50	9.69	20.83	0.52	6.82	18.6	1.4
6H-1, 138-139	48.68	10.91	3.88	7.03	32.32	0.40	8.13	17.6	0.9
6H-2, 50-51	49.30		6.52		54.31				
6H-2, 100-101	49.80	6.77	4.82	1.95	40.15	0.15	1.29	13.0	1.5
6H-2, 142-143	50.22	10.23	3.30	6.93	27.49	0.36	7.24	19.3	1.0
6H-3, 36-37	50.66	9.88	3.36	6.52	27.99	0.36	4.90	18.1	1.3
6H-3, 44-45	50.74		5.60		46.65				
6H-3, 75-76	51.05	9.76	3.79	5.97	31.57	0.34	4.70	17.6	1.3
6H-4, 37-38	52.17	10.47	3.31	7.16	27.57	0.39	6.45	18.4	1.1
6H-4, 82-83	52.62	6.95	4.27	2.68	35.57	0.17	2.12	15.8	1.3
6H-4, 128-129	53.08	10.02	2.17	7.85	18.08	0.37	4.66	21.2	1.7
6H-5, 18-19	53.48	7.24	3.10	4.14	25.82	0.23	2.29	18.2	1.8
6H-5, 50-51	53.80		5.76		47.98				
6H-6, 9-10	54.89	11.04	4.39	6.65	36.57	0.34	3.42	19.8	1.9
6H-6, 112-113	55.92	12.02	2.07	9.95	17.24	0.46	6.88	21.6	1.4
6H-7, 30-31	56.60		6.25		52.06				
7H-1, 80-81	57.60		5.97		49.73				
7H-2, 80-81	59.10		4.58		38.15				
7H-3, 100-101	60.80		6.22		51.81				
7H-3, 116-117	60.96	10.26	5.80	4.46	48.31	0.24	2.21	18.4	2.0
7H-3, 130-131	61.10	10.19	3.96	6.23	32.99	0.30	4.07	20.7	1.5
7H-4, 5-6	61.35	8.69	4.02	4.67	33.49	0.26	3.89	17.7	1.2
7H-4, 80-81	62.10		5.89		49.06				
7H-6, 21-22	64.51	8.16	4.23	3.93	35.24	0.21	6.31	18.7	0.6
7H-6, 74-75	65.04	8.47	4.84	3.63	40.32	0.20	4.39	18.2	0.8
7H-6, 130-131	65.60	7.41	4.02	3.39	33.49	0.18	0.71	18.4	4.8
7H-6, 135-136	65.65	9.93	4.25	5.68	35.40	0.29	2.99	19.9	1.9
7H-CC, 13-14	66.37		5.45		45.40				
7H-CC, 26-27	66.50	10.50	4.33	6.17	36.07	0.29	5.52	21.6	1.1
7H-CC, 34-35	66.58	11.03	4.05	6.98	33.74	0.33	3.86	21.3	1.8
8H-1, 20-21	66.50	10.20	4.15	6.05	34.57	0.29	6.36	21.2	1.0
8H-1, 88-89	67.18	9.16	3.19	5.97	26.57	0.29	15.47	20.7	0.4
8H-2, 73-74	68.53		4.51		37.57				
8H-2, 123-124	69.03	10.73	2.71	8.02	22.57	0.37	6.39	21.5	1.3
8H-4, 73-74	71.53		7.44		61.98				
8H-6, 73-74	74.53		5.73		47.73				
8H-7, 62-63	75.92		6.86		57.14				
8H-CC, 10-11	76.10	14.23	5.43	8.80	45.23	0.40	5.02	22.3	1.8
9H-1, 9-10	75.89	14.11	4.12	9.99	34.32	0.50	3.58	20.0	2.8
9H-1, 71-72	76.51	11.37	5.69	5.68	47.40	0.29	5.14	19.6	1.1
9H-1, 122-123	77.02		5.21		43.40				
9H-2, 51-52	77.81	9.10	6.43	2.67	53.56	0.16	5.84	16.7	0.5
9H-2, 70-71	78.00		6.69		55.73				
9H-2, 114-115	78.44	9.84	5.95	3.89	49.56	0.21	2.48	18.8	1.6
9H-4, 70-71	81.00		6.34		52.81				
9H-4, 100-101	81.30	12.52	6.82	5.70	56.81	0.30	1.89	18.9	3.0
9H-5, 42-43	82.22	11.58	6.42	5.16	53.48	0.27	3.31	19.0	1.6
9H-5, 70-71	82.50		6.51		54.23				
9H-6, 20-21	83.50	10.10	6.64	3.46	55.31	0.19	1.18	18.4	2.9
9H-6, 68-69	83.98	18.22	0.72	17.50	6.00	0.87	9.28	20.2	1.9
9H-6, 95-96	84.25		5.60		46.65				
9H-6, 114-115	84.44	12.56	5.79	6.77	48.23	0.33	3.01	20.6	2.3
9H-7, 23-24	85.03	17.05	5.65	11.40	47.06	0.61	3.72	18.7	3.1
9H-CC, 16-17	85.58	12.97	7.10	5.87	59.14	0.30	1.56	19.6	3.8
10H-1, 22-23	85.52	14.97	5.53	9.44	46.06	0.42	3.76	22.7	2.5
10H-1, 64-65	85.94	16.94	3.47	13.47	28.91	0.60	4.98	22.3	2.7
10H-1, 113-114	86.43	14.66	1.98	12.68	16.49	0.63	4.53	20.3	2.8
10H-2, 29-30	87.09	12.98	4.94	8.04	41.15	0.44	4.72	18.3	1.7
10H-2, 79-80	87.59		5.92		49.31				
10H-2, 144-145	88.24	15.87	3.76	12.11	31.32	0.59	2.83	20.7	4.3
10H-4, 80-81	90.60		6.82		56.81				
10H-6, 80-81	93.60		7.10		59.14				
11H-1, 80-81	95.60		6.53		54.39				
11H-3, 79-80	98.59		7.42		61.81				
11H-5, 80-81	101.60		6.29		52.40				
11H-6, 80-81	103.10		6.86		57.14				
12H-3, 60-61	107.90		7.55		62.89				
12H-4, 60-61	109.40		7.82		65.14				
12H-5, 60-61	110.90		8.32		69.31				
13H-1, 61-62	114.41		8.20		68.31				
13H-4, 58-59	118.88		4.66		38.82				
13H-5, 56-57	120.36		10.61		88.38				
13H-6, 34-35	121.64		2.75		22.91				
15X-1, 86-87	129.96		9.66		80.47				
15X-3, 61-62	132.71		11.03		91.88				
16X-1, 69-70	139.39		9.05		75.39				

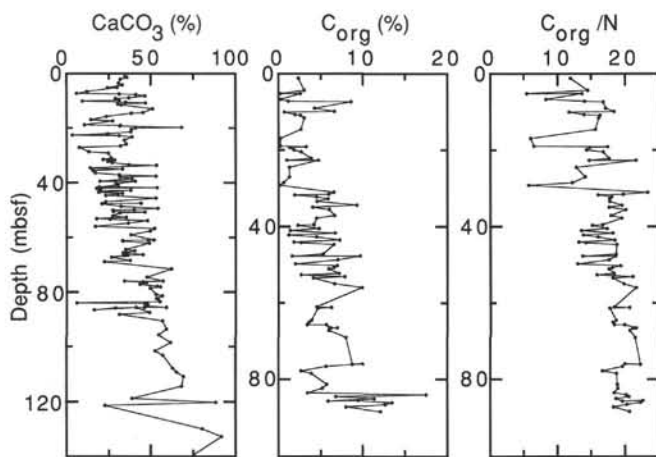


Figure 53. Downhole distribution of calcium carbonate and organic carbon concentrations and the ratio of organic carbon to total nitrogen in sediments from Hole 967A.

terval that could be logged. The maximum logging depth was 598.6 mbsf.

Table 15 summarizes the intervals logged with each tool string. The heave compensator was not working during log acquisition, but the sea was completely calm so that the quality of the logs was not affected. The logs are of fair to good quality, although the caliper measurements indicate borehole washouts (i.e., hole diameter >38 in.) over most of the logged interval (72.9–132, 273–372, 392–442, 450–502, and 532–545 mbsf) (Fig. 63). Bad readings were observed locally by the sonic log at 158–180 mbsf and the PEF at 90–125 mbsf. The sonic log will be reprocessed and some of the Quad combo logs require depth shifting post-cruise. The SFLU log of the induction tool is noisy and contains bad readings.

Two passes of the FMS tool string provided high-resolution resistivity images of the borehole wall as well as measurements of the three vector components of the local magnetic field (GPIT) and the borehole inclination, hole deviation, and diameter in two orthogonal directions. Within the washed-out intervals where the borehole diameter exceeded 38 cm, the FMS pads maintained poor contact with the borehole wall.

A separate run of the GLT logged from 581 to 72.9 mbsf in the open hole and from 72.9 to 0 mbsf through the pipe.

Two runs were made with the GHMT. The total magnetic field intensity did not give good records during the first run, but the second run provided logs of total magnetic field intensity and magnetic susceptibility (Table 15). The data acquired need recalibration and on-shore processing, and we use them here only on a qualitative basis. Total induction and magnetic susceptibility were recorded, by the scalar magnetometer (NMRS) and the susceptometer (SUMS). Total induction shows a shift toward high values because of the highly magnetic BHA at the top of the hole and the drill bit at the bottom.

Results and Preliminary Interpretation

One of the most interesting preliminary results obtained by logging Hole 967E was the detection of a thin interval of evaporites, which was recognized by a characteristic response in the Quad combo logs (see log Unit 2, below) and confirmed by the FMS and geochemical logs. The geochemical data (see “Inorganic Geochemistry” section, this chapter) confirm these results. The stratigraphic position and paleontological data (see “Biostratigraphy and Sedimentation Rates” section, this chapter) suggest that the evaporites were deposited during the Messinian desiccation episode.

On the basis of the log response, we differentiated six logging units in Hole 967E as shown in Figure 64. The boundaries between the units are located at 121, 126, 177, 428, and 510 mbsf. The sharp

changes in log response associated with these boundaries suggest that they correspond to disconformities. This is in general agreement with the interpretation of the lithologic and paleontological data.

Log Unit 1 (72.9–121 mbsf)

Within log Unit 1 three intervals can be differentiated by their level of radioactivity: the interval from 72.9 to 84 mbsf is highly radioactive (i.e., uranium rich) with spikes up to 80 GAPI; 84–100 mbsf is a low-radioactivity interval (<20 GAPI), and 100–121 mbsf has a relatively higher radioactivity (20–25 GAPI). The comparison between the log response and the lithostratigraphy recognized at neighboring holes (see “Lithostratigraphy” section, this chapter) shows that the highly radioactive levels (72.9–84 mbsf) occur within a sapropel-rich interval. Because Hole 967E was drilled without core recovery to a depth of 109.5 mbsf, it is impossible to determine if the uranium-rich intervals correspond to sapropel-rich layers, to the sediments in between, or to both. Post-cruise research on the geochemistry of core samples will determine the relationship between the uranium concentration and the occurrence of sapropels. The natural gamma-ray spectrometry tool (see “Explanatory Notes” chapter, this volume) is not a high-resolution tool and is therefore useful only for analyzing relatively thick intervals.

Fluctuations in density from approximately 1.2 to 2.2 g/cm³ indicate lithologic variation between 72.9 and 102.9 mbsf. According to the lithologic sections recovered in adjacent holes, this corresponds to intercalations of nannofossil-rich sediment and mud turbidites.

The lowermost part of Unit 1 (102–121 mbsf) is a rather massive interval that shows only slight changes in composition according to the log response of lithology indicators (PEF and density). The lithology recognized in cores of this interval indicates that it is nannofossil ooze and micrite.

Log Unit 2 (121–126 mbsf)

Log Unit 2 has an extremely low radioactivity (mostly about 3 GAPI), a typical feature of evaporites as is the high resistivity also observed. The FMS images show this interval as highly resistive (i.e., bright) and massive. Density (about 2.3 g/cm³), PEF (values of about 3), and (preliminary reprocessed) sonic log values indicate that gypsum is the main constituent of this evaporitic unit. In order to evaluate the mineralogy quantitatively and analyze for the possible presence of other evaporitic minerals or interbedded clay, it will be necessary to correct these logs for an enlarged borehole diameter. Toward the base of Unit 2, there is evidence of interbedded clays (higher radioactivity, Th, and U and lower resistivity and density).

Log Unit 3 (126–177 mbsf)

Sharp shifts of the log values at the top and the bottom of log Unit 3 define its boundaries, which were interpreted as disconformities. The condition of the hole in this depth interval, as shown by the caliper, is rather good, in contrast to the units above and below. This reflects contrasts in the sedimentology between this unit and its neighbors. Typical radioactivity values for this unit are in the range of 15 GAPI, although, within the uppermost 10 m, values range between 20 and 25 GAPI. The upper part of the unit also has a lower density that suggests a slight change in composition. A significant feature at 160.5 mbsf (radioactivity spike, change in PEF value) was interpreted as a discontinuity within the unit. According to the lithology recovered, the unit consists of middle Eocene chalk.

Log Unit 4 (177–428 mbsf)

The two principal divisions in log Unit 4 are distinguished above and below 395 mbsf on the basis of a downward change to relatively high acoustic velocity (from under 3.2 km/s to more than 3.3 km/s) and a relatively high uranium to thorium ratio (coincident with an in-

Table 9. Results of Rock-Eval pyrolysis for sediments from Hole 967A.

Core, section, interval (cm)	Depth (mbsf)	S ₁ (mg/g)	S ₂ (mg/g)	S ₃ (mg/g)	TOC (%)	PC	HI	OI	T _{max} (°C)	PI	S ₂ /S ₃
160-967A-											
1H-1, 122-123	1.22	0.74	2.72	5.27	2.38	0.29	114	221	409	0.21	0.52
1H-3, 132-133	4.32	0.85	4.11	5.52	3.04	0.41	135	182	414	0.17	0.74
1H-4, 80-81	5.30	0.69	2.99	4.59	2.58	0.31	116	178	415	0.19	0.65
1H-5, 133-134	7.33	0.18	0.45	3.62	1.12	0.05	40	323	399	0.29	0.12
1H-5, 145-146	7.45	6.68	28.47	7.80	8.59	2.92	331	91	412	0.19	3.65
1H-CC, 8-9	9.13	1.25	9.43	5.53	4.27	0.89	221	130	424	0.12	1.71
2H-1, 64-65	9.94	4.21	22.62	6.85	6.64	2.23	341	103	416	0.16	3.30
2H-1, 145-146	10.75	0.38	1.84	3.93	1.95	0.18	94	202	417	0.17	0.47
2H-2, 17-18	10.97	0.39	1.63	4.04	2.61	0.17	62	155	416	0.19	0.40
2H-2, 84-85	11.64	0.77	4.84	4.85	3.05	0.47	159	159	420	0.14	1.00
2H-4, 88-89	14.68	0.60	3.60	4.63	2.65	0.35	136	175	419	0.14	0.78
3H-1, 35-36	19.15	0.94	6.92	4.44	3.30	0.65	210	135	418	0.12	1.56
3H-1, 49-50	19.29	1.13	7.20	4.61	1.33	0.69	541	347	414	0.14	1.56
3H-1, 127-128	20.07	0.31	0.91	3.95	1.86	0.10	49	212	416	0.25	0.23
3H-2, 20-21	20.50	0.94	5.26	4.26	2.69	0.51	196	158	417	0.15	1.23
3H-3, 35-36	22.15	1.02	7.21	5.17	3.88	0.68	186	133	427	0.12	1.39
3H-3, 86-87	22.66	0.12	0.24	2.46	1.03	0.03	23	239	428	0.33	0.10
3H-3, 95-96	22.75	1.38	12.06	4.95	4.76	1.12	253	104	428	0.10	2.44
3H-4, 122-123	24.52	0.22	0.93	3.18	1.28	0.10	73	248	427	0.19	0.29
3H-6, 82-83	27.12	0.13	0.36	2.22	1.27	0.04	28	175	416	0.27	0.16
4H-2, 129-130	31.09	0.52	3.24	3.91	6.53	0.31	50	60	431	0.14	0.83
4H-3, 34-35	31.64	2.00	18.96	4.95	5.92	1.74	320	84	428	0.10	3.83
4H-3, 48-49	31.78	0.32	1.69	3.35	1.92	0.17	88	174	426	0.16	0.50
4H-3, 93-94	32.23	1.15	8.92	4.73	4.51	0.84	198	105	427	0.11	1.89
4H-3, 140-141	32.70	2.03	15.15	5.36	5.84	1.43	259	92	425	0.12	2.83
4H-4, 62-63	33.42	1.55	11.17	4.73	4.60	1.06	243	103	422	0.12	2.36
4H-5, 20-21	34.50	4.35	29.79	6.78	9.34	2.83	319	73	425	0.13	4.39
4H-5, 70-71	35.00	0.97	8.49	5.17	4.04	0.79	210	128	427	0.10	1.64
4H-5, 130-131	35.60	1.57	18.39	6.23	6.02	1.66	305	103	434	0.08	2.95
4H-6, 136-137	37.16	2.12	18.73	6.87	6.64	1.73	282	103	425	0.10	2.73
4H-7, 52-53	37.82	0.98	8.32	5.35	4.49	0.77	185	119	425	0.11	1.56
5H-2, 12-13	39.42	1.00	8.43	5.44	4.17	0.78	202	130	428	0.11	1.55
5H-2, 32-33	39.62	0.85	4.01	4.67	2.27	0.40	177	206	422	0.17	0.86
5H-2, 115-116	40.45	1.18	11.58	6.09	4.83	1.06	240	126	427	0.09	1.90
5H-3, 87-88	41.67	2.31	21.38	5.46	6.74	1.97	317	81	427	0.10	3.92
5H-4, 42-43	42.72	0.76	7.67	4.93	4.47	0.70	172	110	431	0.09	1.56
5H-4, 122-123	43.52	0.83	8.13	4.68	7.22	0.74	113	65	432	0.09	1.74
5H-5, 85-86	44.65	3.01	22.66	5.24	6.59	2.13	344	80	426	0.12	4.32
5H-7, 36-37	47.16	1.53	14.26	4.69	5.24	1.31	272	90	430	0.10	3.04
6H-1, 40-41	47.70	5.94	35.28	6.79	9.69	3.42	364	70	426	0.14	5.20
6H-1, 138-139	48.68	4.21	25.11	5.85	7.03	2.43	357	83	422	0.14	4.29
6H-2, 142-143	50.22	2.42	25.51	5.81	6.93	2.32	368	84	429	0.09	4.39
6H-3, 36-37	50.66	2.40	22.79	5.82	6.52	2.09	350	89	422	0.10	3.92
6H-3, 75-76	51.05	2.32	22.96	5.72	5.97	2.10	385	96	430	0.09	4.01
6H-4, 37-38	52.17	3.89	30.42	5.81	7.16	2.85	425	81	429	0.11	5.24
6H-4, 128-129	53.08	3.95	33.74	5.71	7.85	3.13	430	73	431	0.10	5.91
6H-5, 18-19	53.48	0.93	12.00	5.07	4.14	1.07	290	122	437	0.07	2.37
6H-6, 9-10	54.89	2.47	25.96	6.30	6.65	2.36	390	95	433	0.09	4.12
6H-6, 112-113	55.92	4.10	39.24	7.42	9.95	3.60	394	75	427	0.09	5.29
7H-3, 116-117	60.96	1.20	16.43	4.98	4.46	1.46	368	112	436	0.07	3.30
7H-3, 130-131	61.10	1.85	23.96	5.35	6.23	2.14	385	86	432	0.07	4.48
7H-4, 5-6	61.35	1.30	15.06	5.18	4.67	1.36	322	111	429	0.08	2.91
7H-6, 21-22	64.51	1.00	12.43	4.12	3.93	1.11	316	105	427	0.07	3.02
7H-6, 74-75	65.04	0.92	10.75	3.90	3.63	0.97	296	107	426	0.08	2.76
7H-6, 130-131	65.60	0.74	10.09	3.69	3.39	0.90	298	109	427	0.07	2.73
7H-6, 135-136	65.65	1.70	21.45	5.06	5.68	1.92	378	89	422	0.07	4.24
7H-CC, 26-27	66.50	2.02	21.00	5.34	6.17	1.91	340	87	418	0.09	3.93
7H-CC, 34-35	66.58	2.46	26.50	5.80	6.98	2.40	380	83	427	0.08	4.57
8H-1, 20-21	66.50	2.29	21.71	5.14	6.05	1.99	359	85	421	0.10	4.22
8H-1, 88-89	67.18	3.20	20.84	4.23	5.97	2.00	349	71	417	0.13	4.93
8H-2, 123-124	69.03	3.70	32.59	5.84	8.02	3.01	406	73	417	0.10	5.58
8H-CC, 10-11	76.10	3.54	28.96	7.22	8.80	2.70	329	82	415	0.11	4.01
9H-1, 9-10	75.89	4.62	39.05	8.16	9.99	3.62	391	82	419	0.11	4.79
9H-1, 71-72	76.51	3.30	20.46	6.19	5.68	1.97	360	109	410	0.14	3.31
9H-2, 51-52	77.81	0.76	6.75	2.79	2.67	0.62	253	104	424	0.10	2.42
9H-2, 114-115	78.44	1.26	12.73	3.19	3.89	1.16	327	82	427	0.09	3.99
9H-4, 100-101	81.30	1.97	19.95	3.86	5.70	1.82	350	68	422	0.09	5.17
9H-5, 42-43	82.22	1.37	18.54	3.40	5.16	1.65	359	66	426	0.07	5.45
9H-6, 20-21	83.50	0.93	10.28	2.80	3.46	0.93	297	81	425	0.08	3.67
9H-6, 68-69	83.98	11.80	64.58	6.28	17.50	6.34	369	36	421	0.15	10.28
9H-6, 114-115	84.44	2.18	25.36	3.94	6.77	2.29	375	58	425	0.08	6.44
9H-7, 23-24	85.03	6.55	43.39	5.50	11.40	4.15	381	48	421	0.13	7.89
9H-CC, 16-17	85.58	3.37	24.00	3.47	5.87	2.27	409	59	419	0.12	6.92
10H-1, 22-23	85.52	5.42	41.20	4.79	9.44	3.87	436	51	422	0.12	8.60
10H-1, 64-65	85.94	7.17	62.10	5.28	13.47	5.75	461	39	429	0.10	11.76
10H-1, 113-114	86.43	5.13	51.57	5.15	12.68	4.71	407	41	428	0.09	10.01
10H-2, 144-145	88.24	4.72	50.94	5.75	12.11	4.62	421	47	426	0.08	8.86

Notes: TOC = total organic carbon; PC = petroleum potential as pyrolyzable carbon; HI = hydrogen index; OI = oxygen index; PI = production index; see the "Explanatory Notes" chapter (this volume) for units for these parameters.

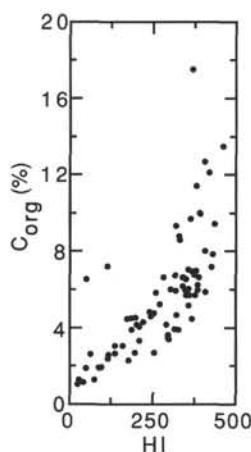


Figure 54. Relationship between organic carbon and the hydrogen index for sediments from Hole 967A.

crease in radioactivity). This probably reflects a change in both composition and texture. A progressive, gradual change from the bottom to the top of this unit is otherwise observed. The change at 395 mbsf may correspond to a change in core lithology, from Upper Cretaceous foraminiferal pelagic chalk to calcarenites with replacement chert below.

In total, seven subunits can be distinguished within Unit 4 on the basis of log response. The boundaries between the subunits are tentatively placed at the following depths: 205, 219, 235, 271, 311, 345, and 396 mbsf. The changes recognized suggest slight variations in composition and texture, which are probably related to facies changes or to different sedimentation episodes. Relative increases in K at 257, 322, and 353 mbsf are probably related to the presence of glauconite (K-rich clay mineral), which was detected in the core. An increase in U at 377 mbsf and within the intervals 384–395, 406–408, 414–415, and 422–426 mbsf seems to be related to pyrite-rich (organic-rich) intervals recognized in some cases at corresponding depths in the cores (see “Lithostratigraphy” section, this chapter). From the bottom to the top of Unit 4, radioactivity progressively decreases. The radioactivity ranges from 45 to 50 GAPI at the bottom of the unit to 10–20 GAPI toward the top of the unit. The progressive increase in PEF values downhole that was also recognized suggests better cementation with depth and compaction of the carbonate-rich sediments. A progressive increase in acoustic velocity from top to bottom seems to be an expression of a compaction trend within the sediments, which is also noticeable in the decreasing porosity shown in the neutron log and a progressive increase in density.

Log Unit 5 (428–510 mbsf)

There is a sharp decrease in radioactivity at the top of log Unit 5, from 48 GAPI at the bottom of Unit 4 to values ranging between 20 and 25 GAPI within Unit 5. Two subunits were identified: Subunit 5A (428–458 mbsf) and Subunit 5B (458–510 mbsf). Both log Unit 5 and its subunits can be correlated with lithostratigraphic Unit IV (see “Lithostratigraphy” section, this chapter); the two facies correspond to a corallgal calcarenite subunit and a well-cemented shallow-water calcarenite subunit. The depth boundaries determined from the cores correlate with those seen in the logs. A remarkable feature is the lower density and PEF values within Subunit 5B, which do not seem to be related to the geology or to the physical properties of the rock, but rather to hole conditions. A large washout zone at this level probably affected the density tool readings, which are highly sensitive to the borehole diameter. The possibility that this feature is related to the presence of gas can be discounted because the neutron log shows an

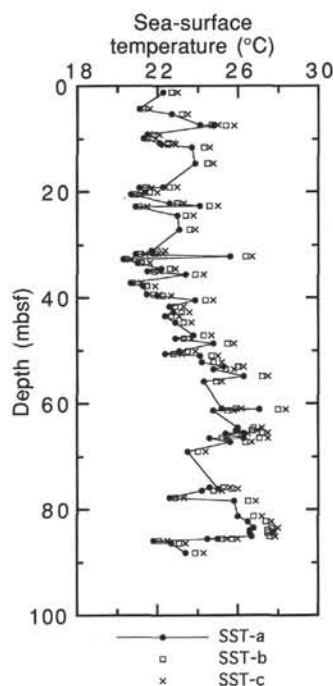


Figure 55. Variation of paleo-sea-surface temperatures (SST) during times of sapropel deposition as a function of depth in Hole 967A. Temperatures were calculated from the alkenone unsaturation index (U_{37}^k) according to the calibrations of (a) Sikes and Volkman (1993), (b) Prahl and Wakeham (1987), and (c) Brassell (1993).

increase in porosity values, which would not be expected in the presence of gas.

Log Unit 6 (510–598.6 mbsf)

The top of log Unit 6 is recognizable by a sharp increase in radioactivity that also shows on the PEF, density, and resistivity logs. This can be correlated with the lithostratigraphic facies and unit boundary between lithostratigraphic Unit IV and Unit V (see “Lithostratigraphy” section, this chapter). In spite of the poor core recovery, this unit was recognized as a limestone breccia. The log response and facies observed in the FMS images agree with this, but also indicate interlayering of intervals with higher and lower resistivity. The resistivity logs suggest a high porosity, which is not reflected on the neutron porosity log, that was interpreted as fracture porosity. The FMS images indicate the same features. The radioactivity is rather high in the entire unit, varying from 20 to 50 GAPI. A remarkable feature is the presence of extremely high PEF spikes (from 12 up to 30 barnes/e⁻) that suggest the presence of thin intercalations or veins of minerals other than the host rock that might be sealing fractures. The PEF and density values are close to those of some oxides and sulfides and the raw geochemical logs indicate an increase in silica content at the same depth.

Geochemical Logging Results

The GLT combination was run successfully in Hole 967E. This logging string is composed of the NGT, AACT, and GST (see “Explanatory Notes” chapter, this volume). The absolute abundances of thorium (ppm), uranium (ppm), potassium (wt%), and aluminum (wt%) are determined from NGT- and AACT-measured spectra. From the GST measurements, the linear combination of the elemen-

Table 10. Index properties measured in APC and XCB cores from Hole 967A and RCB cores from Hole 967E.

Core, section, interval (cm)	Depth (mbsf)	Water content (wt%)	Porosity (vol%)	Bulk density (g/cm ³)		Grain density (g/cm ³)		Dry density (g/cm ³)	
				Method B	Method C	Method B	Method C	Method B	Method C
160-967A-									
1H-1, 93-95	0.93	56.06	79.99	1.46	1.42	3.21	2.82	0.64	0.62
1H-3, 121-123	4.21	44.75	69.24	1.59	1.56	2.85	2.71	0.88	0.86
1H-5, 119-121	7.19	52.48	75.87	1.48	1.44	2.92	2.64	0.70	0.69
1H-6, 81-83	8.31	40.77	66.42	1.67	1.62	2.94	2.72	0.99	0.96
1H-7, 11-13	8.61	45.62	71.18	1.60	1.54	3.02	2.65	0.87	0.84
2H-1, 90-92	10.2	38.98	64.00	1.68	1.65	2.85	2.72	1.03	1.01
2H-2, 136-138	12.16	40.51	65.88	1.67	1.61	2.90	2.62	0.99	0.96
2H-3, 141-143	13.71	38.63	59.63	1.58	0.00	2.40	0.00	0.97	0.00
2H-4, 132-134	15.12	37.11	61.16	1.69	1.68	2.73	2.70	1.06	1.06
2H-5, 134-136	16.64	40.66	65.36	1.65	1.61	2.82	2.64	0.98	0.95

Only part of this table is reproduced here. The entire table appears on the CD-ROM (back pocket).

Table 11. Compressional wave velocity measured in APC and XCB cores from Hole 967A and RCB cores from Hole 967E.

Core, section, interval (cm)	Depth (mbsf)	Measurement type	Velocity (km/s)
160-967A-			
1H-2, 133.1	2.83	DSV 1	1.53
1H-2, 133.5	2.84	DSV 2	1.52
1H-3, 121.2	4.21	DSV 1	1.52
1H-3, 122.4	4.22	DSV 2	1.53
1H-4, 61.7	5.12	DSV 1	1.51
1H-4, 64.3	5.14	DSV 2	1.50
1H-5, 119.7	7.20	DSV 2	1.50
1H-5, 120.2	7.20	DSV 1	1.50
1H-6, 81.6	8.32	DSV 1	1.54
1H-6, 82	8.32	DSV 2	1.55

Note: Direct DSV measurements.

Only part of this table is reproduced here. The entire table appears on the CD-ROM (back pocket).

Table 12. Vane shear strength measured in split APC cores from Hole 967A.

Core, section, interval (cm)	Depth (mbsf)	Strength (kPa)
160-967A-		
1H-2, 139.1	2.89	6.9
1H-3, 120	4.20	9.4
1H-4, 60.4	5.10	12.7
1H-5, 121.2	7.21	17.4
1H-6, 82.6	8.33	17.9
2H-1, 88.4	10.18	17.3
2H-2, 201.4	12.81	16.1
2H-3, 194.3	14.24	17.9
2H-4, 194.4	15.74	18.5
2H-5, 189.7	17.20	18.7

Only part of this table is reproduced here. The entire table appears on the CD-ROM (back pocket).

tal standards that best fit the accumulated spectra is determined. This leads to the elemental yield coefficients, which are the proportions of the total spectrum attributed to each element. The GLT can measure the contribution of calcium, silica, iron, hydrogen, chlorine, and sulfur to the spectrum. Certain elemental yield ratios, which are used to measure changes in the macroscopic properties of the formation, are also calculated during downhole acquisition (Table 16).

Because the yields are normalized to 1 and, hence, are dependent on each other, it is impossible to discuss them in terms of elemental abundances. However, the elemental yield ratios can be used to interpret the logs qualitatively.

Table 13. Thermal conductivity measured in APC and XCB cores from Hole 967A and RCB cores from Hole 967E.

Core, section, interval (cm)	Depth (mbsf)	Thermal conductivity (W/[m · K])
160-967A-		
1H-1, 50	0.50	0.99
1H-2, 50	2.00	1.17
1H-3, 50	3.50	1.13
1H-4, 50	5.00	1.10
1H-5, 50	6.50	0.98
1H-6, 50	8.00	1.19
1H-7, 50	9.00	1.18
2H-1, 50	9.80	1.07
2H-2, 50	11.30	1.07
2H-3, 50	12.80	1.29

Only part of this table is reproduced here. The entire table appears on the CD-ROM (back pocket).

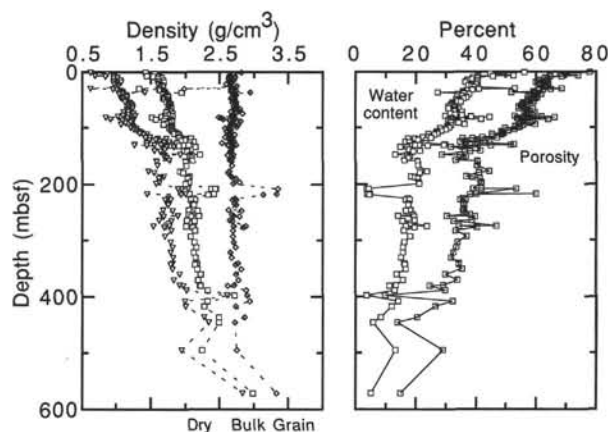


Figure 56. Index properties measured in cores from Holes 967A and 967E. Density was measured using method C (see "Explanatory Notes" chapter, this volume).

Correlation with Lithology

The boundary between lithostratigraphic Units III and IV (see "Lithostratigraphy" section, this chapter) can be clearly seen at 420 mbsf on the porosity-indicator ratio (PIR = H/[Si + Ca]; Table 16), which is the water content relative to silica and calcium, and on the salinity-indicator ratio (SIR = Cl/H; Table 16). A decrease in both the PIR and SIR profiles at 420 mbsf indicates a denser formation,

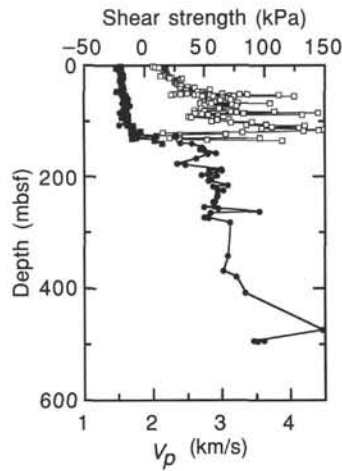


Figure 57. P -wave velocity measured in cores from Holes 967A and 967E and shear vane strength measured in split APC cores from Hole 967A. DSV 1 and DSV 3 (vertical) = solid circles; DSV 2 (horizontal) = solid squares; shear strength = open squares.

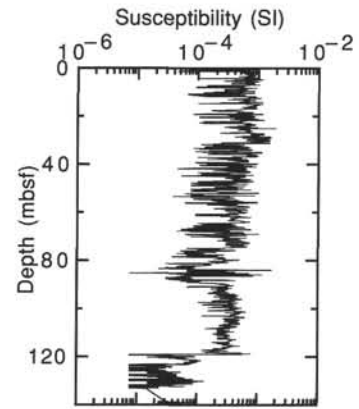


Figure 60. Magnetic susceptibility measured on the MST from cores from Hole 967A.

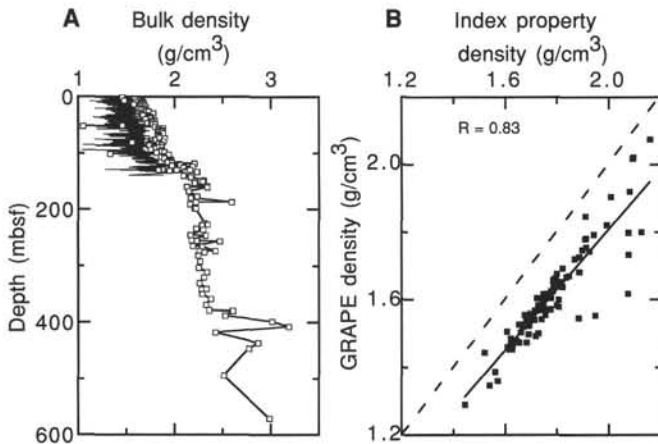


Figure 58. **A.** Density measured as part of index properties measurements (connected open symbols) and GRAPE density (line) measured using the MST. **B.** Linear regression of index properties density with GRAPE density at common depths. The dashed line represents a hypothetical one-to-one correspondence between the two density data sets.

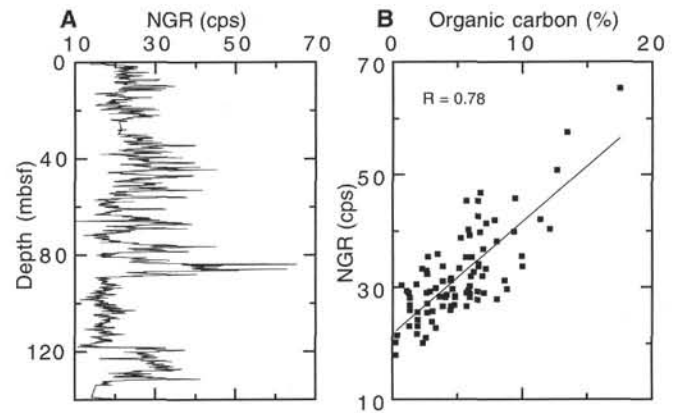


Figure 61. **A.** Natural gamma-ray radiation measured in cores from Hole 967A. **B.** Correlation of NGR with the organic carbon content in the sediments.

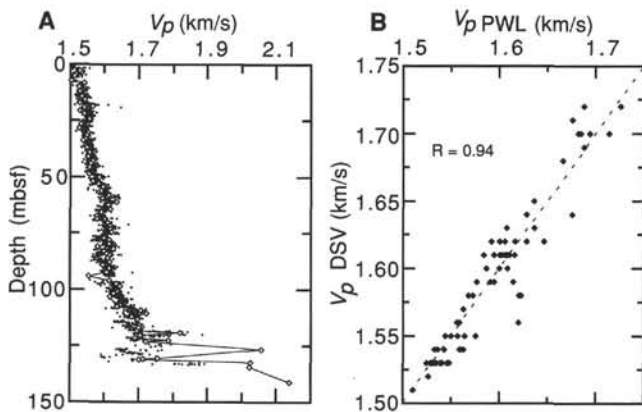


Figure 59. **A.** P -wave velocities measured using the PWL component of the MST compared with velocities measured in discrete samples using the DSV apparatus (connected open symbols). **B.** Correlation of PWL velocity with DSV velocity at common depths.

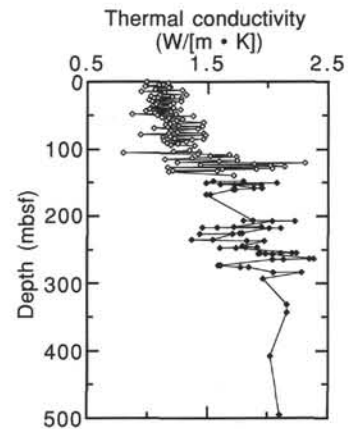


Figure 62. Thermal conductivity measured in cores from Holes 967A and 967E.

Table 14. Correlation between physical properties and lithostratigraphy at Hole 967A.

Interval (mbsf)	GRAPE density	NGR	Susceptibility	V_p	Lithostratigraphy
0–60	Steady increase	Constant, large scatter	Decrease	Steady increase	Holocene-Pleistocene ooze and sapropels
60–70	Constant	Large variation	Constant	Constant	Debris flow
70–90	Large variation	High values	Low values	Constant	Pliocene ooze and sapropels
90–120	Steady increase	Constant, low scatter	Constant	Steady increase	Pliocene ooze and sapropels
120–135	Abrupt increase, steady decrease	Abrupt increase, constant	Abrupt decrease	Abrupt increase, large variation	Calcareous fragments embedded in sediment; reworked Eocene-Miocene fossils

Table 15. Logged depth intervals in Hole 967E for the three tool strings.

String	Run	Open-hole depth		In-pipe depth		Tools
		(mbsf)	(mbrf)	(mbsf)	(mbrf)	
Quad combination	Downhole	91.4–598.6	2655.4–3162.6	0–91.4	2564–2655.4	NGT/SDT/CNT/HLDT/DIT/TLT
	Up 1 (repeat section)	598.6–516	3162.6–3080			
	Up 2	598.6–71.6	3162.6–2635.6	71.6–52	2635.6–2616	
GLT	Up 1	581.4–71.6	3145.4–2635.6	71.6–13.3	2635.6–2550.72	NGT/CNT/AACT/GST
	Up 2 (repeat section)	123.3–71.6	2687.3–2635.6	71.6–67	2635.6–2631.03	
FMS	Up 1	582.3–71.6	3146.3–2635.6	71.6–53.3	2635.6–2617.3	NGT/GPIT/FMS
	Up 2	582.4–71.6	3148.4–2635.6	71.6–63.2	2635.6–2627.2	
GHMT	Up 1	583.7–88.8	3147.7–2652.8			NGT/GHMT
	Up 2 (repeat section)	526.4–416.6	3090.4–2980.9			

whereas the lithology-indicator ratio ($LIR = Si/[Si + Ca]$; Table 16) shows a pronounced decrease in silica content that correlates with the passage to a more carbonate-rich lithology (Fig. 65).

Lithostratigraphic Unit V at 510 mbsf is characterized by slight decrease of the PIR profile and the occurrence of several spikes in the LIR profile, which can be related to some chert layers described in the cores (Fig. 66).

The aluminum and potassium contents show relatively high values in some intervals of lithostratigraphic Units I and II (40–60 and 90–110 mbsf; Fig. 64). These values can be interpreted as clay-rich subunits related to the mud turbidite intervals found in the cores. In the same manner, several spikes on the aluminum profile (at 140, 180, 370, and 390 mbsf) and on the potassium profile (at 140, 180, 260, and 390 mbsf) may indicate several discrete turbidite or clay-rich layers, which were not recognized in the cores because of poor core recovery.

Indications for the Presence of Gypsum

The S/Ca ratio (Fig. 66) shows a value of 1 between 124 and 128 mbsf; this corresponds to a gypsum layer that was not recovered on the cores, but was indicated by the depth profiles for calcium, sulfate, and strontium from pore-water analyses (see “Inorganic Geochemistry” section, this chapter). The SIR (Fig. 66) also clearly shows a decrease at the same depth owing to this highly hydrated layer. Taking the resolution of the tool (about 1.5 m) into account, the gypsum layer can be estimated to be 4 to 5 m thick, which is consistent with results from the FMS and other conventional logging data.

The profiles of the aluminum, thorium, and uranium contents (Fig. 67) suggest the presence of clayey layers above and below the gypsum layer as indicated by higher aluminum and potassium contents (Fig. 67). Such clay layers are typically associated with gypsum formed in situ, which is suggested by the sharpness of the SIR, PIR, and S/Ca ratio spikes.

The elemental weight percent oxides will be obtained from on-shore processing of the data. The mineralogical inversion uses a statistical modeling based on clustering the elemental data into several groups. This information is used to infer a possible mineralogy that corresponds to different general types of rocks. In order to discriminate between various similar lithologies, we can integrate the conventional logging data in the analysis, and use the results from the

FMS and the geological data. Such a study should help to define the exact mineralogical and chemical nature of the different lithologies inferred from the logs.

Temperature Logging Tool

The Lamont-Doherty TLT recorded temperature measurements in Hole 967E during both runs 1 and 2. Unfortunately, the data from run 1 were corrupted owing to damaged tool electronics. Only the data from run 2 are presented here. The temperature was recorded downhole and uphole. The fast- and the slow-thermistors show a constant offset of about 0.3°C.

Figure 68 shows the fast- and the slow-thermistors temperatures for both downhole and uphole. Despite the fact that the borehole temperature was still equilibrating, the large difference between the up and downhole profiles below 450 mbsf is a result of the drilling disturbance. Both curves show a change in gradient at about 350 mbsf, which is discussed in terms of heat-flow variations (see “Heat-flow Measurements” section, “Site 967” chapter, this volume). The bottom-hole temperature is higher than 22°C.

The fast-thermistors curve for the downhole run shows great fluctuations, especially in the upper part. Table 17 shows the depths at which these variations occur. These peaks can be attributed to water flowing into the borehole and warming it; they were not visible on the uphole run because the water column had been mixed. This water flow may have resulted from the forced circulation related to drilling and would indicate zones of relatively high porosity. No evidence from comparison with the other logs has been found, however, to confirm this hypothesis. These anomalies can not be definitely linked to changes in the surrounding rock properties either. The temperature data need to be reprocessed, taking into account the timing of the last circulation in the hole, speed of the tool, and tension in the cable, in order to obtain a more accurate and detailed interpretation.

SUMMARY AND CONCLUSIONS

Site 967 is located on a small ridge near the foot of the northern slope of the Eratosthenes Seamount. The ridge was interpreted to be a compressional feature related to thrusting beneath the Cyprus active margin to the north. Drilling results are consistent with this hypothe-

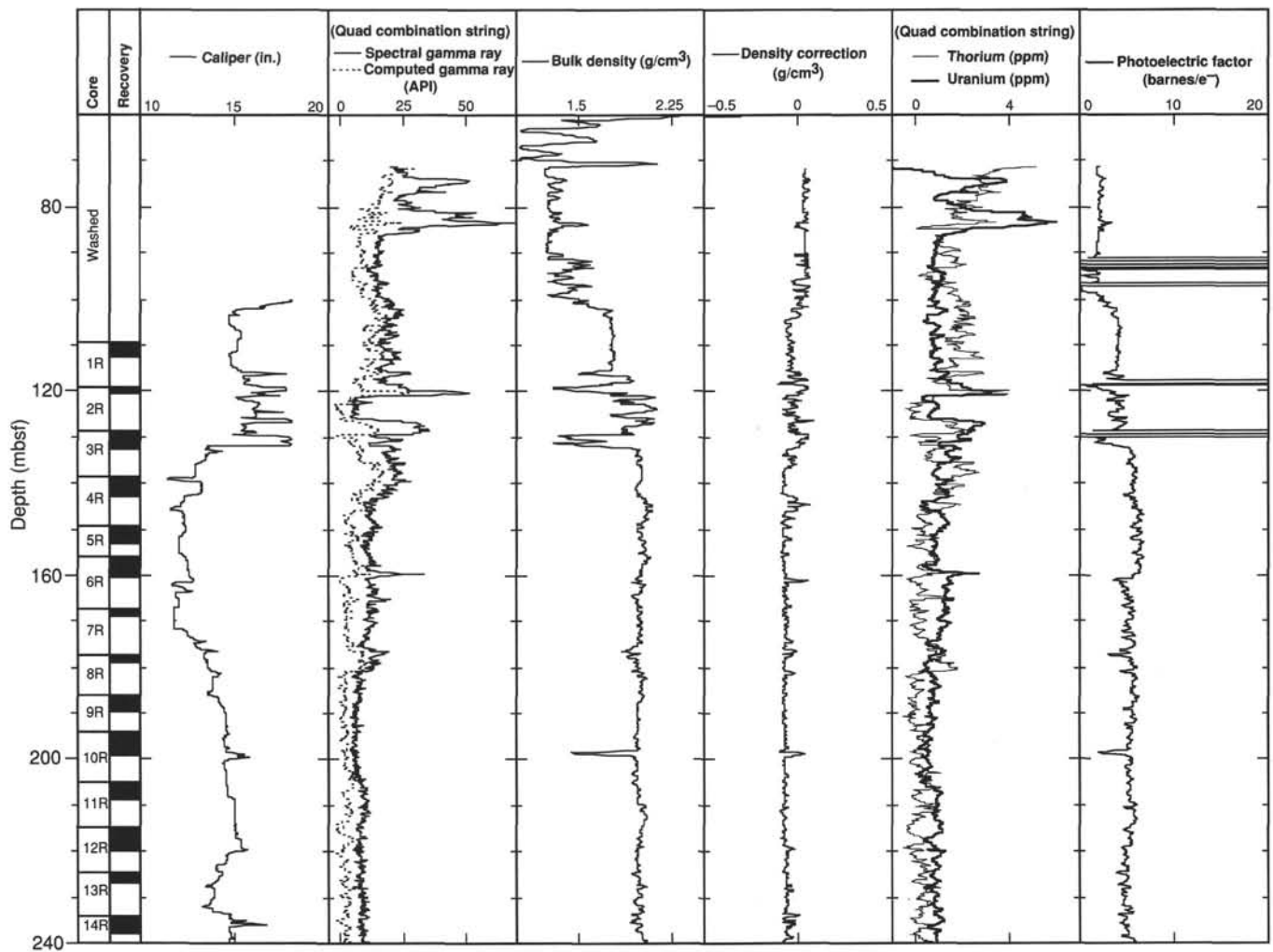


Figure 63. Hole 967E Quad combination tool and FMS (4-arm) caliper results.

sis; coring at Site 967 further provided a Pliocene-Pleistocene sapropel record and a remarkable window into the history of the Mediterranean Sea at least as far back as the Late Cretaceous.

Five lithostratigraphic units were recognized in the sequence recovered from five APC holes and a single RCB hole cored at Site 967.

Unit I (100 m thick) is composed of intercalations of bioturbated nannofossil ooze, nannofossil clay, mud turbidites, and sapropels. An interval of slumping with an overlying debris-flow unit (1–7 m thick) was noted in most holes between 50 and 60 mbsf. Bedding of the host sediment is horizontal to subhorizontal throughout and is cut by sporadic high-angle faults. Eighty discrete sapropels were identified, in which organic carbon values typically range from 3% to 10% (maximum 17%). Many of the sapropels are finely laminated; in the upper three cores, some occur with intercalated mud turbidites. The C/N ratios of the organic matter are relatively high (about 20); hydrogen indices of the organic matter are relatively low (200 to 400) and are positively correlated with organic carbon concentrations. The source of the organic matter may be dominantly marine, but the material appears to be degraded. Optical microscopy shows that fine plant material can be seen in some sapropels, whereas in others the organic matter is present as amorphous matter and dark brown aggregates. Estimates of paleo-sea-surface temperatures based on alkenone indices indicate cyclic variations in the Pleistocene between 21° and

25°C and average temperatures that are 2°–3°C higher in the Pliocene, but with less pronounced fluctuations.

Sediment sequences recovered from the five APC holes were correlated by means of continuously logged physical properties, color, and sedimentological features, from which a composite section was constructed. Over several intervals in the Pliocene, the pattern of sapropel occurrence and the lithologic and physical properties resemble those found at Site 966 on the top of Eratosthenes Seamount. Comparisons of the depositional history of the sites of greatly different water depths will be a high-priority objective of post-cruise work.

Paleontological studies recognized 15 datum levels within the Pleistocene and Pliocene and include the lowermost Pliocene Zones MNN12 and MPL1. A possible hiatus was identified from 1.50 to 2.0 Ma in Hole 967A (but not in Hole 967C), which coincides with the debris flow and slump. The average sedimentation rate over the entire Unit I is 26 m/m.y., ranging from 5 to 57 m/m.y. Preliminary study of benthic foraminifers indicates forms typical of middle mesobathyal depths (i.e., 1800–2500 m) in the upper Pliocene, which give way to an assemblage of possibly lower mesobathyal (2500–3000 m) character, indicative of somewhat deeper water, in the Pleistocene.

The paleomagnetic measurements reveal a complex directional signature that is not easily reconciled with standard paleomagnetic reversal stratigraphy. However, several polarity zones were recognized by measuring discrete samples, and these zones compare well

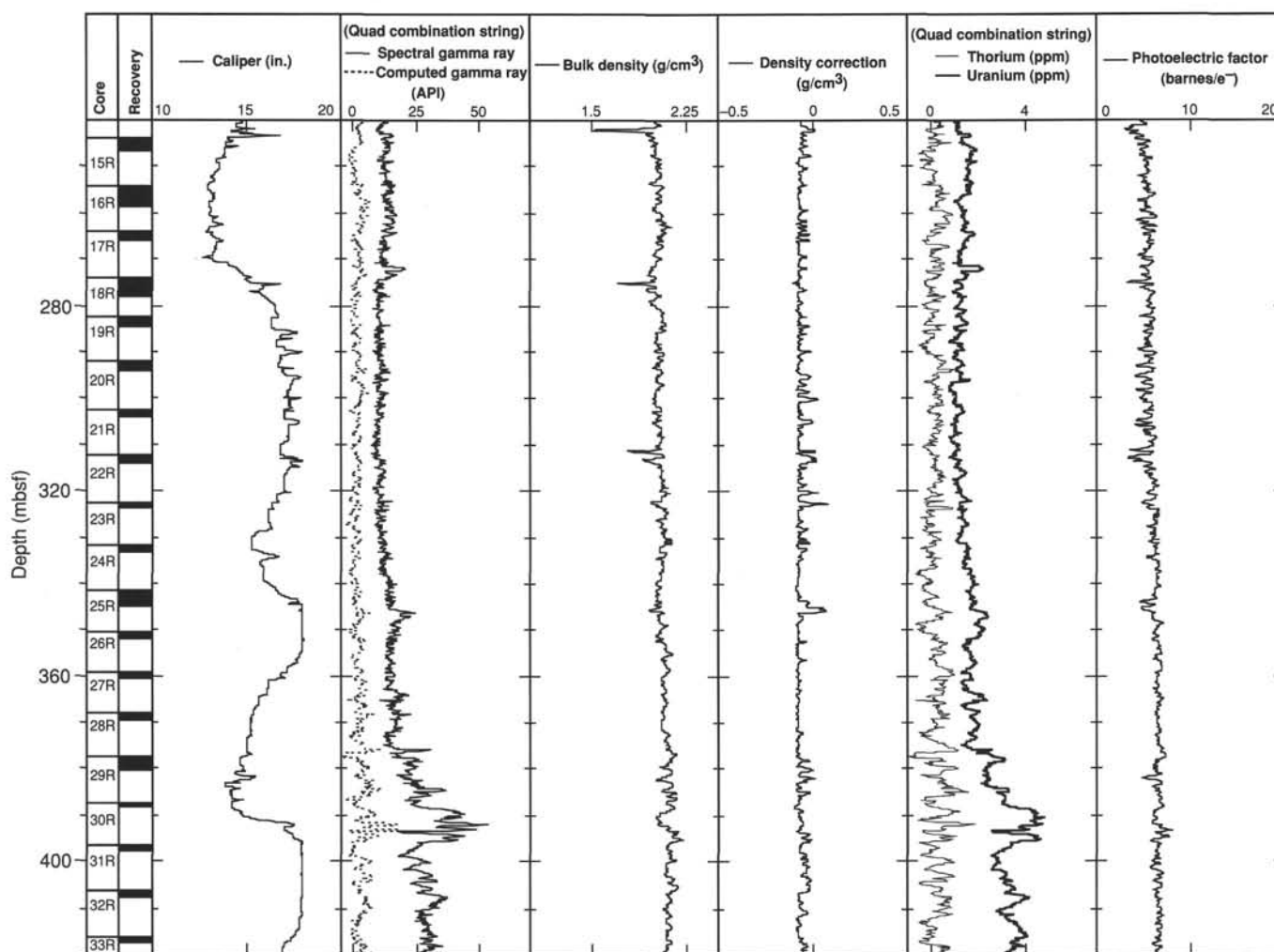


Figure 63 (continued).

with the biostratigraphic data. Problems with the paleomagnetic measurements arise from magnetic mineral diagenesis and magnetic overprinting of sequences that contain abundant sapropels and where organic matter degradation results in redox changes during burial. It appears that strong gradients in magnetic intensity (over 3 orders of magnitude on a scale of centimeters) between the sapropels and the surrounding sediments are introducing artifacts that cannot be resolved with the shipboard cryogenic magnetometer.

Unit II (approximately 10–20 m thick) consists of intercalations of well-consolidated red-colored nannofossil mud and nannofossil ooze, with both micritic and recrystallized carbonate rock fragments. A mixed microfossil assemblage noted at approximately 130 mbsf in Holes 967A and 967E includes reworked planktonic foraminifers and nannofossils of middle Eocene, Oligocene, Miocene, and late Miocene–early Pliocene age. Pore-water calcium, sulfate, and strontium data indicate the presence of gypsum at about 120–130 mbsf. Trends of soluble potassium and rubidium are indicative of uptake by clay minerals. Preliminary analysis of FMS and other log data reveal the presence of a highly resistive interval from 120 to 124 mbsf that is thought to be gypsum. Heat-flow measurements indicate increased values at the boundary with Unit I that may result from the upward flow of relatively warm water through limestones at depth possibly along fault conduits; flow was then constrained by the relatively impermeable Pliocene–Pleistocene clay-rich sediments above.

Unit III (approximately 300 m thick) is composed of well-lithified bioturbated nannofossil chalk, with several thin (tens of centimeters) intervals of dark organic-matter-rich, laminated calcilutite. Glauconite, pyrite, mollusk shells, and replacement chert concretions were also noted. Deformation structures include both a small (centimeter offsets) relatively shallow-dipping suite of normal and reverse faults and a pervasive fabric of steeply dipping normal faults with slickensided fault planes. Paleontological studies indicate that the upper part of Unit III is middle Eocene in age, whereas the lower part is Late Cretaceous (late Santonian–late Maastrichtian), based on well-preserved planktonic foraminifers (*A. mayaroensis*–*D. asymmetricus* Zones) and less well-preserved calcareous nannofossils (NC23 to CC15?). The Cretaceous/Tertiary transition is estimated to lie at approximately 170 mbsf, and although it was probably not recovered, it appears to have some expression in the log data. The FMS and other log data allow the Eocene and Cretaceous pelagic intervals to be distinguished (together with subunits) and also reveal bands of highly resistive material in the Eocene succession, inferred to be chert. The FMS data indicate a large number of deformed intervals of both low and high angle, which were interpreted as representing several generations of faulting, within which marked conductivity variations are indicative of rheology contrasts (e.g., open vs. cemented fault zones).

Unit IV (approximately 80 m thick) consists of well-cemented shallow-water limestone (calcarenes), with calcareous algae, shell

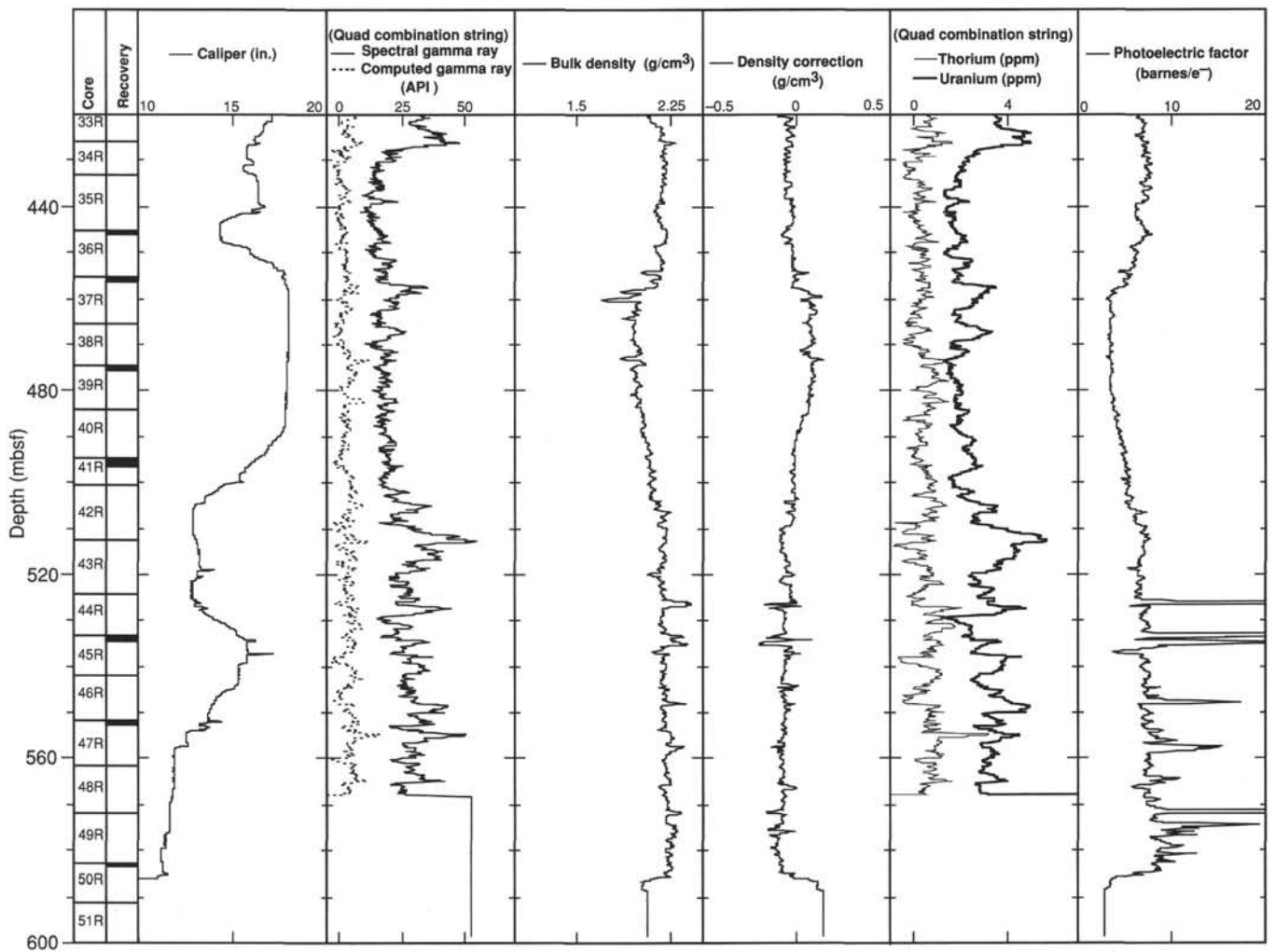


Figure 63 (continued).

fragments, and peloids. Recrystallization and secondary porosity development have destroyed much of the depositional fabric, except within sporadic chert nodules. Fossils have not been identified. The limestone is fractured, with an interstitial brown clay-bearing matrix and a finely crystalline carbonate cement. Both calcite and chalcedonic quartz occur as vein fill.

Unit V (approximately 85 m thick) is restricted to the recovery of a small number of clasts of calcarenite, calcilitite, and breccia that are cut by well-developed slickensides. Individual clasts show a gradation from massive to pervasively brecciated and are composed mainly of angular clasts, which show evidence of shearing, pressure solution, and several generations of cement (i.e., carbonate, then chalcedonic quartz). The FMS and other log data reveal evidence of a breccia-like tectonic fabric, in addition to other features (e.g., bedding).

In summary, Site 967 exhibits a long and diverse geologic history. The site once formed part of a shallow-water carbonate platform, such as that exposed on land around the Mediterranean Sea. The platform was later inundated, ushering in a 40-m.y. period of deep-water pelagic carbonate deposition, punctuated by low-oxygen episodes in the Late Cretaceous and times of high-silica accumulation both in the Late Cretaceous and in the middle Eocene (represented by chert). The earliest Pliocene was the next time interval that is definitely recorded at Site 967. However, the presence of derived microfossils of middle Eocene, Oligocene, Miocene, and late Miocene–early Pliocene age

shows that some open-marine sedimentation took place at, or in the vicinity of, Site 967 during the intervening middle Eocene–early Pliocene time interval. Sediments of this time interval may have been deposited and then eroded, perhaps in response to tectonic uplift. Evaporites apparently accumulated in the late Miocene (i.e., Messinian). This was followed by the erosion of carbonate clasts and deposition of well-oxidized muds and carbonates, largely by turbidity currents in an open-marine setting, which was followed by open-marine sedimentation and sapropel deposition. Water depths may have increased after the late Pliocene in response to dominantly tectonic subsidence, which allowed the accumulation of deep-sea nannofossil-rich sediments interspersed with sapropels and fine-grained mud turbidites.

Interpretation of the site-survey seismic data supports the interpretation of Site 967 as a dominantly south-verging thrust structure. In addition, trends in pore-water chloride concentration indicate the presence of a brine at depth that can be explained by the presence of the overthrust Messinian evaporite beneath. However, the shipboard structural data indicate one or more phases of extensional rather than compressional faulting. The site may have experienced mainly extensional deformation prior to the late Pliocene, followed by reverse faulting and minor uplift that formed the present raised ridge in a compressional setting at the base of the Eratosthenes Seamount slope (i.e., a form of basin inversion). This uplift possibly began in the late Pliocene–early Pleistocene at the time of the inferred depositional hi-

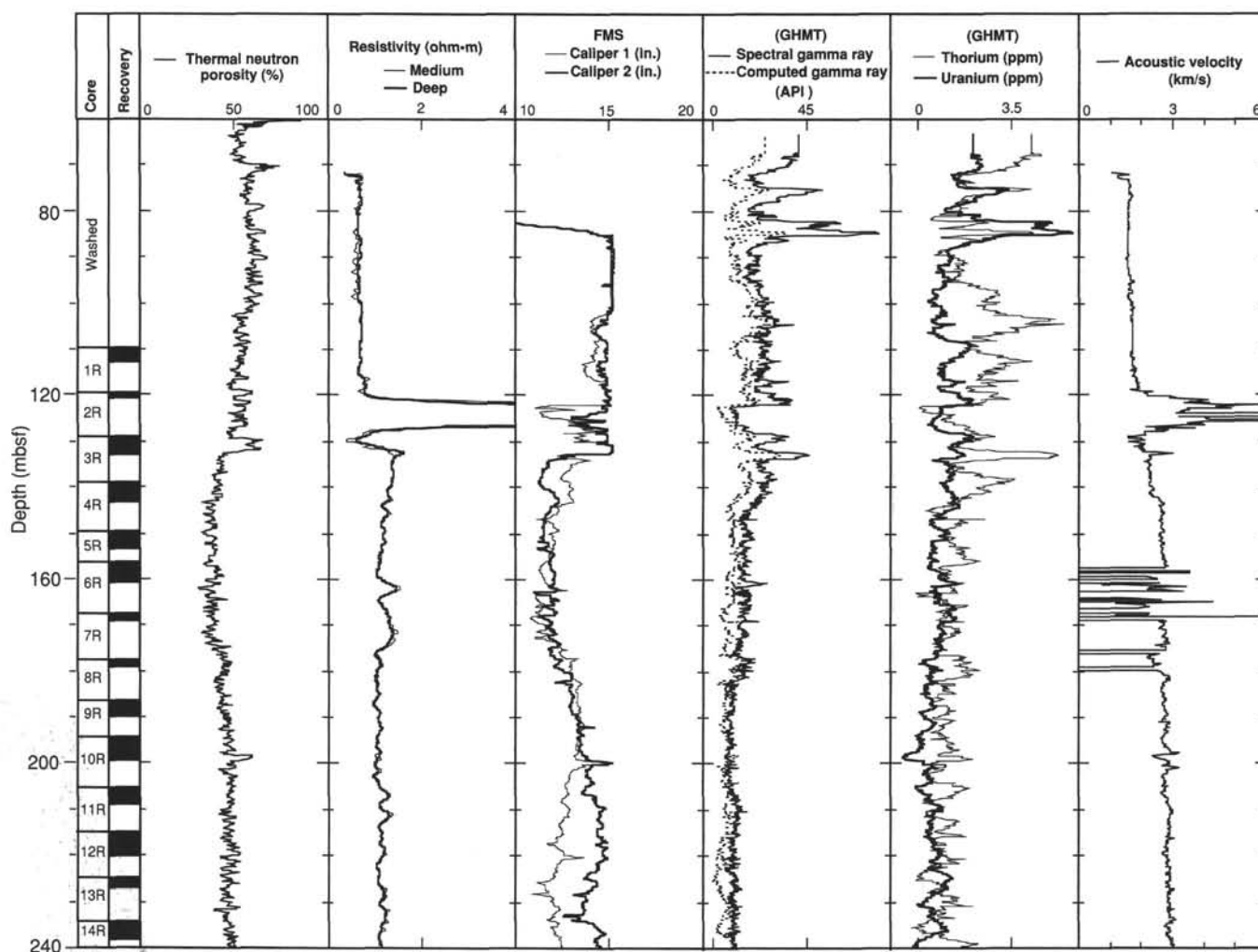


Figure 63 (continued).

atus and slumping in some of the holes. If correct, this interpretation highlights the long-lived nature of faults in the Eratosthenes Seamount.

In conclusion, drilling at Site 967 has charted the kinematic history of a collision-related structure and provided an extraordinary window into the Late Mesozoic history of the Eratosthenes Seamount.

REFERENCES

- Alibes, B., Campo, M., Fraile, J., Galindo-Zaldívar, J., Fomenko, V., and Nieto, L., 1994. Sidescan sonar survey, OKEAN sonographs. In Limonov, A.F., Woodside, J.M., and Ivanov, M.K. (Eds.), *Mud Volcanism in the Mediterranean and Black Seas and Shallow Structure of the Eratosthenes Seamount*. UNESCO Rep. Mar. Sci., 64:128-134.
- Behrmann, J.H., Lewis, S.D., Musgrave, R.J., et al., 1992. *Proc. ODP, Init. Repts.*, 141: College Station, TX (Ocean Drilling Program).
- Blow, W.H., 1979. *The Cainozoic Globigerinida*: Leiden (E.J. Brill).
- Brassell, S.C., 1993. Applications of biomarkers for delineating marine paleoclimatic fluctuations during the Pleistocene. In Engel, M.H., and Macko, S.A. (Eds.), *Organic Geochemistry: Principles and Applications*: New York (Plenum), 699-738.
- Brumsack, H.-J., Zuleger, E., Gohn, E., and Murray, R.W., 1992. Stable and radiogenic isotopes in pore waters from Leg 127, Japan Sea. In Pisciotto, K.A., Ingle, J.C., Jr., von Breyman, M.T., Barron, J., et al., *Proc. ODP, Sci. Results*, 127/128 (Pt. 1): College Station, TX (Ocean Drilling Program), 635-650.
- Caron, M., 1985. Cretaceous planktonic foraminifera. In Bolli, H.M., Saunders, J.B., and Perch-Nielsen, K. (Eds.), *Plankton Stratigraphy*: Cambridge (Cambridge Univ. Press), 17-86.
- Cita, M.B., 1975. Planktonic foraminiferal biozonation of the Mediterranean Pliocene deep-sea record: a revision. *Riv. Ital. Paleontol. Stratigr.*, 81:527-544.
- Cita, M.B., Beghi, C., Camerlenghi, A., Kastens, K.A., McCoy, F., Nosetto, A., Parisi, E., Scolari, F., and Tomadin, L., 1984. Turbidites and megaturbidites from the Herodotus abyssal plain (Eastern Mediterranean) unrelated to seismic events. *Mar. Geol.*, 55:47-62.
- de Lange, G.J., Boelrijk, N.A.I.M., Catalano, G., Corselli, C., Klinkhammer, G.P., Middelburg, J.J., Muller, D.W., Ullman, W.J., Van Gaans, P., and Woitiez, J.R.W., 1990. Sulphate-related equilibria in the hypersaline brines of the Tyro and Bannock Basins, eastern Mediterranean. *Mar. Chem.*, 31:89-112.
- Erba, E., Premoli Silva, I., Wilson, P., Pringle, M.S., Silter, W.V., Watkins, D.K., Arnaud Vanneau, A., Bralower, T.I., Budd, A.F., Camoin, G.F., Masse, J.-P., Mutterlose, J., and Sager, W.V., in press. Synthesis of stratigraphies from shallow-water sequence at Sites 871 through 879 in the Western Pacific Ocean (Leg 44). In Haggerty, J.A., Premoli Silva, I., Rack, F., and McNutt, M. (Eds.), *Proc. ODP, Sci Results*, 144: College Station, TX (Ocean Drilling Program).

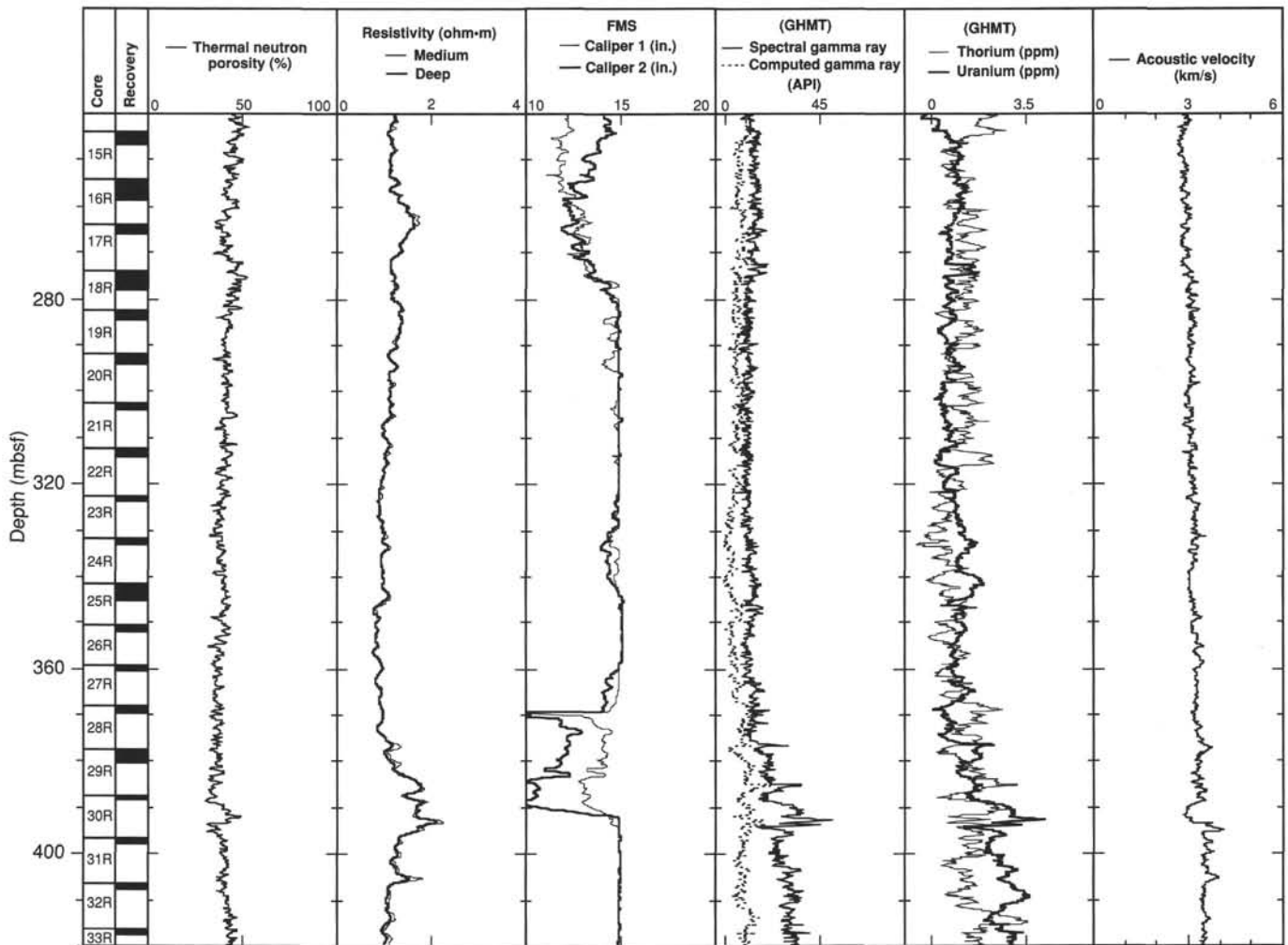


Figure 63 (continued).

- Iaccarino, S., 1985. Mediterranean Miocene and Pliocene planktic foraminifera. In Bolli, H.M., Saunders, J.B., and Perch-Nielsen, K. (Eds.), *Plankton Stratigraphy*: Cambridge (Cambridge Univ. Press), 283–314.
- Limonov, A., and Woodside, J., 1994. Results 4.2.1a. Seismic reflection profiling. In Limonov, A.F., Woodside, J.M., and Ivanov, M.K. (Eds.), *Mud Volcanism in the Mediterranean and Black Seas and Shallow Structure of the Eratosthenes Seamount*. UNESCO Rep. Mar. Sci., 64:120–127.
- Limonov, A.F., Woodside, J.M., and Ivanov, M.K. (Eds.), 1994. *Mud Volcanism in the Mediterranean and Black Seas and Shallow Structure of the Eratosthenes Seamount*. Initial Results of the Geological and Geophysical Investigations during the Third "Training-through-Research" Cruise of the *R/V Gelendzhik* (June–July 1993). UNESCO Rep. Mar. Sci., 64.
- Lindsley-Griffin, N., Kemp, A., and Swartz, J.F., 1990. Vein structures of the Peru Margin, Leg 112. In Suess, E., von Huene, R., et al., *Proc. ODP, Sci. Results*, 112: College Station, TX (Ocean Drilling Program), 3–16.
- Manheim, F.T., and Sayles, F.L., 1974. Composition and origin of interstitial water of marine sediments based on deep sea drilled cores. In Goldberg, E.D. (Ed.), *The Sea* (Vol. 5): New York (Wiley Interscience), 527–568.
- McCoy, F.W., Jr., 1974. Late Quaternary sedimentation in the Eastern Mediterranean Sea [Ph.D. thesis]. Harvard University, Cambridge, MA.
- Prahl, F.G., and Wakeham, S.G., 1987. Calibration of unsaturation patterns in long-chain ketone compositions for paleotemperature assessment. *Nature*, 330:367–369.
- Robertson, A.H.F., Kidd, R.B., Ivanov, M.K., Limonov, A.F., Woodside, J.M., Galindo-Zaldivar, J., Nieto, L., and the Scientific Party of the 1993 TTR-3 Cruise, 1994a. Probing continental collision in the Mediterranean Sea. *Eos*, 75:233, 239.
- , 1995. Eratosthenes Seamount, easternmost Mediterranean: evidence of active collapse and underthrusting beneath the Cyprus active Margin. *Terra Nova*, 7:254–264.
- Robertson, A.H.F., Woodside, J.M., and Kidd, R.B., 1994b. Eratosthenes Seamount (study area 3). 4.1. Geological setting. In Limonov, A.F., Woodside, J.M., and Ivanov, M.K. (Eds.), *Mud Volcanism in the Mediterranean and Black Seas and Shallow Structure of the Eratosthenes Seamount*. UNESCO Rep. Mar. Sci., 64:115–119.
- Robertson, A.H.F., Woodside, J.M., Limonov, A.F., and Kidd, R.B., 1994c. General interpretation. In Limonov, A.F., Woodside, J.M., and Ivanov, M.K. (Eds.), *Mud Volcanism in the Mediterranean and Black Seas and Shallow Structure of the Eratosthenes Seamount*. UNESCO Rep. Mar. Sci., 64:148–158.
- Sikes, E.L., and Volkman, J.K., 1993. Calibration of alkenone unsaturation ratios (U_{37}^*) for paleotemperature estimation in cold polar waters. *Geochim. Cosmochim. Acta*, 57:1883–1889.
- Spezzaferri, S., 1994. Planktonic foraminiferal biostratigraphy and taxonomy of the Oligocene and lower Miocene in the oceanic record: an overview. *Palaeontographica Ital.*, 81:1–187.
- Sprovieri, R., 1993. Pliocene–early Pleistocene astronomically forced planktonic Foraminifera abundance fluctuations and chronology of Mediterranean calcareous plankton bio-events. *Riv. Ital. Paleontol. Stratigr.*, 99:371–414.

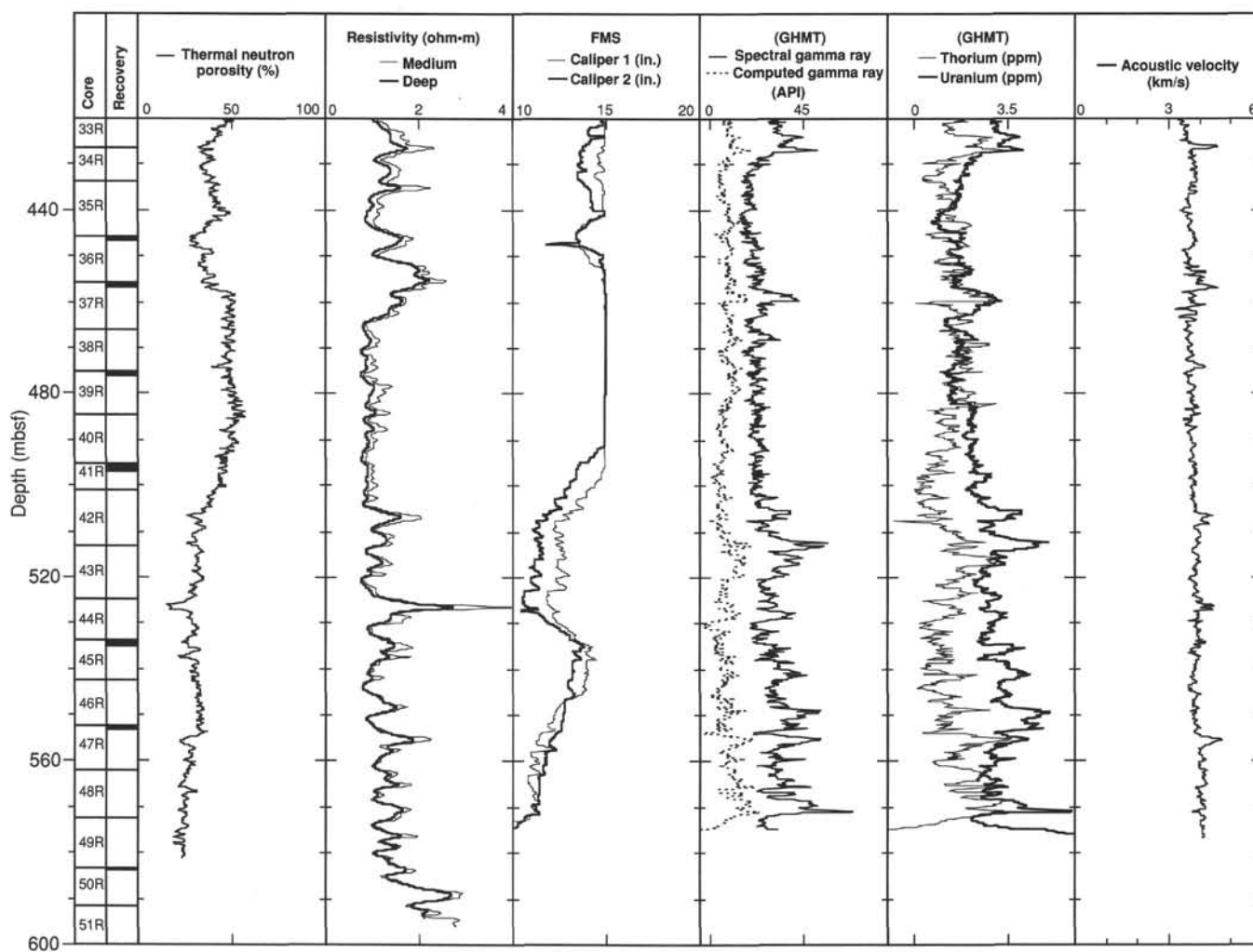


Figure 63 (continued).

Stanley, D.J., and Maldonado, A., 1979. Levantine Sea-Nile Cone lithostratigraphic evolution: quantitative analysis and correlation with paleoclimatic and eustatic oscillations in the Late Quaternary. *Sediment. Geol.*, 23:37-65.

ten Haven, L., 1986. Organic and inorganic aspects of Mediterranean late Quaternary sapropels and Messinian evaporitic deposits [Ph.D. thesis]. University of Utrecht, The Netherlands. *Geol. Utraiectina*, 46.

ten Haven, H.L., Baas, M., de Leeuw, J.W., and Schenck, P.A., 1987. Late Quaternary Mediterranean sapropels, I. On the origin of organic matter in sapropel S₇. *Mar. Geol.*, 75:137-156.

Westbrook, G.K., Carson, B., Musgrave, R.J., et al., 1994. *Proc. ODP, Init. Repts.*, 146 (Pt. 1): College Station, TX (Ocean Drilling Program).

Ms 160IR-108

NOTE: Core-description forms ("barrel sheets") and core photographs can be found in Section 5, beginning on page 535. Forms containing smear-slide data can be found in Section 6, beginning on page 951. Color reflectance, physical properties, chemistry, and thin-section data are presented on the CD-ROM (back pocket).

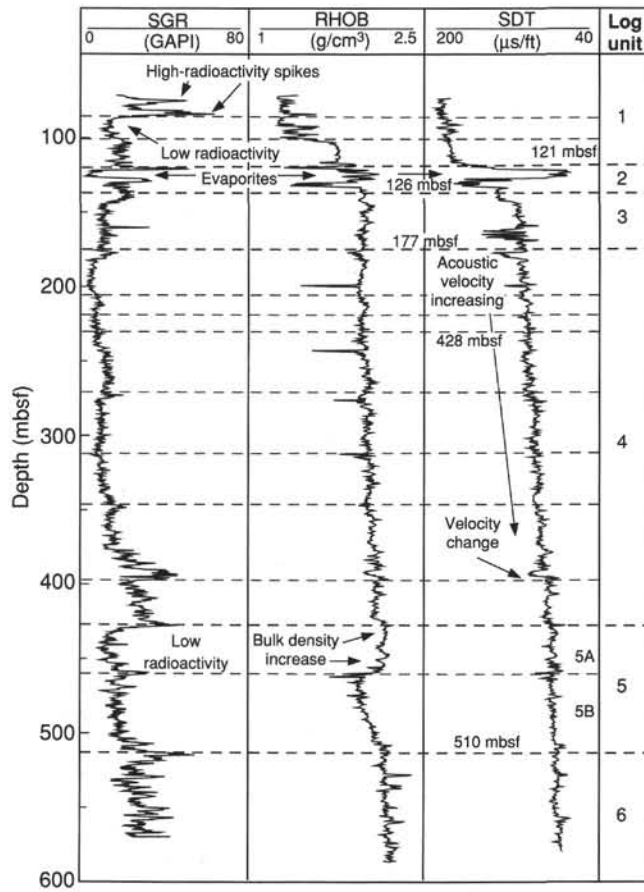


Figure 64. Interpreted log Units 1 through 4 in Hole 967E. The natural gamma-ray radioactivity (SGR), density (RHOB), and preliminary ship-board-reprocessed sonic (SDT) logs illustrate the changes in log character related to changes in the composition and texture of the sediments. The dotted lines within Units 2 and 4 show the boundaries between intervals differentiated in a preliminary interpretation that are most probably related to sequence boundaries or changing conditions in the sedimentary environment.

Table 16. Elemental yield ratios provided routinely by the geochemical logging tool.

Salinity-indicator ratio (SIR)	Cl/H
Porosity-indicator ratio (PIR)	H/(Si + Ca)
Iron-indicator ratio (IIR)	Fe/(Si + Ca)
Lithology-indicator ratio (LIR)	Si/(Si + Ca)

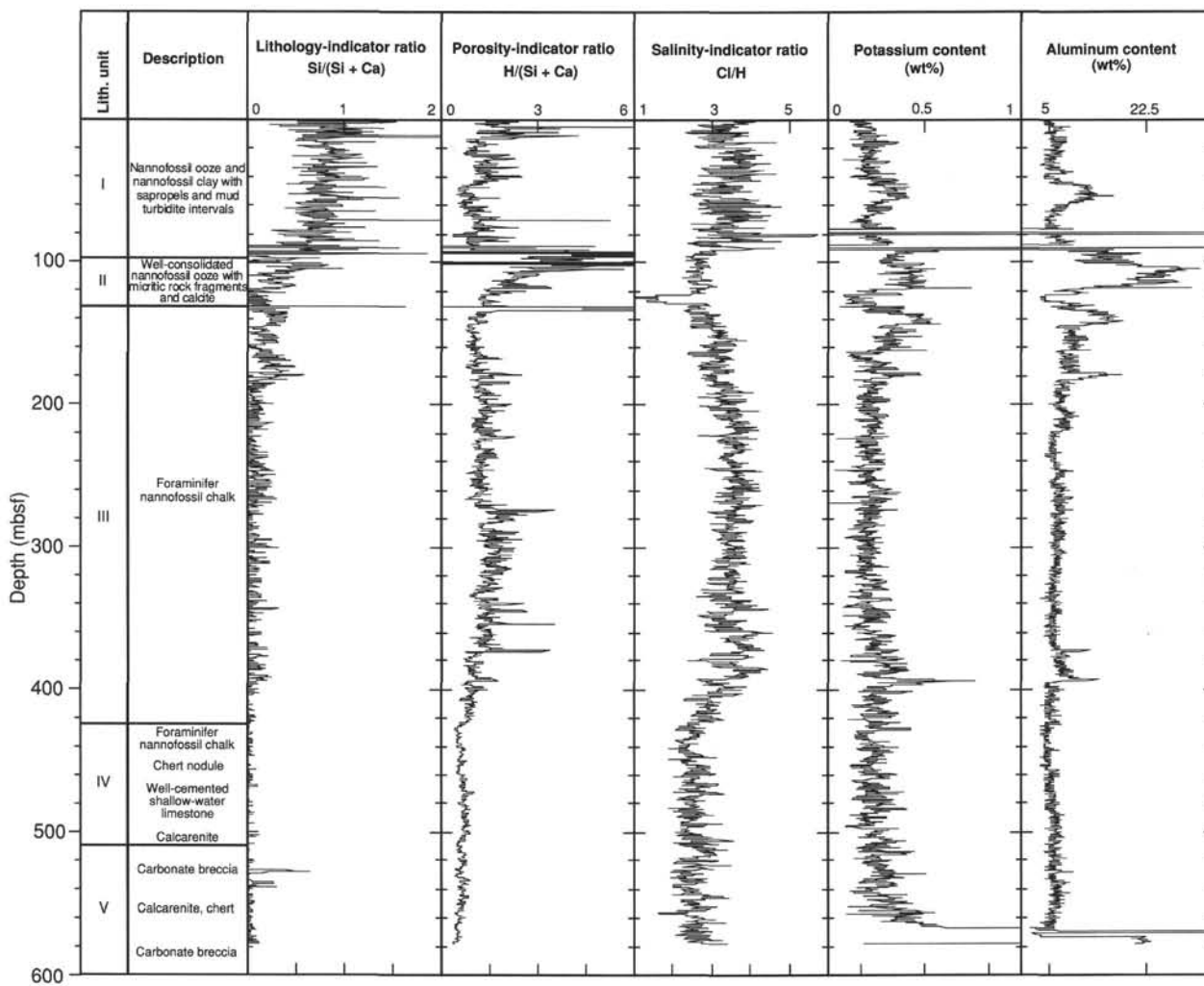


Figure 65. Lithology-indicator ratio, porosity-indicator ratio, salinity-indicator ratio, and potassium and aluminum contents profiles from geochemical logging tool measurements in Hole 967E. The right-hand column contains the lithostratigraphic units and a brief description for comparison.

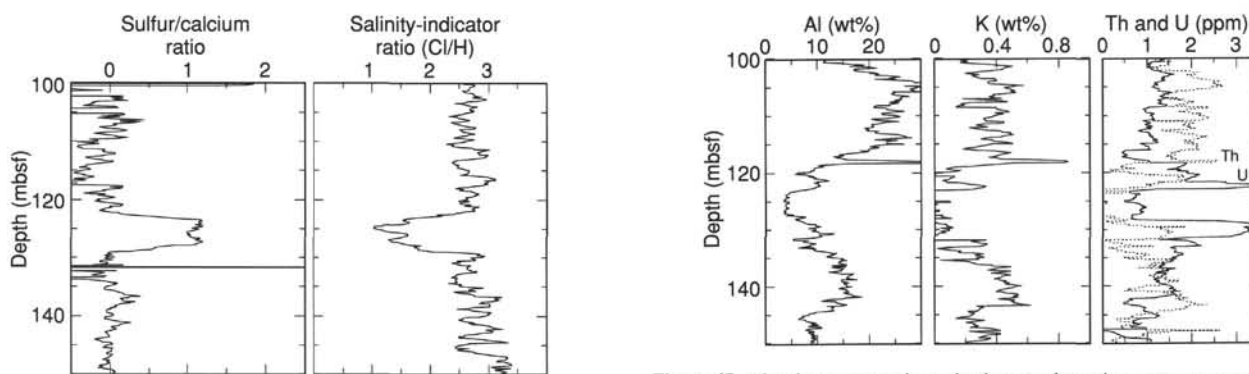


Figure 66. The sulfur/calcium and salinity-indicator ratios showing the gypsum layer at 120 mbsf in Hole 967E.

Figure 67. Aluminum, potassium, thorium, and uranium contents around the gypsum layer in Hole 967E.

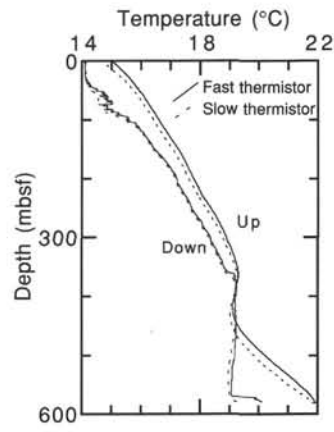


Figure 68. Data from the second run of the temperature logging tool in Hole 967E.

Table 17. Zones of possible water flow, Hole 967E.

Zone	Depth (mbsf)
1	38, 44, 51, 55, 60, 64, 67, 71, 75, 88, 93, 100, and 105
2	190, 215, 240, 260, 275, 300, 310, 320, and 340
3	375, 364, and 368

SHORE-BASED LOG PROCESSING

HOLE 967E

Bottom felt: 2564 mbrf
Total penetration: 600.3 mbsf
Total core recovered: 72.3 m (14.8%)

Logging Runs

Logging string 1: DIT/SDT-LSS/HLDT/CNT/NGT

Logging string 2: ACT/GST/NGT

Logging string 3: FMS/GPIT/NGT

Logging string 4: GHMT/NGT

The wireline heave compensator was used to counter ship heave resulting from the mild sea conditions.

Bottom-hole Assembly

The following depths for the BHA are as they appear on the logs after differential depth shift (see **Depth shift** section) and depth shift to the seafloor. As such, there might be a discrepancy with the original depths given by the drillers on board. Possible reasons for depth discrepancies are ship heave, use of wireline heave compensator, and drill string and/or wireline stretch.

DIT/SDT-LSS/HLDT/CNT/NGT: BHA at ~71.5 mbsf

ACT/GST/NGT: BHA at ~91.5 mbsf.

FMS/GPIT/NGT: BHA at ~71.5 mbsf.

GHMT/NGT: did not reach the BHA.

Processing

Depth shift: All original logs were interactively depth shifted with reference to the NGT from the DIT/SDT-LSS/HLDT/CNT/NGT run and to the seafloor (2564 mbrf).

Gamma-ray processing: The NGT data were processed to correct for borehole size and type of drilling fluid.

Acoustic data processing: The sonic logs were processed to eliminate some of the noise and cycle skipping experienced during recording.

Geochemical processing: For a detailed explanation of the processing, please refer to the "Explanatory Notes" chapter (this volume) or to the "geochem.doc" file on the enclosed CD-ROM. The elemental yields recorded by the GST tool represent the relative contribution of only some of the rock-forming elements (iron, calcium,

chlorine, silica, sulfur, hydrogen, gadolinium, and titanium; the last two are computed during geochemical processing) to the total spectrum. Because other rock-forming elements are present in the formation (such as aluminum and potassium), caution is recommended in using the yields to infer lithologic changes. Instead, ratios (see "acronyms.doc" file on the CD-ROM) are more appropriate to determine changes in the macroscopic properties of the formation. A list of oxide factors used in geochemical processing includes the following:

$\text{SiO}_2 = 2.139$

$\text{CaCO}_3 = 2.497$

$\text{FeO}^* = 1.358$

$\text{TiO}_2 = 1.668$

$\text{K}_2\text{O} = 1.205$

$\text{Al}_2\text{O}_3 = 1.889$

FeO^* = computed using an oxide factor that assumes a 50:50 combination of Fe_2O_3 and FeO factors.

Quality Control

Data recorded through the BHA, such as the NGT and CNT data above 71.5 mbsf, should be used only qualitatively because of the attenuation on the incoming signal. Invalid NGT spikes were recorded at 59–62 and 69–73 mbsf during the DIT/SDT-LSS/HLDT/CNT/NGT run and at 75–80 and 87–92 mbsf during the ACT/GST/NGT run.

Invalid SFL data were recorded at 290–246, 528–534, and 550–553 mbsf owing to tool malfunction.

Invalid PEF spikes were recorded at 119 and 126 mbsf.

Hole diameter was recorded by the hydraulic caliper on the HLDT tool (CALI) and on the FMS string (C1 and C2).

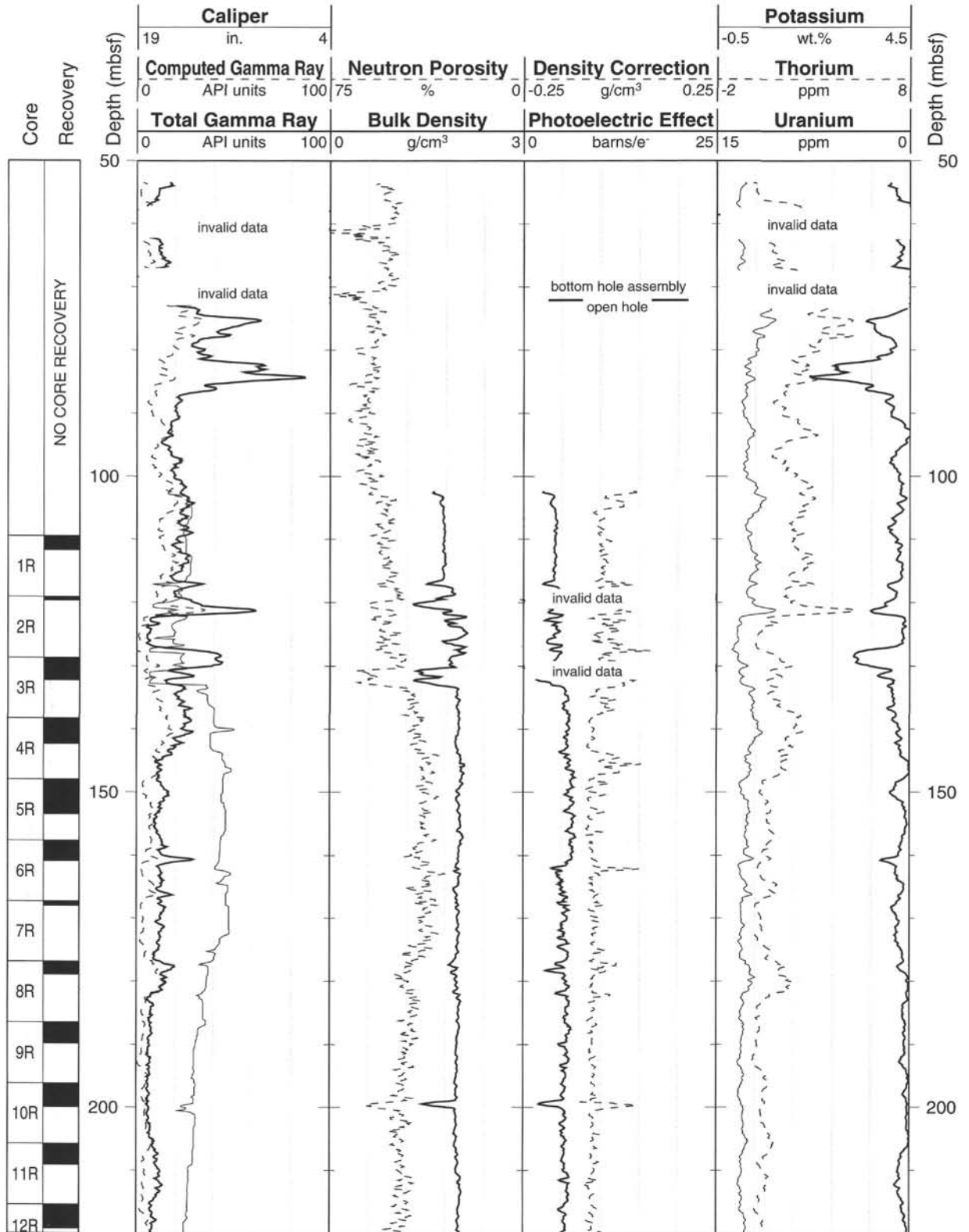
FACT = quality control curve in geochemical processing. Accuracy of the estimates is inversely proportional to the magnitude of the curve.

Details of standard shore-based processing procedures are found in the "Explanatory Notes" chapter (this volume). For further information about the logs, please contact:

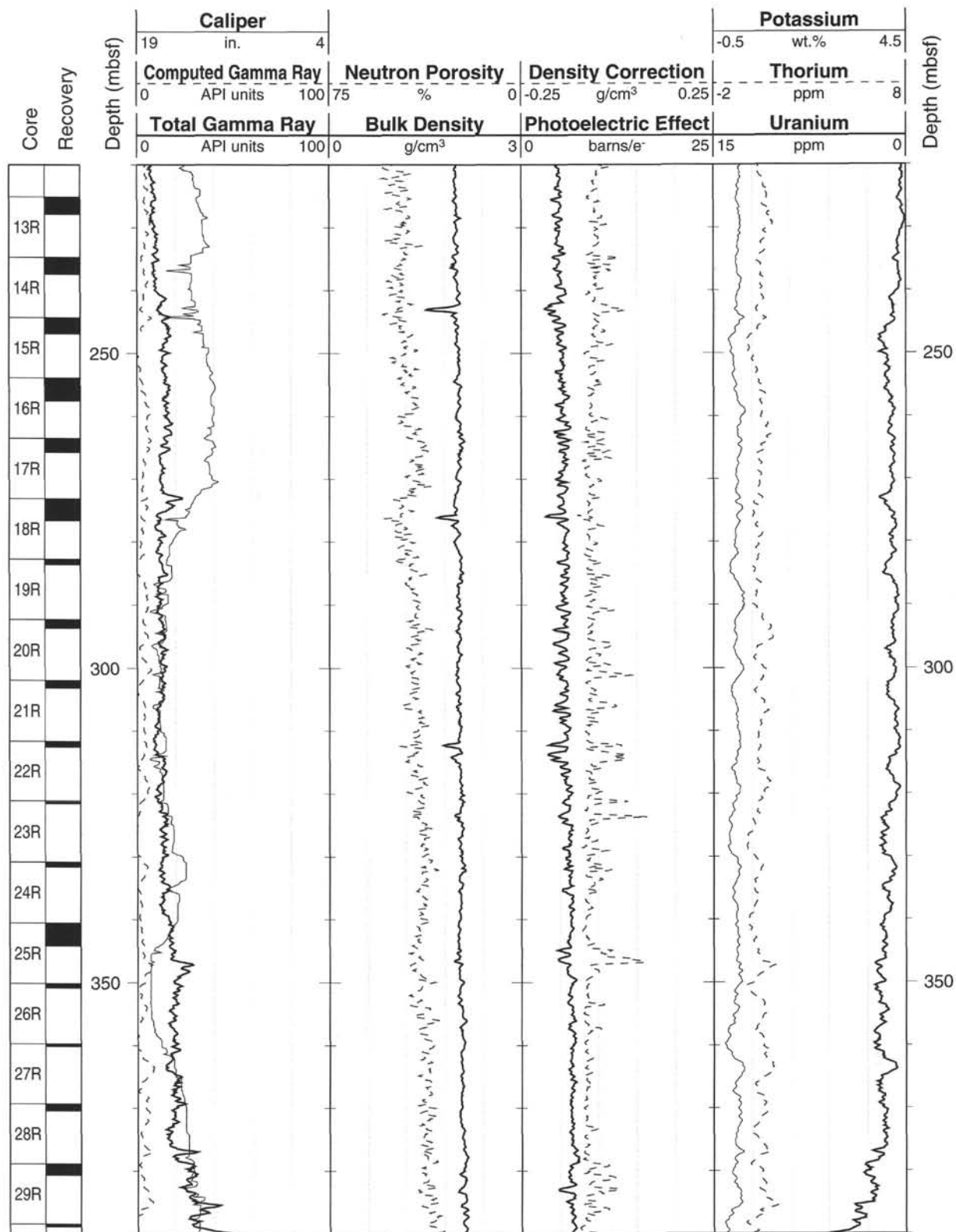
Cristina Broglia
 Phone: 914-365-8343
 Fax: 914-365-3182
 E-mail: chris@ideo.columbia.edu

Elizabeth Pratson
 Phone: 914-365-8313
 Fax: 914-365-3182
 E-mail: beth@ideo.columbia.edu

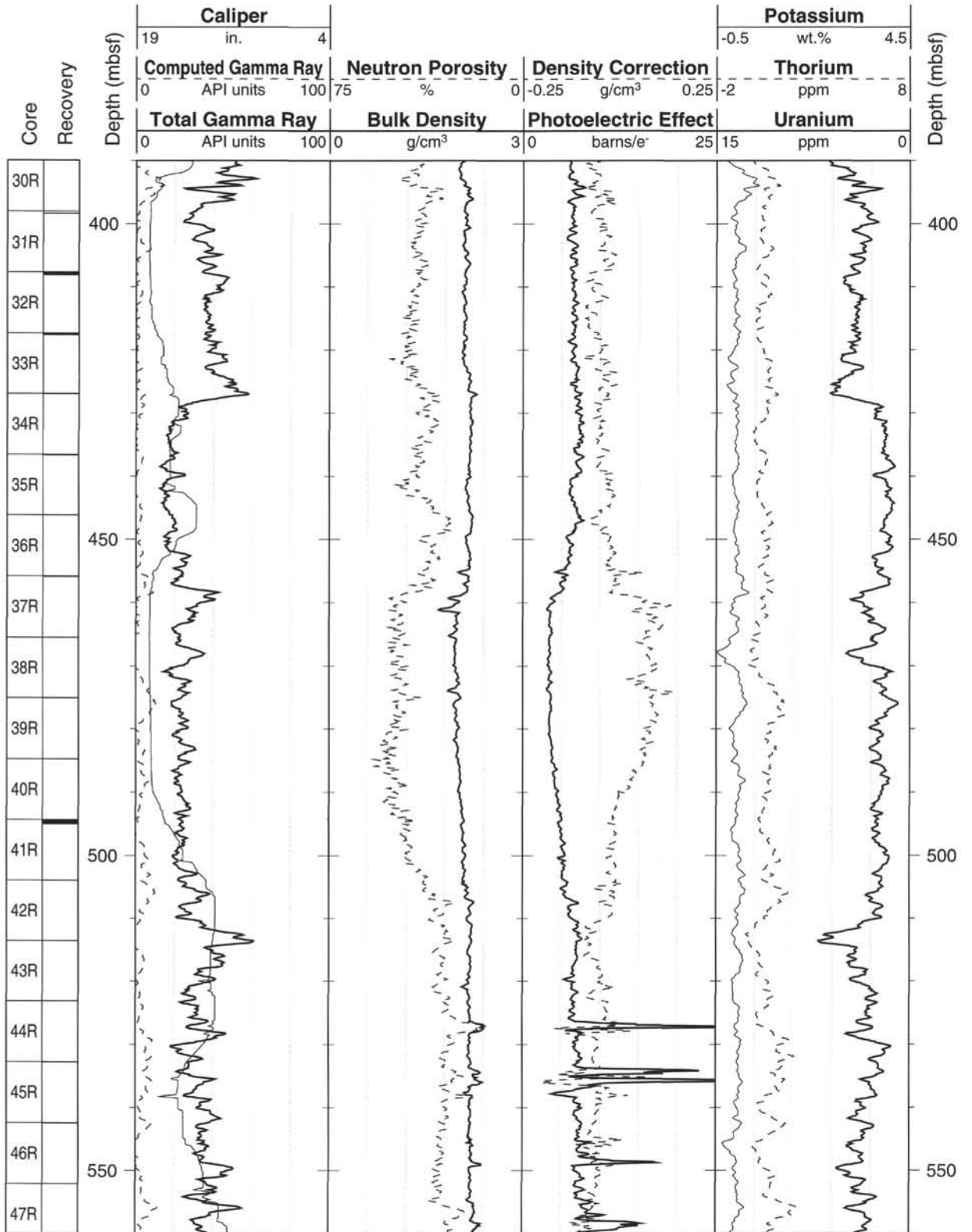
Hole 967E: Natural Gamma Ray-Density-Porosity Logging Data



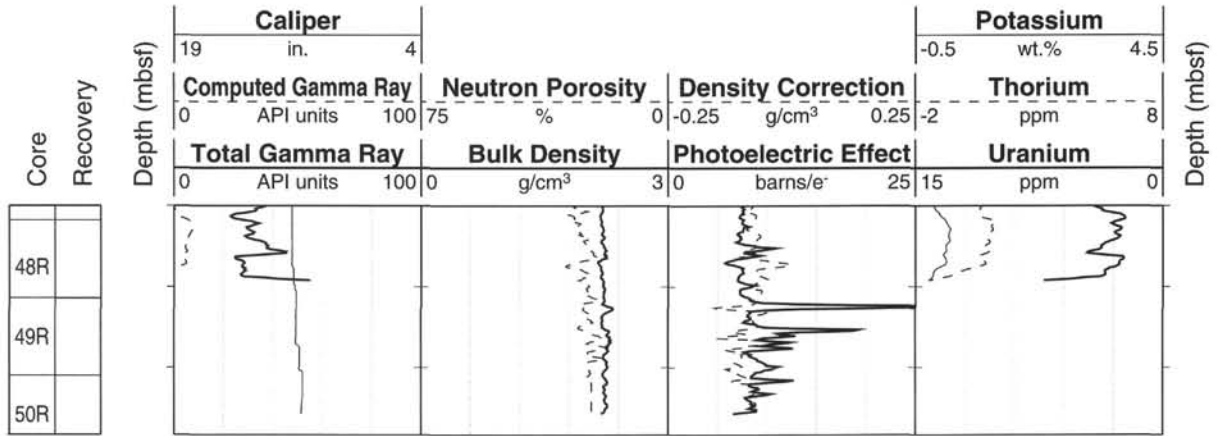
Hole 967E: Natural Gamma Ray-Density-Porosity Logging Data (cont.)



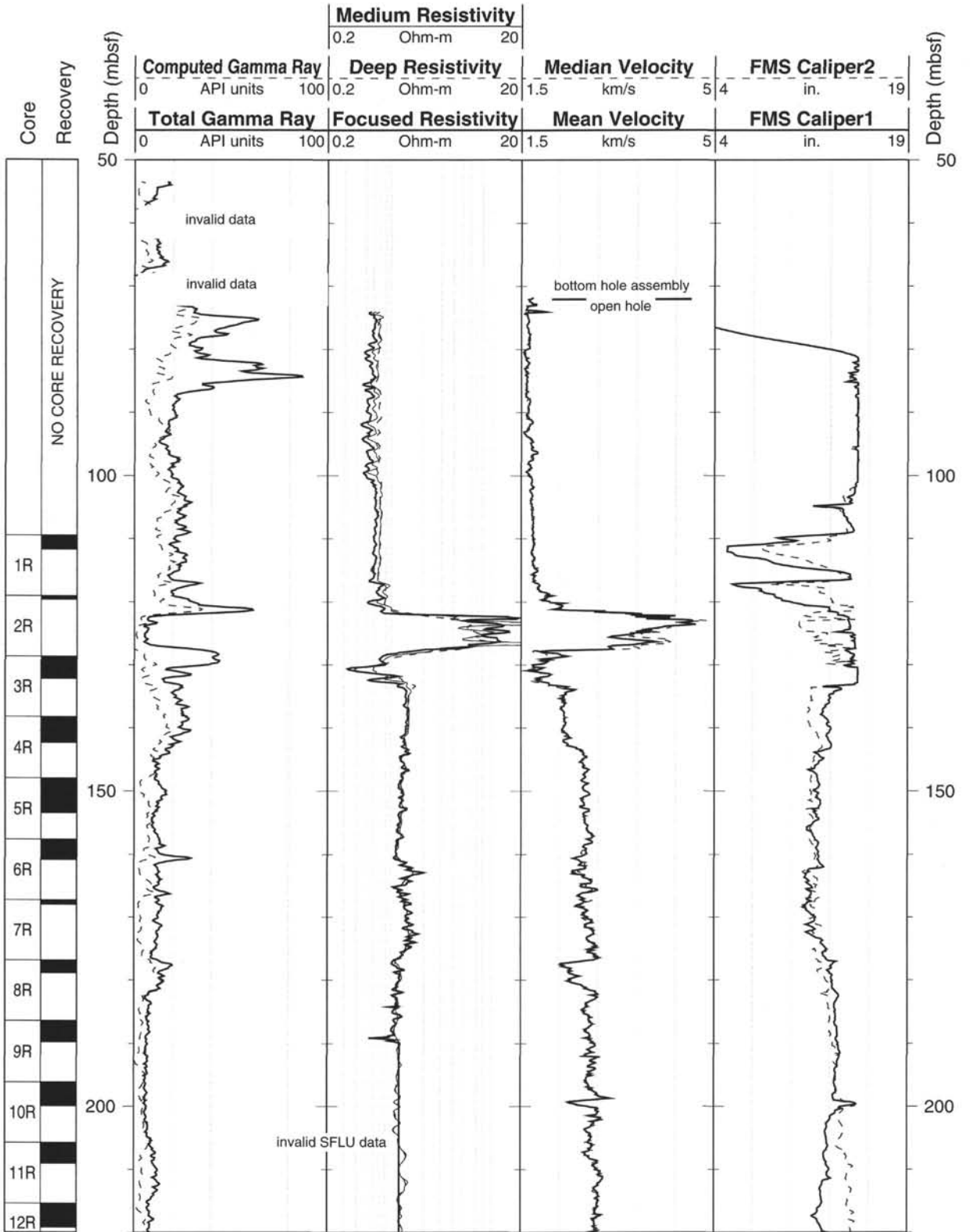
Hole 967E: Natural Gamma Ray-Density-Porosity Logging Data (cont.)



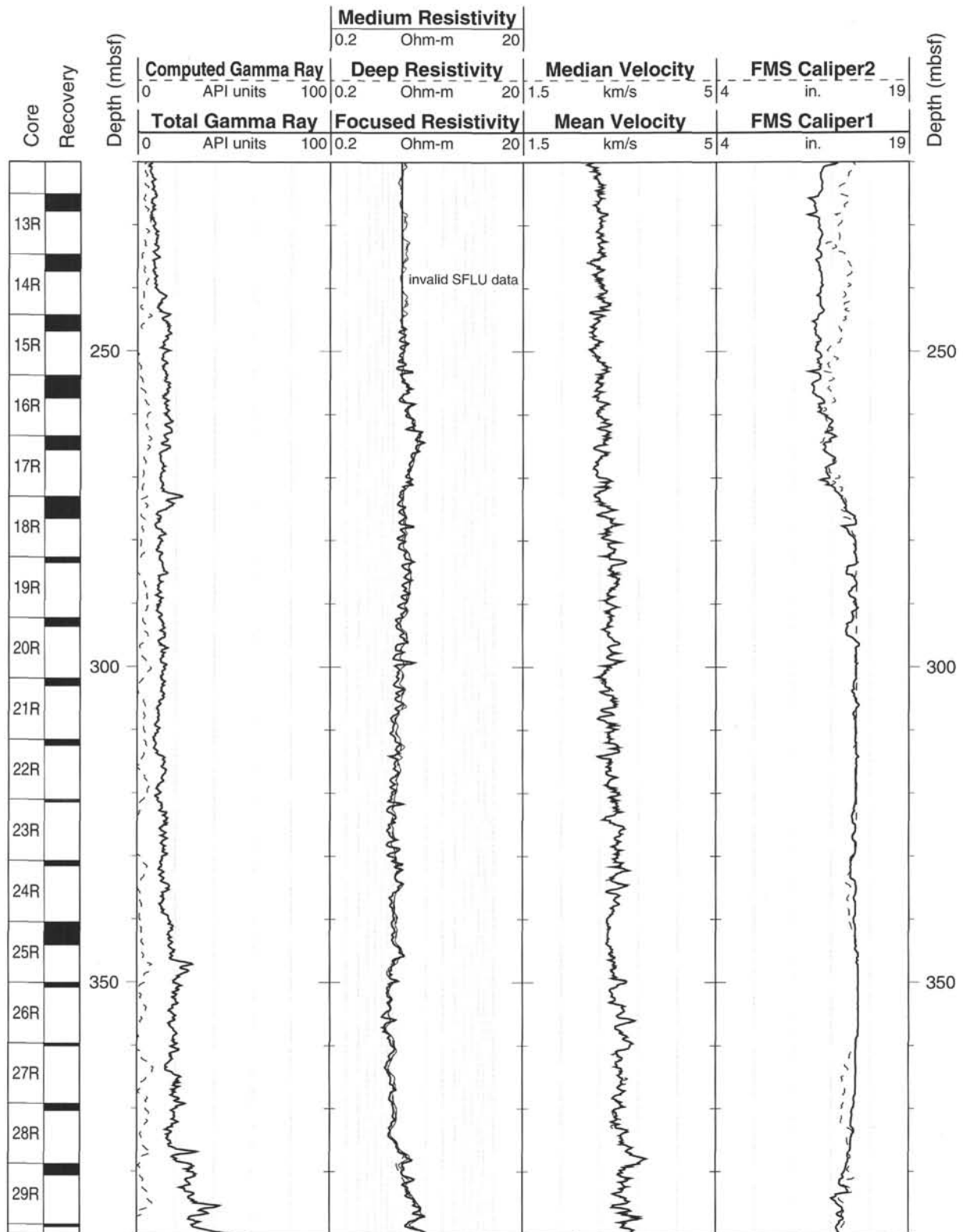
Hole 967E: Natural Gamma Ray-Density-Porosity Logging Data (cont.)



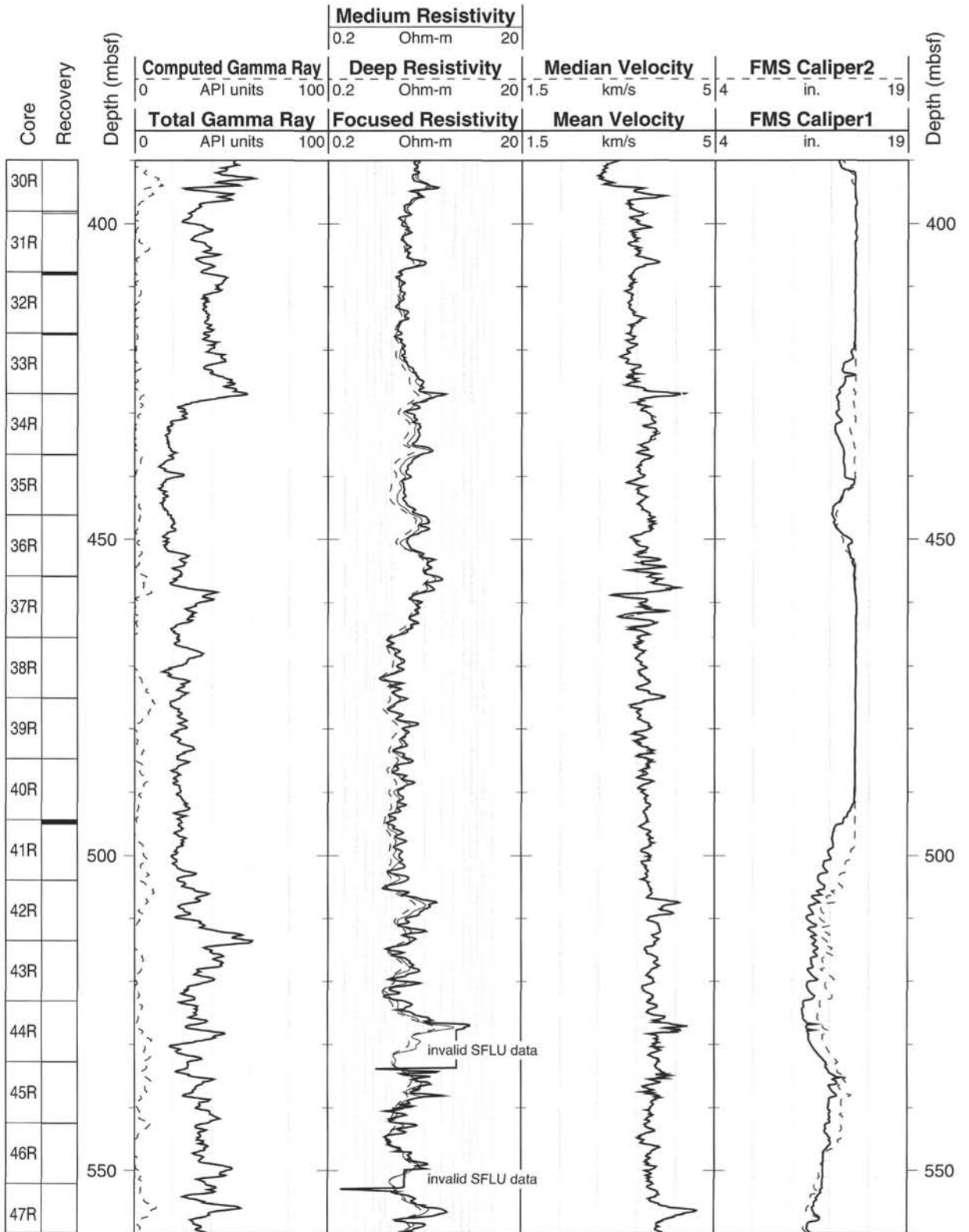
Hole 967E: Natural Gamma Ray-Resistivity-Sonic Logging Data



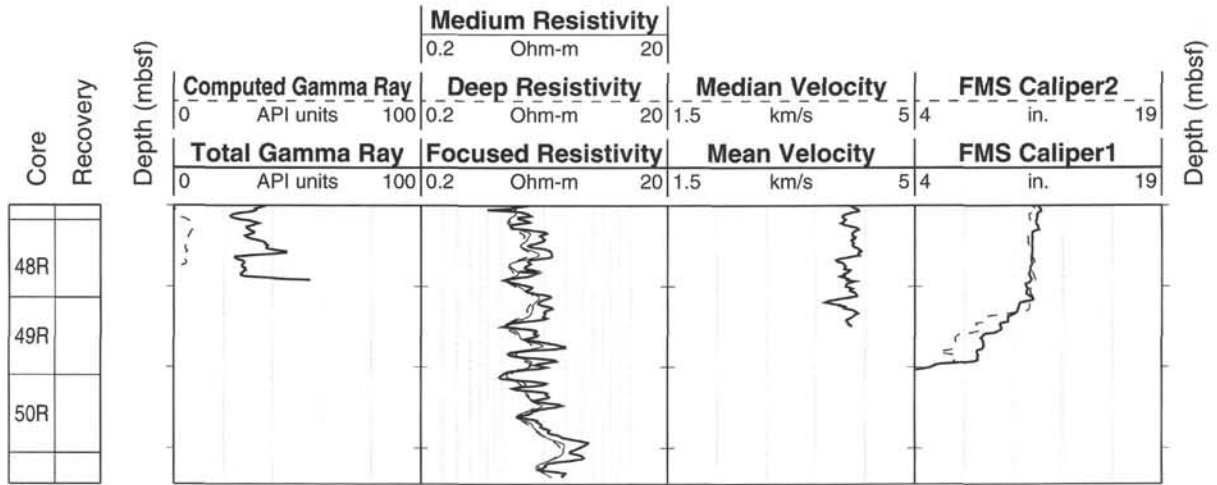
Hole 967E: Natural Gamma Ray-Resistivity-Sonic Logging Data (cont.)



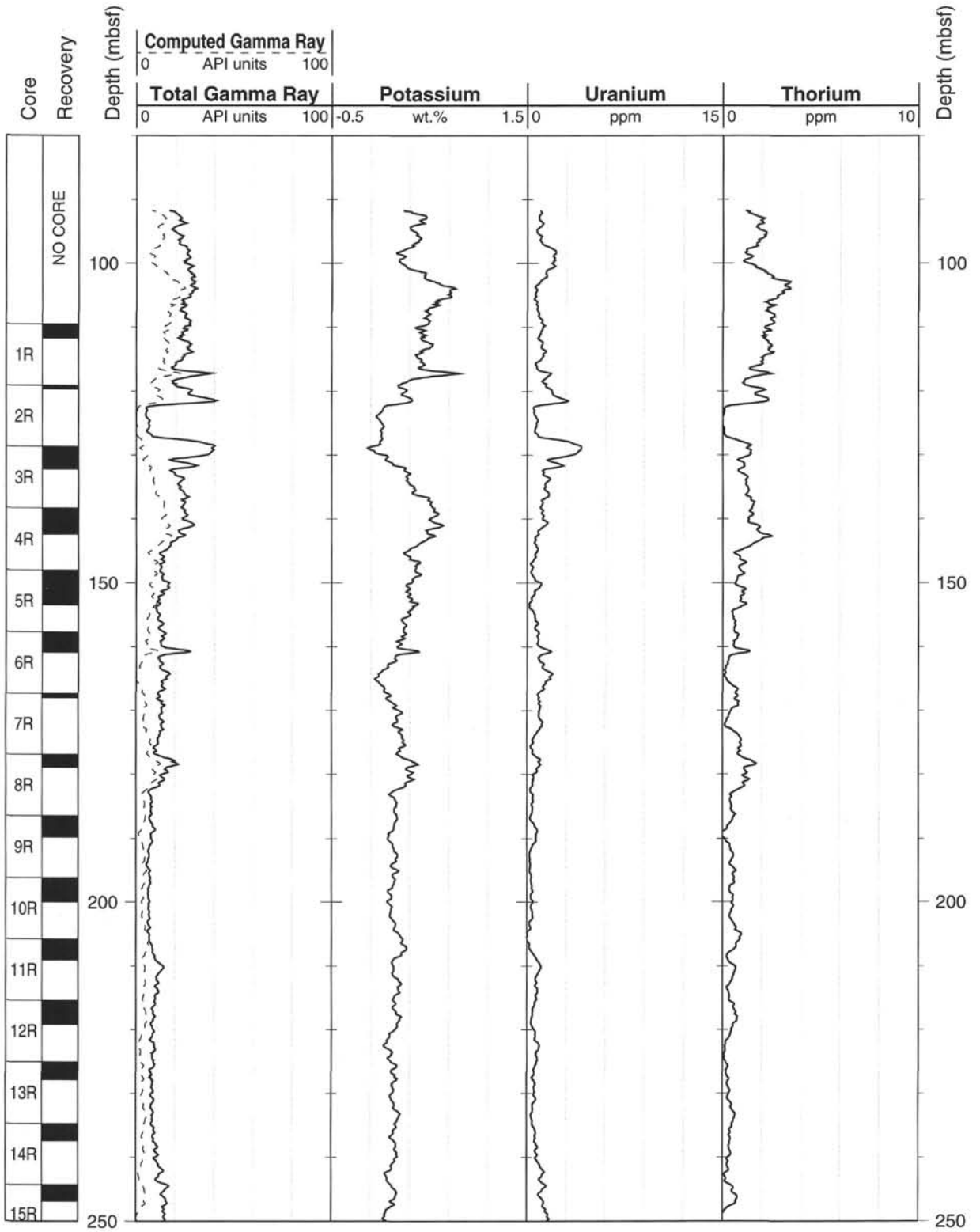
Hole 967E: Natural Gamma Ray-Resistivity-Sonic Logging Data (cont.)



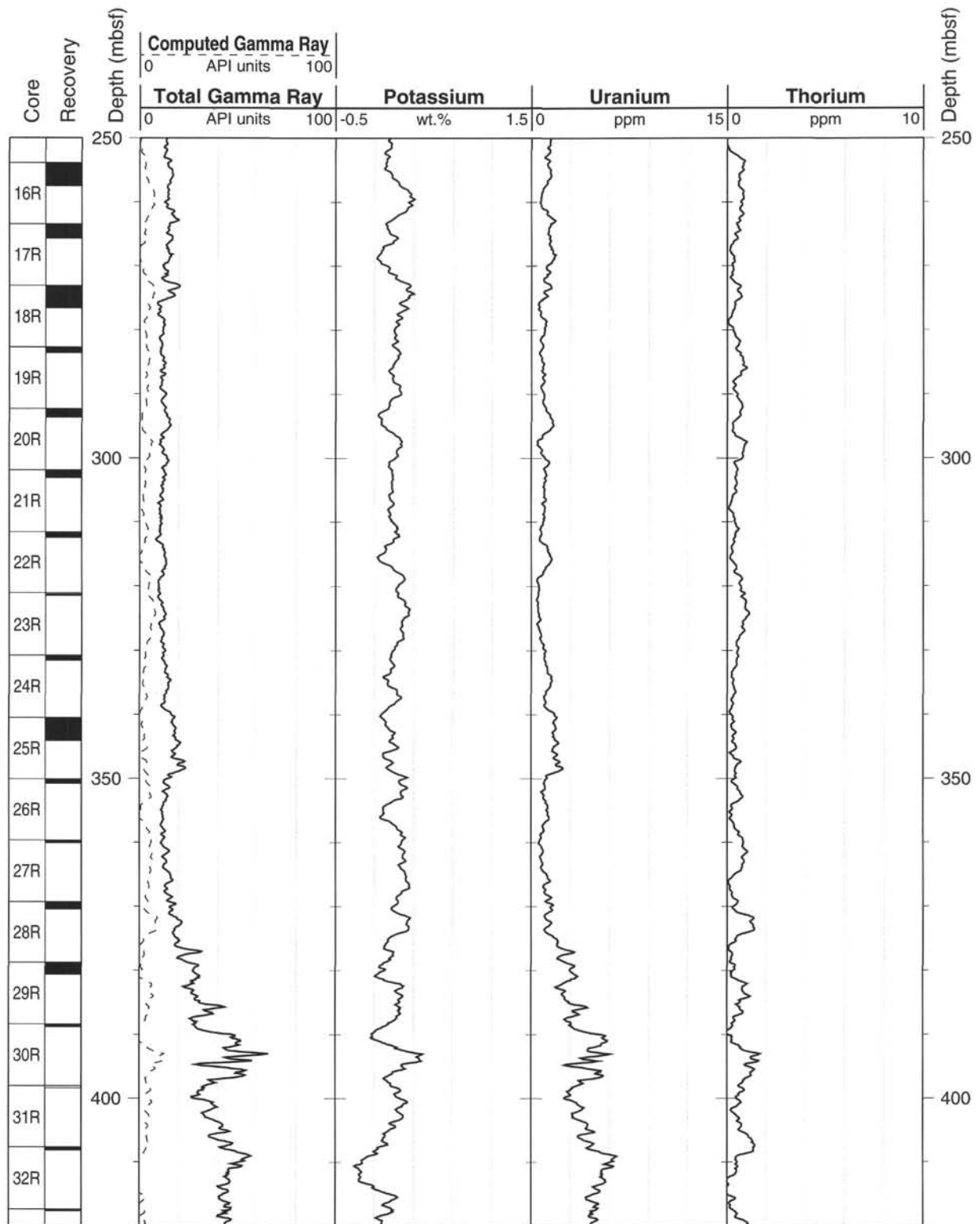
Hole 967E: Natural Gamma Ray-Resistivity-Sonic Logging Data (cont.)



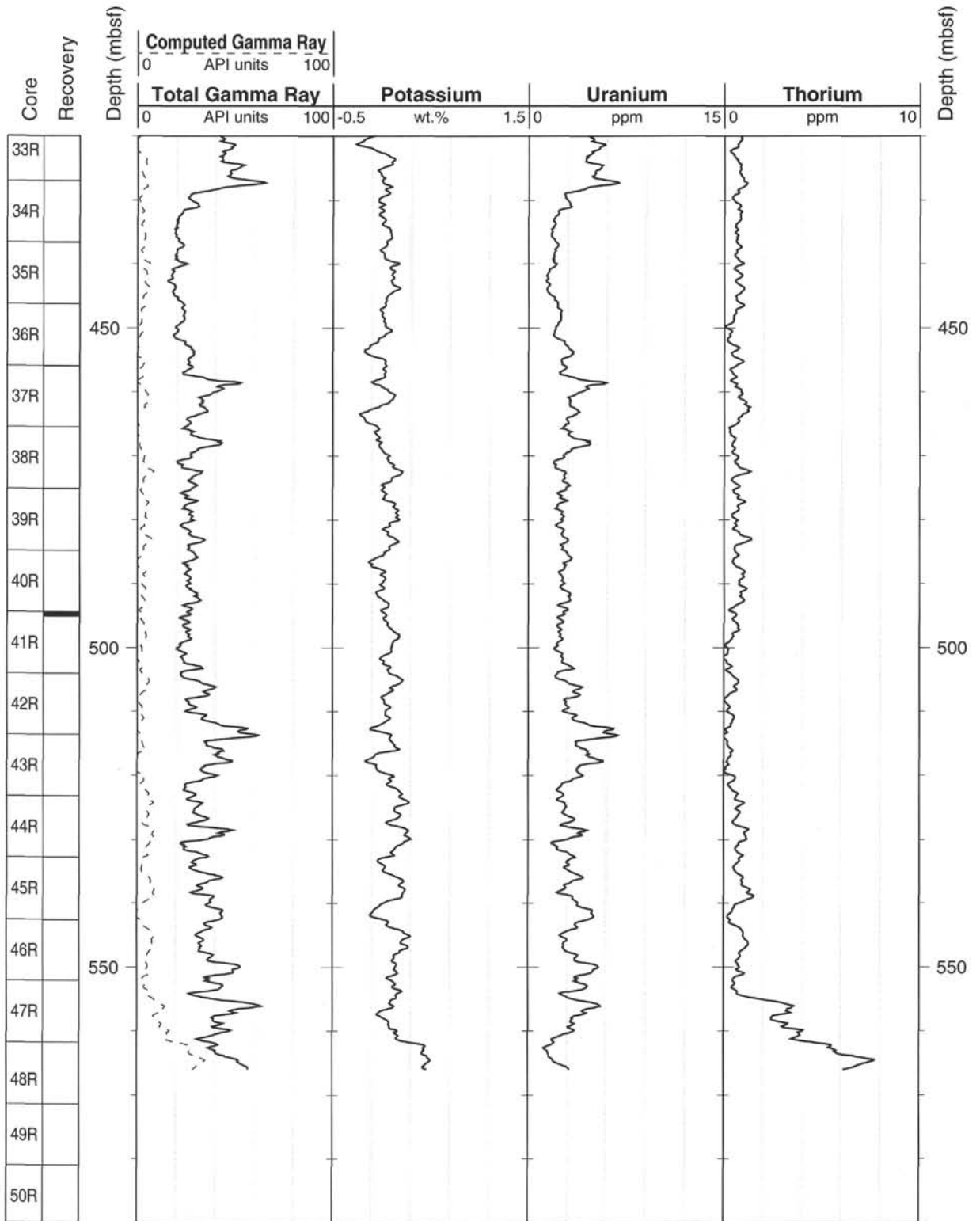
Hole 967E: Natural Gamma Ray Logging Data



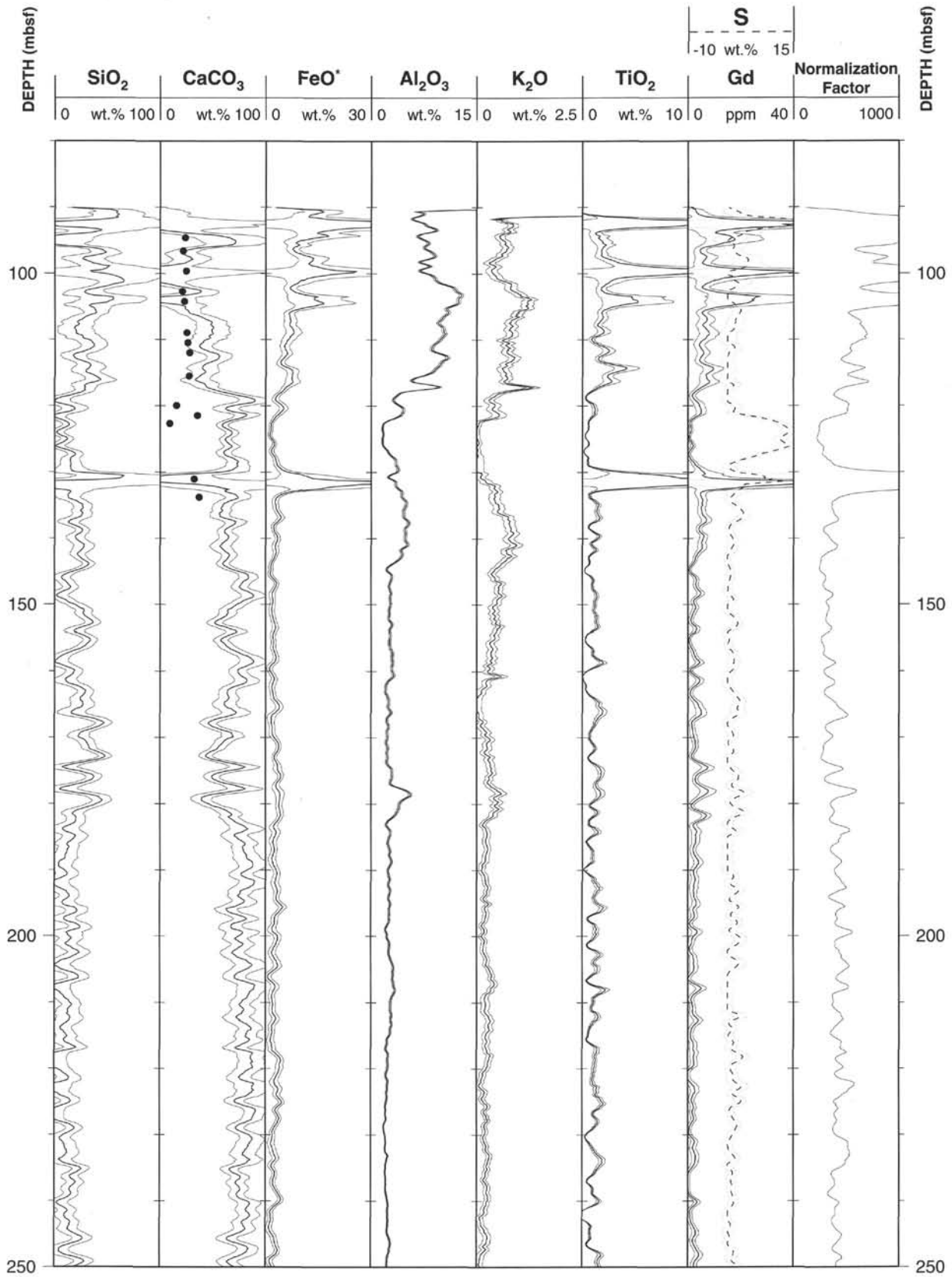
Hole 967E: Natural Gamma Ray Logging Data (cont.)



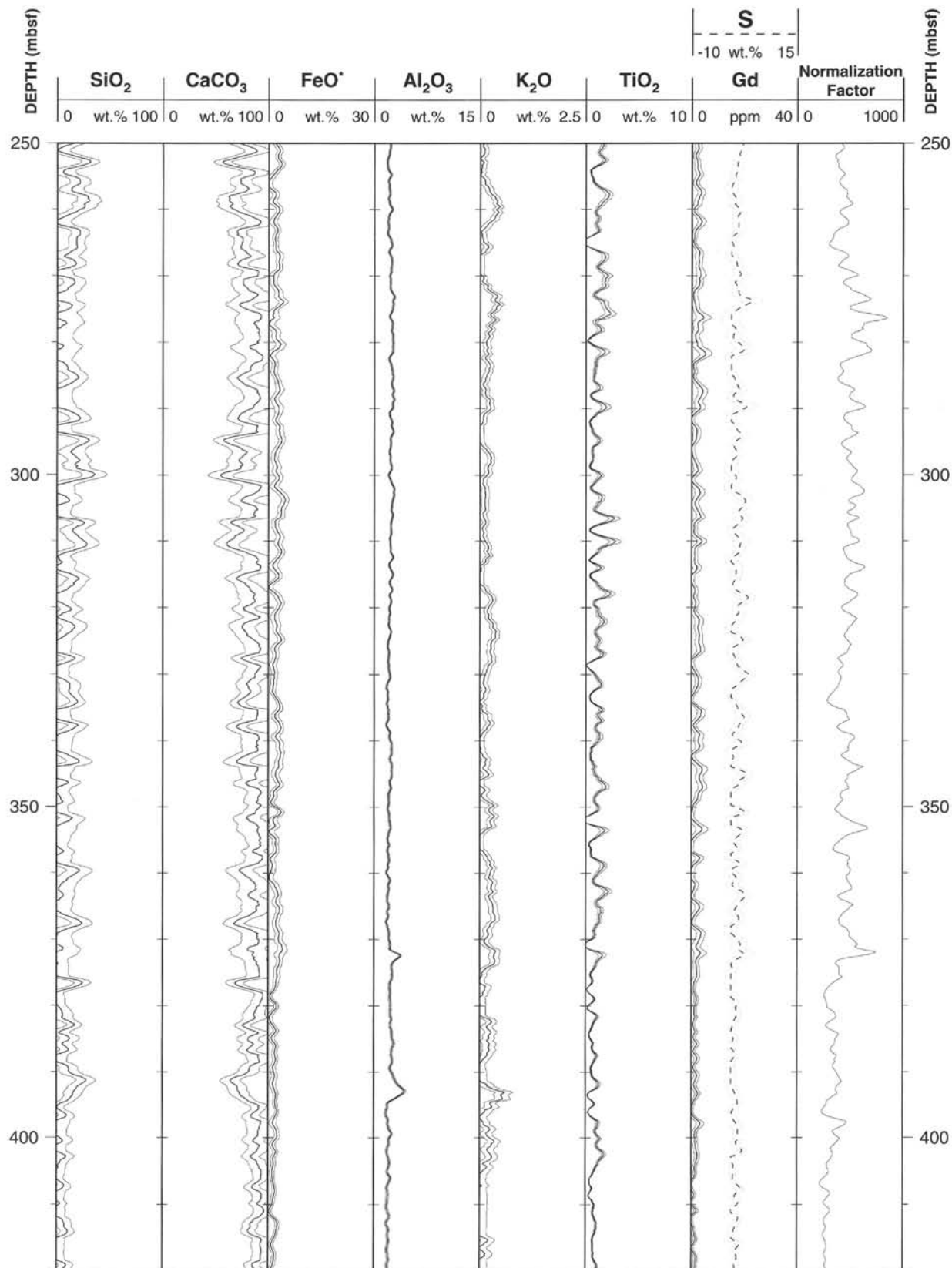
Hole 967E: Natural Gamma Ray Logging Data (cont.)



Hole 967E: Geochemical Logging Data



Hole 967E: Geochemical Logging Data (cont.)



Hole 967E: Geochemical Logging Data (cont.)

